# Dark Current and Persistence in HgCdTe-on-Si Infrared Detectors

---

Ph.D. *Doctor of Philosophy*

in Astrophysical Sciences and Technology

*Lazar Buntic*

---

School of Physics and Astronomy

Rochester Institute of Technology

Rochester, New York

December 2025

ASTROPHYSICAL SCIENCES AND TECHNOLOGY

COLLEGE OF SCIENCE

ROCHESTER INSTITUTE OF TECHNOLOGY

ROCHESTER, NEW YORK

Ph.D. DISSERTATION DEFENSE

---

Candidate: .....

Dissertation Title: .....

Adviser: .....

Date of defense: .....

The candidate's Ph.D. Dissertation has been reviewed by the undersigned. The Dissertation

(a) is acceptable, as presented.

(b) is acceptable, subject to minor amendments.

(c) is not acceptable in its current form.

*Written details of required amendments or improvements have been provided to the candidate.*

Committee:

---

Dr. Stefan Preble, Committee Chair

---

Dr. Michael Zemcov, Committee Member

---

Dr. Roger Smith, Committee Member

---

Dr. Donald F. Figer, Thesis Advisor

Please submit form to AST Graduate Program Coordinator

ASTROPHYSICAL SCIENCES AND TECHNOLOGY
COLLEGE OF SCIENCE
ROCHESTER INSTITUTE OF TECHNOLOGY
ROCHESTER, NEW YORK

# CERTIFICATE OF APPROVAL

**Ph.D. DEGREE DISSERTATION**

The Ph.D. Degree Dissertation of *Lazar Buntic* has been examined and approved by the dissertation committee as satisfactory for the dissertation requirement for the Ph.D. degree in Astrophysical Sciences and Technology.

Dr. Stefan Preble, Committee Chair

Dr. Michael Zemcov, Committee Member

Dr. Roger Smith, Committee Member

Dr. Donald F. Figer, Thesis Advisor

Date

Dark Current and Persistence in HgCdTe-on-Si Infrared Detectors

By

*Lazar Buntic*

A dissertation submitted in partial fulfillment of the requirements for the degree of Ph.D. in Astrophysical Sciences and Technology, in the College of Science, Rochester Institute of Technology.

December, 2025

Approved by

| | |
|---|---|
| Dr. Andrew Robinson | Date |
| Director, Astrophysical Sciences and Technology | |

*For Meghan, light of my life, my muse, and unending source of motivation. This would not have been possible without you.*

# Acknowledgments

I am incredibly grateful for the support that made this thesis possible, funded by a NASA FINESST Grant (Award Number 80NSSC22K1595).

I would like to acknowledge my colleagues at the Center for Detectors: Justin Gallagher, for keeping my harebrained schemes from running amok, Edwin Alexani, for his endless supply of humor and moral support, and my advisor Don Figer, for his inexhaustible knowledge of detector physics and always asking just the right questions to result in more research. He is fond of saying that there is infinite work to be done, and even after all these years I feel that I have barely scratched the surface of this field. I want to thank David Fanning, an unsung hero, whose open-source IDL library (idl-coyote) has prevented many IDL-related headaches. I would like to thank my family and friends for their love and support, too numerous to name here. You and your families have provided an invaluable quantity of joy and laughter to my life.

Finally, I acknowledge the use of Grok 4.1 (internal build v4.1-20251206-1), a large language model developed by xAI, as an auxiliary tool for proofreading, identifying grammatical errors, and enhancing the readability and consistency of the text. All scientific content, analysis, and conclusions remain the sole responsibility of the author.

# Abstract

This thesis investigates the performance of Raytheon's mercury-cadmium-telluride-on-silicon (MCT-on-Si) infrared detector arrays, with particular emphasis on the impact of the heteroepitaxial silicon growth process on dark current and persistence characteristics.

Infrared detectors have been the cornerstone of astronomical discovery for the past four decades and remain essential for current and future flagship observatories, including the James Webb Space Telescope and the Nancy Grace Roman Space Telescope. Traditionally, the highest-performance HgCdTe (MCT) arrays are grown on lattice-matched cadmium-zinc-telluride (CZT) substrates, which are costly and limited in size. To enable low-cost, large-format arrays, Raytheon developed a process for growth of MCT on silicon wafers. The large lattice mismatch between the materials in this approach introduces defects that degrade detector performance, and these effects are systematically characterized in the present work.

Analysis of the best-performing pixels in the SATIN engineering-grade array (detector V23) reveals dark current levels substantially closer to those of state-of-the-art MCT-on-CZT devices than previously reported for MCT-on-Si technology. Persistence measurements demonstrate that charge-trapping timescales span many orders of magnitude and that trapping occurs almost exclusively within the bulk active region rather than at surface states. A clear correlation is established between p-n junction implant area and performance in the metrics of dark current and linearity, driven by increased defect density in the active volume. Finally, on-sky observations obtained with the SATIN detectors are presented.

The results presented here show that MCT-on-Si technology offers a viable path toward low-cost, large-format, high-performance infrared imaging arrays for future astronomical instruments.

# Contents

# List of Figures

# List of Tables

# Chapter 1

# Introduction

The night sky has long served as a powerful symbol for humanity. Throughout human history and prehistory, it has represented the unknown: distant and incomprehensible, yet beautiful and alluring. Astronomers, like all scientists, are a consequence of the human drive to comprehend our environment and thereby master it. Although modern astronomy is often traced to the ancient Greeks and, later, to the scholars of the Islamic Golden Age, humans have studied the stars for millennia. As early as the Upper Paleolithic (5,000-10,000 years ago) our ancestors depicted constellations on cave walls, carved analemma of lunar zeniths, and may have attributed spiritual significance to caves which are illuminated only during equinoxes and solstices.[1] The tracking of equinoxes and constellations has undeniably been important to ancient man, although the reasons for doing so (whether spiritual or practical) have been a significant topic of debate.

## 1.1 A Brief History of Imagers

The ancient study of the sky relied on a remarkable yet limited natural imager: the human eye. Although the eye is well suited for everyday vision, it lacks the characteristics required of a scientific detector. The human brain, acting as sophisticated readout electronics, effectively masks many of these limitations — non-uniform spatial response, blind spots, wavelength-

[1] A review of this topic can be found in [2].

dependent sensitivity, saturation, and severe persistence effects.[2] Most critically, the eye cannot integrate light over long periods, both because of its physiological design and because a human observer cannot remain sufficiently motionless.

Consequently, nearly all major advances in astronomy beyond simple catalogs of the brightest objects have required corresponding technological breakthroughs. The 19th century began with the development of photographic plates, which rapidly gave rise to the first dedicated astronomical imaging systems. A mere decade after the first daguerreotype, in 1840, J. W. Draper and others used photographic plates to record images of the Moon. Although film soon replaced plates in commercial photography, astronomical plates remained in widespread use until the late 20th century, most famously for the Palomar Observatory Sky Surveys conducted in the 1950s and again in the 1990s.

Photographic plates were only the first modern imaging technology; the 20th century saw the development of numerous electronic devices for collecting and quantifying light. The photomultiplier tube (PMT), invented in the 1930s by the Soviet physicist Leonid Kubetsky, exemplifies this transition. In a PMT, an incident photon striking the photocathode ejects a photoelectron, which a series of increasingly positive dynodes then accelerates and multiplies through secondary emission. A single photoelectron can thereby produce an avalanche of thousands or millions of electrons at the anode, generating a readily measurable voltage pulse. A related device, the proportional gas counter developed in the 1940s, operates on a similar principle of controlled electron multiplication within a noble-gas-filled chamber surrounding a high-voltage anode wire. When an ionizing particle or photon enters the chamber, it triggers a localized electron avalanche that produces a detectable signal. The core concept of electron multiplication pioneered in these early devices remains central to many state-of-the-art detectors today, albeit in radically different implementations.

The invention of the transistor in 1947, followed by rapid progress in solid-state electronics, laid the foundation for digital information storage. In 1969 the charge-coupled device (CCD) was invented by Willard Boyle and George Smith at Bell Laboratories [3]. They recognized

[2] Persistence manifests as the afterimage observed after viewing a bright source such as the Sun, a lightning bolt, or a welding arc, and then closing one's eyes.

that charge packets could be stored in metal-oxide-semiconductor (MOS) capacitors and sequentially transferred along a linear or two-dimensional array by applying appropriate clock voltages. Within two years, by 1971, the first CCD imagers were operational. These CCD imagers would quickly become widely used for astronomy, despite some fundamental architectural flaws. Problems arise from the charge transfer mechanism, which requires charge to be passed from one pixel to the next in order to reach the readout amplifiers at the edge of the devices. Loss of charge during this process is known as charge-transfer inefficiency (CTI or CTE), and it makes accurate charge measurements difficult. Additionally, if any pixel in a row is rendered inoperable the charge transfer across it becomes impossible, effectively making the rest of the row inoperable as well. If a device could perform charge readout directly from the pixel instead of having to pipe the charge across the device, it would circumvent the problems of CCD architecture. Complementary Metal-Oxide-Semiconductor (CMOS) technology emerged in the 1960s, but its application to imaging had to await the development of the active-pixel sensor (APS) architecture. The first practical CMOS APS was demonstrated in 1993 by Eric Fossum and his collaborators. The introduction of these devices marks the beginning of the modern era of electronic imaging in astronomy. Since the 1970s, CCDs, and later CMOS sensors and their derivatives, have become the dominant detectors in virtually every major astronomical imaging instrument.

Detector technology has greatly improved the human understanding of the universe that surrounds us. Improvements in detector performance enable observations of faint objects previously considered beyond our reach. Without the advancement of detector technology over the past century, humanity would still have a poor understanding of the mechanics of galaxies, star formation, and most cosmological phenomena. Every major discovery is the result of either pointed investigation or analysis of data acquired in major sky surveys, all of which require detectors.

## 1.2 Infrared Light

Infrared (IR) radiation was discovered in 1800 by William Herschel. He passed sunlight through a glass prism and showed that thermometers placed just beyond the visible red end of the spectrum registered a temperature rise even though no visible light reached them. Throughout the 19th century, rudimentary IR detectors—primarily bolometers and thermopiles—were developed. These devices produce a measurable voltage in response to temperature changes in their absorbing elements.

Simple lead sulphide (PbS) "night vision" devices were conceived for use in anti-air applications in the first half of the 20th century, and saw further development at the hands of major players in the second world war, primarily the Germans and Americans [4]. The breakthrough for modern IR astronomy came from advances in narrow-gap semiconductors: indium antimonide (InSb) was first synthesized in 1952, and mercury cadmium telluride (HgCdTe or MCT) was developed in 1959. Other materials still saw use in detectors: PbS detectors were used in the late 1960s for the Two Micron Sky Survey (TMSS) to scan 70% of the night sky and catalogue 5,700 objects. The tunable bandgap of MCT proved especially revolutionary, enabling detectors optimized for specific infrared wavelength ranges. These detectors can cover the 1–30 $\mu$m range effectively. However, the majority of astronomical applications exploit the 1–15 $\mu$m interval as the atmosphere is essentially opaque to infrared light at wavelengths greater than 15 $\mu$m primarily due to the presence of water vapor [5].

## 1.3 Mercury Cadmium Telluride on Silicon

$Hg_{1-x}Cd_xTe$—where $x$ is the cadmium mole fraction—is a II-VI ternary semiconductor alloy that has historically been the premier material for infrared detectors [4]. It offers exceptional flexibility in wavelength tuning from 1–30 $\mu$m, enabling detectors for a wide range of military, medical, and scientific applications. Adjusting $x$ directly controls the bandgap and thus the long-wavelength cutoff of the detector. The structure of the material is called the "lattice," an arrangement where the atoms form a crystalline structure which supports the alloy's tunable

properties. Defects in the material arise when lattices with disparate atomic spacing ("lattice mismatch") are grown atop one another, disrupting the ordered nature of the atoms within the lattice and causing the semiconductor to behave un-ideally.

### 1.3.1 MCT Growth

Historically, infrared MCT arrays have been grown epitaxially (one layer atop another, from the Greek *epi-* meaning "above" and *taxis* meaning "in an ordered fashion") on cadmium-zinc-telluride (CdZnTe or CZT) substrates. These substrates provide excellent lattice matching to MCT, resulting in absorber layers with very low defect density. Low defect density is critical because dark current in these detectors scales strongly with the concentration of mid-gap traps. Unfortunately, CZT remains expensive and difficult to produce in large areas; typical wafers measure only 10–100 $cm^2$. To overcome the size and cost limitations of CZT, substantial efforts in the late 1980s and early 1990s focused on heteroepitaxial growth (epitaxial growth of unlike materials) of MCT directly on silicon substrates [6, 7, 8]. Silicon wafers are far less expensive and readily available in diameters exceeding twelve inches ($\geq$700 $cm^2$), making them highly attractive for large-format focal-plane arrays.

The "standard" method for MCT is direct epitaxial growth on lattice-matched CZT, usually by molecular beam epitaxy (MBE). Early IR detectors were grown using primarily liquid phase epitaxy (LPE) which provided less defective material growth, but the need for accurate doping profiles and larger arrays brought MBE into dominance. The growth method used to grow MCT on alternative substrates (Si, GaAs, Ge) requires one or more buffer layers to bridge the large mismatch between materials. These buffer layers and serve to terminate dislocations that arise at the interface between the poorly-matched substrates. A common choice of buffer material is CdTe, often grown thick to terminate defects and allow the lattice to recover into a more stable crystal structure [8].

The detectors characterized in this thesis were grown using Raytheon's most recent MCT-on-Si process, which inserts thick buffer layers (ZnTe and CdTe) between the silicon substrate and the MCT absorber to mitigate dislocations arising from the large lattice mismatch [1, 9, 10].

This same buffer-layer approach was developed in parallel with the MCT-on-CZT detectors supplied for the VISTA observatory, although performance testing at the time revealed an excessively high dark current tail for that particular application [9, 6].

This elevated dark current arises primarily from threading dislocations generated by lattice mismatch between the substrate and the epitaxial layers [11, 12, 13]. Such mismatch becomes especially severe when the constituent materials exhibit substantially different lattice constants, as illustrated in Figure 1.1 for numerous semiconductor alloys of interest. Two ternary alloys—CZT and MCT—are included for reference, although their exact lattice constants and bandgaps vary with alloy composition.

The conventional growth approach (*i.e.*, MCT grown on lattice-matched CZT substrates) minimizes mismatch and therefore defectivity. Precise adjustment of the cadmium mole fraction in the CZT substrate places its lattice constant between those of ZnTe and CdTe, as shown in Figure 1.1. Similarly, MCT lies between CdTe and HgTe. This plot also explains the widespread use of MCT in infrared detectors: the large separation in bandgap along the y-axis between HgTe and CdTe enables continuous tuning over a broad range of cutoff wavelengths. By finely controlling the cadmium fraction in the CZT substrate, state-of-the-art detectors (for example, Teledyne's HxRG series) achieve near-perfect lattice matching with the MCT absorber, thereby attaining extremely low defect densities.

The detectors developed for the SATIN program had to overcome the large lattice mismatch between silicon and MCT. This challenge was addressed by growing two buffer layers on the silicon wafer before depositing the MCT absorber. The growth sequence consists of a ZnTe layer on the silicon substrate, followed by a CdTe layer, and finally the HgCdTe device structure. This layered approach has proven effective at terminating the majority of threading dislocations at the heterointerfaces [1].

After completion of the full epitaxial stack, most of the buffer material is removed by selective etching. Only a small amount of CdTe is retained on the backside of the MCT, and this residual layer is subsequently passivated to suppress surface states that would otherwise generate significant dark current. One consequence of retaining this CdTe layer is that it

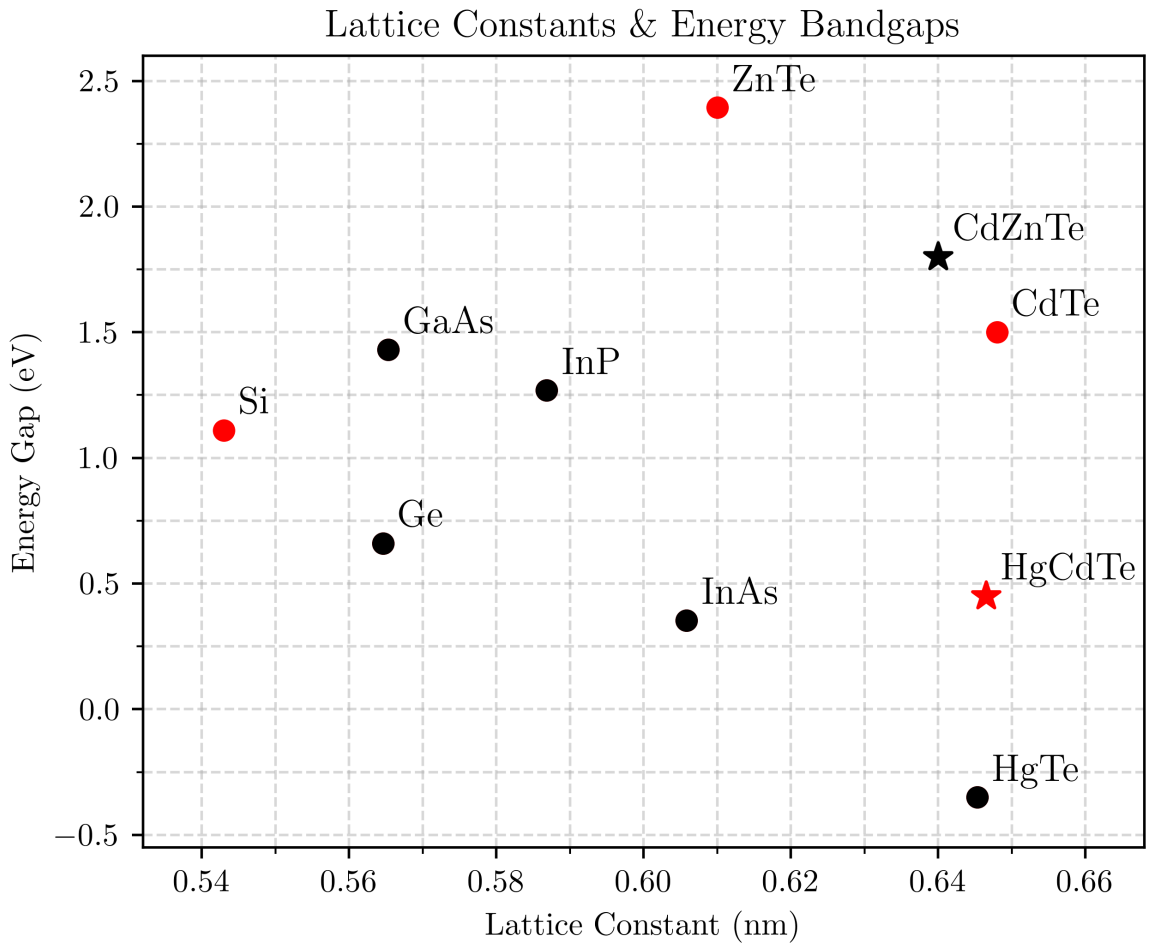


Figure 1.1: The figure displays lattice constants and energy bandgaps for several semiconductor alloys commonly employed in detector fabrication. The positions of the ternary alloys CZT and MCT vary with cadmium mole fraction. Note the negative y-axis value of HgTe; HgTe is a semimetal, which has overlapping energy bands, unlike the other semiconductors shown.

imposes a short-wavelength quantum-efficiency cutoff near 800 nm.

### 1.3.2 Consequences of Defective Detector Material Use

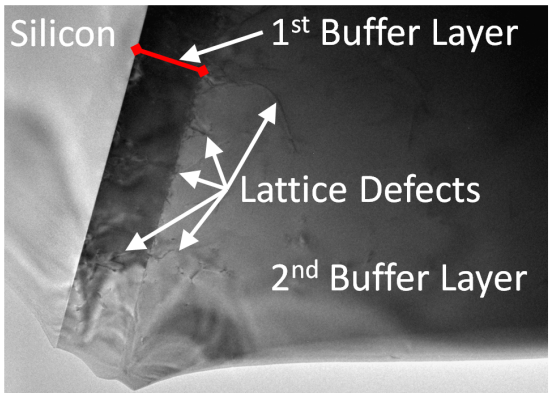


(a) A high resolution scan of a die sample showing the buffer silicon substrate and two buffer layers, demonstrating the higher defect density in the first buffer layer and termination of defects in the second buffer layer.

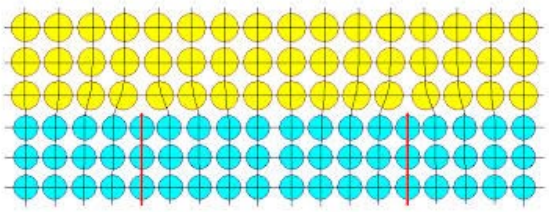

(b) A simple depiction of the boundary between two lattice material layers, showing how dislocations form due to lattice mismatch.

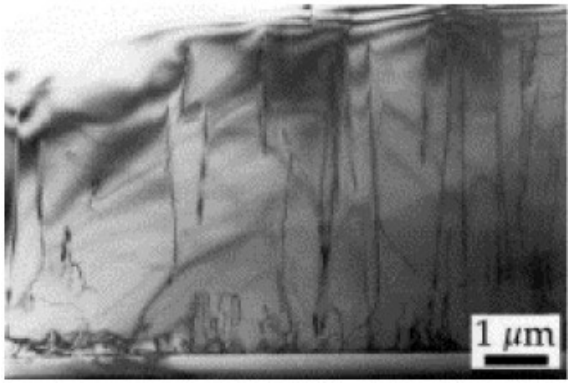


(c) A cross-sectional scan of mismatched materials grown atop one another, showing how defects grow upward into the MCT.

Figure 1.2: This figure shows scans of defective materials and a diagram of mismatched lattice growth that causes defects. All figures are from Hanold et al. 2015 [1].

Figure 1.2 shows a diagram of threading dislocation formation between two mismatched materials and two scans of actual MCT with threading dislocation formation. As mentioned prior, these threading dislocations have a number of consequences for detectors. They increase the fraction of bad pixels in a detector, increase persistence, cause long tails on dark current distributions, and make the resulting device performance more reliant on the size of the p-n junction implant. Material defects in MCT, specifically dislocations, are well known to reduce detector performance in these ways [1, 14, 13, 15, 4, 16].

Dislocation density is often estimated by a count of the etch pits (surface pitting of the material) that result when defective substrate or buffer layers are etched away during the

growth process. Measurements of the etch pit density (EPD) yield an estimate of the number of threading dislocations that permeate into the MCT. It is well established that defect densities less than approximately $10^5\,\mathrm{cm}^{-2}$ have little to no effect on device performance [14, 4]. The EPD of the devices tested in this thesis are proprietary to Raytheon, but significantly higher than this threshold.

Defects that are present in the active region of the detector warp the electric field of the pixel and cause pixels to become completely inoperative. If the density of this type of defect is particularly high, pixel yield can drop drastically. Defects can also introduce traps into the band structure of the p-n junction, allowing trap-assisted tunneling across the junction (See Section 2.2.3) to become significantly more common than expected. Multiple defects in the same pixel can contribute cumulatively to this effect, causing dark current distributions to have very long Poisson tails, shown later in Section 3.4.5. Traps also increase persistence by capturing photogenerated charge in one exposure and releasing it in later ones, which is discussed in Section 3.3. The trap density affecting the detectors so strongly when defects are present in the active region of the pixel (*i.e.* within the pixel implant area) also means that detectors with smaller implants will contain fewer defects, and thus result in higher pixel yield. This is apparent in the detectors used for this thesis, where larger pixel implant size directly correlates to both reduced pixel performance and reduced pixel yield.

### 1.3.3 MCT Architecture

MCT photodiode architecture is split between two types: planar structures and mesa structures [8]. Figure 1.3 shows simple schematic diagrams of the two structures. Planar structures are simpler and cheaper to produce than mesa structures, which require deep etching to isolate the individual pixels from one another. However, the reduced cost of planar structures comes with downsides for the focal plane array, namely increased crosstalk. In contrast, mesa structures benefit from excellent pixel isolation and allow for more complex structures and doping profiles [8].

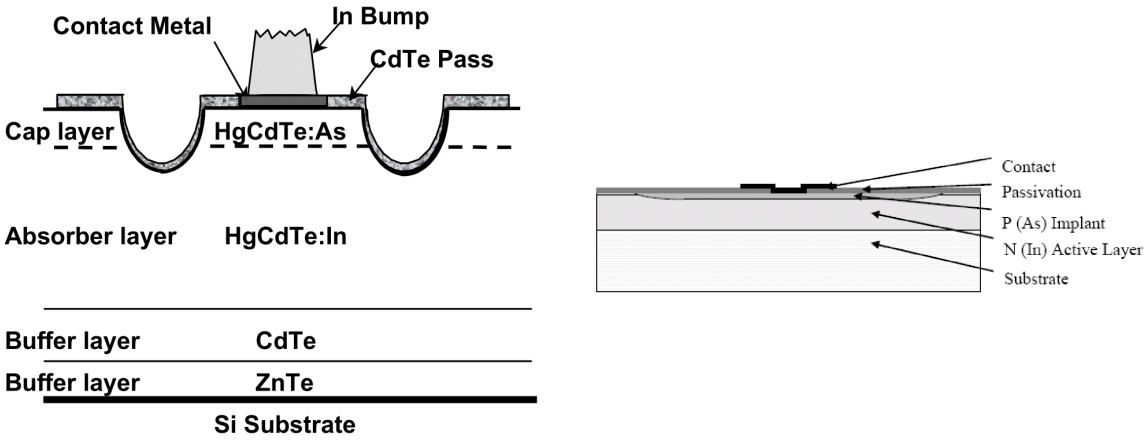


Figure 1.3: The figure displays two simple diagrams of the mesa and planar pixel structures. The figures are from [9, 17].

## 1.4 The SATIN Detector Development Program

The SATIN (SWIR Advanced Technology Instruments for NSF and NASA) program was a two-phase development effort funded jointly by NSF and NASA to improve the performance of MCT detectors grown on silicon substrates for astrophysical applications. Phase I supported the fabrication of two detector lots. The first lot was comprised of two 2048×2048 arrays—one grown on CZT (designated 9A) and one on silicon (VIRGO-14)—together with five variable-unit-cell (VUC) test devices (V1–V6). The 9A and VIRGO-14 arrays established the performance baseline for subsequent lots. Each VUC device contained four quadrants with different mesa sizes; characterization of these quadrants directly informed the design of the second Phase I lot, which consisted of three detectors (F3, F6, and VTHIN1) with 17 $\mu$m mesas. Although this second lot satisfied nearly all original program goals, the measured dark current remained approximately a factor of three higher than the target value.

Phase II continued the development with three additional fabrication rounds. The first round evaluated two new substrate-removal and annealing processes. The second round focused on reducing the dark current tail by limiting defect propagation from the buffer layers into the absorber. The third and final round introduced a shift from the mesa architecture used throughout Phase I to a planar architecture. This final lot produced eight devices, designated V21 through V28. The results presented in this thesis are based primarily on V23,

which is the highest-performing detector from this lot. The work performed for this thesis extend many of the results from the early testing phases of the SATIN project, with particular focus on a true measurement of the dark current in the best pixels of the newest devices. The impact of p-n junction implant size is assessed for the first time in this thesis, demonstrating both the successes and issues of using smaller junction implants.

V23 is the only device from the final SATIN lot that arrived at RIT without major mechanical damage. A packaging failure during shipment from Raytheon damaged most detectors in the lot. Although all devices were returned to Raytheon for wire-bond repair, the cosmetic and surface damage remained. V23 suffered the least surface damage and has therefore served as the primary subject of our characterization work. Figure 1.4 shows a quadrant map and a high-resolution scan of V23. The numbers on each quadrant indicate the pitch (side length) of the square p-n junction implants within each 20$\mu$m pixel in the respective quadrant. The size of the implant affects the field structure of the pixel, determines the dominant sources of capacitance within the pixel, and determines how many material defects affect the active region of the pixel.

### 1.4.1 Materials and Dopants

The SATIN detectors employ a p-on-n $Hg_{1-x}Cd_xTe$ heterostructure in which p-type material doped with arsenic is implanted into the n-type layer doped with indium. The exact doping concentrations and profiles remain proprietary to Raytheon. Nevertheless, several key material parameters can be inferred from measured device performance, including the cadmium mole fraction $x$ and the dielectric constant $\epsilon$.

The cadmium mole fraction $x$ is the primary determinant of the detector cutoff wavelength. An empirical expression for the temperature-dependent bandgap $E_g$ (in eV) of $Hg_{1-x}Cd_xTe$ was derived by Hansen *et al.* [18]:

$$E_g(x,T) = -0.302 + 1.93x + 5.35 \times 10^{-4}T(1-2x) - 0.810x^2 + 0.832x^3, \tag{1.4.1}$$

where $x$ is the mole fraction and $T$ is the temperature in kelvin (typically 70 K for the mea-

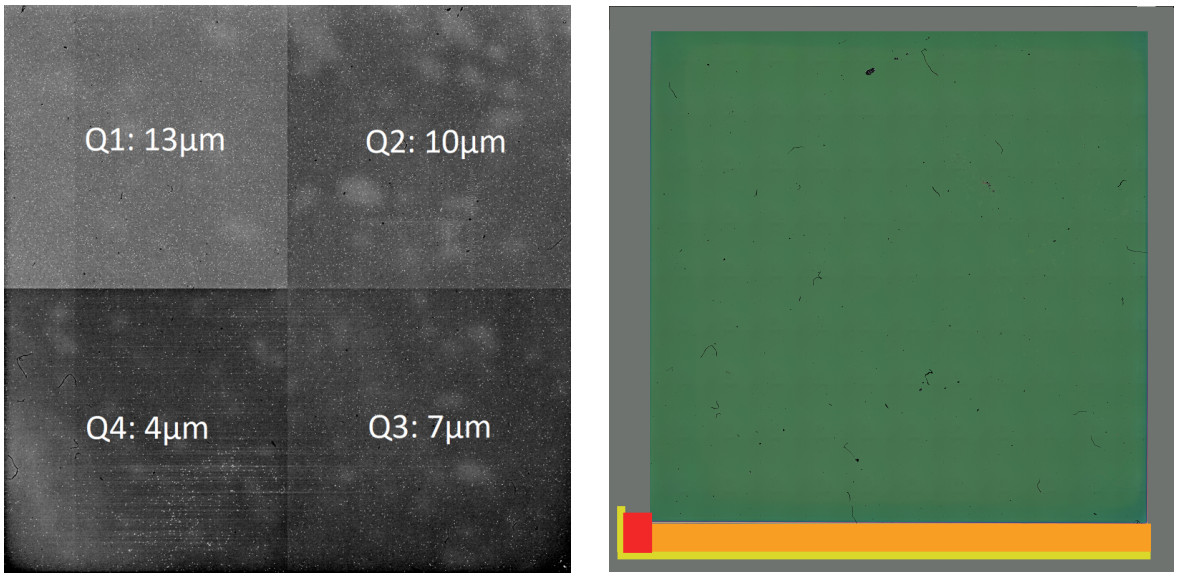


Figure 1.4: Left: A quadrant map of V23 indicating the p-n junction implant sizes in each quadrant. Right: A high-resolution optical scan of V23 with edge circuitry and identifying markings redacted. The yellow region marks the wire-bond attachment pads to the ROIC, the orange region covers the column output circuitry, and the red region covers the clocking and protection circuitry.

surements presented here). The measured cutoff wavelength of V23 is 2750 nm, and thus the corresponding bandgap is

$$E_g = \frac{hc}{\lambda q} = 0.451\,\text{eV}, \tag{1.4.2}$$

where $h = 6.626 \times 10^{-34}\,\text{J/Hz}$ is Planck's constant, $c = 2.998 \times 10^{8}\,\text{m/s}$ is the speed of light, and $q = 1.6 \times 10^{-19}\,\text{J/eV}$ is the elementary charge. Substituting $E_g = 0.451\,\text{eV}$ and $T = 70\,\text{K}$ into Equation (1.4.1) and solving the resulting cubic equation for $x$ yields a single physically meaningful root:

$$x = 0.431. \tag{1.4.3}$$

### 1.4.2 ROIC Structure

The VIRGO readout integrated circuit (ROIC) employs a three-transistor (3T) pixel architecture, shown schematically in Figure 1.5. The three transistors perform the following functions: the select transistor (SEL) connects the pixel to the column bus during readout, the reset gate transistor (RG) restores the integration node to the nominal reset voltage after readout, and

the source-follower transistor (SF) buffers the photodiode signal within the pixel [19]. The detector common bias is labeled VDETCOM, the source-follower drain supply is VNUC, and the reset voltage is VRSTUC. Table 1.1 shows some values used in normal operation of the V23 detector; Applying the voltages in the table results in an applied reverse bias $V_R$ of -1.0 V. When modifying the total bias across the junction, the common voltage VDETCOM is maintained at 1.0 V, and VRSTUC is increased. This reduced bias allows us to modify the effective size of the p-n junction, which will be useful in testing persistence within the detector later.

| Name | Voltage | Unit |
|---|---|---|
| VRSTUC | 0.002 | V |
| VDETCOM | 1.002 | V |
| VNUC | 0.9 | V |
| VPUC | 3.5 | V |
| VNOUT | 2.5 | V |

Table 1.1: This table shows some common voltages for nominal operation of the V23 detector.

Although the exact physical layout of the ROIC components is proprietary to Raytheon, their general placement can be inferred from the known 3T architecture and from similar designs reported in the literature. The photodiode resides in the HgCdTe layer, where the p-n junction meets the indium bump (IB) that hybridizes the detector array to the ROIC. To the right of each pixel lies the column bus. The column slew current source is denoted ISLEW, the analog supply for the column current source is VPUC, the output source-follower return is VNOUT, and COL leads to a second source-follower stage that requires an external current source $I_{\text{ext}}$.

### 1.4.3 ROIC Operation

The VIRGO ROIC is operated by the readout electronics. In the course of imaging with a detector the electronics this includes biasing the detector to the nominal voltage, resetting it between exposures, and sampling the signal integrated by the pixels. The voltage applied to the pixel upon reset is the difference of VRSTUC and VDETCOM – the "reverse bias" – is $V_r =$ VRSTUC − VDETCOM.

Aside from setting the voltages required to operate the detector, the electronics also control

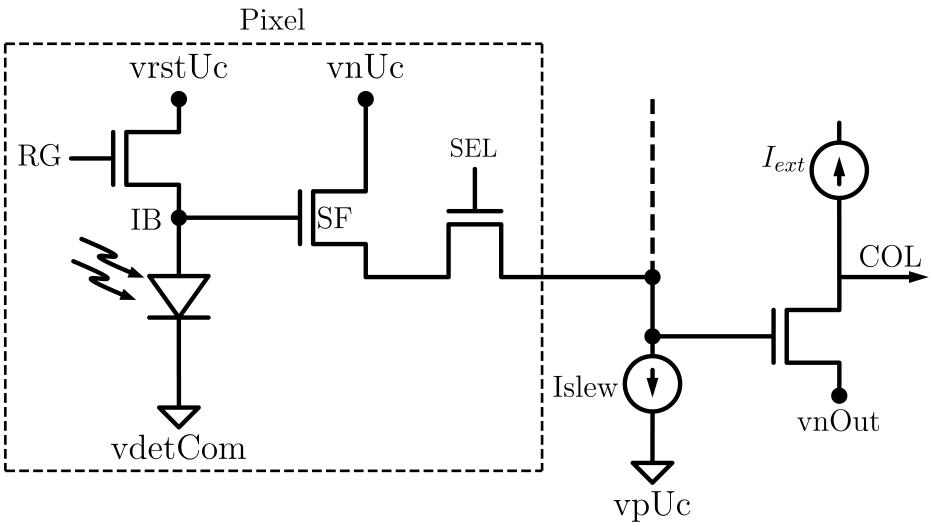


Figure 1.5: The figure shows the 3T pixel architecture used in the VIRGO ROIC. The three transistors are labeled SEL (select), RG (reset gate), and SF (source follower).

how readout of the detector array is carried out. For most use-cases a standard up-the-ramp (UTR) sampling scheme is used, where the array is reset once and then non-destructively read out a user-specified number of times. Readout configurations are denoted UTR,X,Y,Z, where X is the total number of frames in the ramp, Y is the number of non-destructive reads performed per frame, and Z is the number of dropped (skipped) frame periods between successive saved frames. In all use cases for this thesis, Y=1, while X is modified to increase the number of frames in each ramp and Z is modified to increase the integration time of individual frames.

The dropped-frame count Z directly controls the effective integration time per saved frame in multiples of the basic array readout period (0.9924 s). For example, a five-frame ramp with approximately 1 s integration per frame (no dropped frames) is executed as UTR,5,1,0. A five-frame ramp in which each frame (except the initial reference frame) integrates for 1000 s is executed as UTR,5,1,999. In this final case, this means that the detector is reset, a 1 second frame is taken, followed by 4 frames with 1000 second integration times.

The electronics are also capable of more advanced readout schemes; One such scheme was created for the persistence experimentation presented in this thesis. In this mode the integration time per frame increases progressively until a maximum value is reached, after which an arbitrary number of frames are acquired at that maximum integration time. A

typical long ramp, for example, consisted of UTR frames with integration times of 1, 2, 5, 10, 20, 50, 100, 200, and 500 s, followed by ten frames at 1000 s each. This mode and its relevance is further discussed in Section 3.3.2.

## 1.5 Limitations of Detector Technology

Detectors are limited primarily by the following phenomena: dark current, persistence, quantum efficiency, non-linearity, crosstalk, and ROIC glow. Dark current generates false signal in the absence of light, persistence causes signal to carry over from one image to another, quantum efficiency determines how effectively a detector can absorb light, non-linearity and crosstalk affect how accurately the true signal of a pixel can be measured, and ROIC glow contaminates data with light generated by the electronic components within the detector.

### 1.5.1 Challenges of IR Detector Fabrication

Infrared detectors are particularly challenging to make, given that they depend on relatively brittle materials and complex equipment to manufacture. As mentioned prior, the growth and etching processes for infrared detectors are imperfect and introduce additional issues via defects. The processes must be carefully controlled to ensure high pixel yield. Depending on the application, the concentrations of dopants in the detector material need to be carefully controlled. Doping gradients are often needed to ensure proper function of the device, and the curves and severity of these gradients vary wildly depending on the desired application.

### 1.5.2 Current State-of-the-Art IR Detectors

Current state-of-the-art infrared detector technology is exceptionally advanced. They achieve performance that early IR detector scientists could only dream of, and come in array sizes orders of magnitude larger than was possible just a few decades ago. Improvements in semiconductor processes have yielded smaller pixel sizes, precise dopant grading, and improved ROIC technology. The Teledyne HxRG detector line is generally accepted as the overall best in the category. The dark current in modern detectors is immeasurably low and believed to

be largely dominated by ROIC glow as opposed to actual dark current mechanisms [20, 21]. They exhibit crosstalk between nearest neighbor pixels less than 3%, high quantum efficiency across their entire wavelength detection range, and extremely low persistence.

Teledyne has put a large amount of resources into ROIC development and package integration, with particular effort put into improving detector buttability for large arrays. This is particularly attractive for astrophysics, where array fill-factor determines the overall size and weight of FPA, both of which drastically affect the overall cost of space missions.

The greatest shortcoming of these devices is their cost. Individual detectors sell for upwards of $1,000,000, and often cost more if purchased in small quantities. This cost arises largely from a lack of competition and the high cost of the CZT substrates used to manufacture the detectors. Additionally, for many ground-based applications, the detector performance is far better than required to perform the observations that small observatories perform. A lower-cost alternative to the HxRG devices, even with worse performance, would introduce a much-needed alternative for users that don't have access to the kind of funding that major observatories have access to.

## 1.6 Thesis Goals

The primary goal of the testing performed for this thesis is to demonstrate that MCT-on-Si devices are a promising candidate for inexpensive astronomy FPA. The results show that the performance of these devices is far closer to that of state-of-the-art arrays than previously believed, and with further development could feasibly compete in the astronomy detector space. This thesis demonstrates that despite the inherent issues tied to the mismatched material growth, the device performance is primarily limited by the ROIC and electronics. A detector of this type with improved passivation and ROIC would not challenge state-of-the-art devices for the most demanding applications; It would, however, be an excellent competitor for ground-based and background limited observations, at a price point far below that of current state-of-the-art.

The remainder of this thesis is structured as follows: Chapter 2 discusses the underlying

theory of pixel physics as they relate to operation and noise, Chapter 3 presents the results of testing carried out for the SATIN detectors, Chapter 4 presents the results of a brief observing program carried to demonstrate on-sky performance, and Chapter 5 summarizes the results and presents conclusions.

# Chapter 2

# Theory

## 2.1 p-n Junction Theory

The p-n junction forms the core of every detector pixel and enables the integration and collection of photogenerated charge. Modern semiconductor detectors would not exist without it. A brief review of p-n junction physics is therefore essential for understanding the operation of virtually all semiconductor-based active-pixel sensors.

### 2.1.1 Properties of the p-n Junction

A p-n junction forms when a p-doped semiconductor region, containing a high concentration of mobile holes from acceptor impurities, is brought into direct contact with an n-doped region, which contains a high concentration of mobile electrons from donor impurities (Figure 2.1a). In reality the junction is created by growth or implantation of the relevant ion in the material, and is not actually a joining of two separately doped materials, but the following "contact" analogy allows for a simpler discussion of the creation of the junction. Immediately after contact, electrons diffuse from the n-side into the p-side, and holes diffuse from the p-side into the n-side. The holes are not true particles, and only "move" in the sense that their apparent location changes as the electrons occupy one hole and leave another behind. This carrier diffusion uncovers fixed, uncompensated charges: positively charged donor ions ($N_d^+$) on the n-side and negatively charged acceptor ions ($N_a^-$) on the p-side. The resulting charge

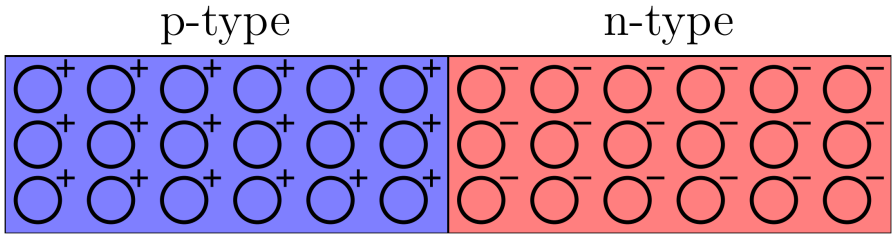


(a) A theoretical p-n junction at the moment the p-type and n-type materials are joined, with symbols representing the donor and acceptor ions. In reality, one layer is grown atop another or implanted into it, but this representation is a useful tool for understanding how the depletion region evolves.

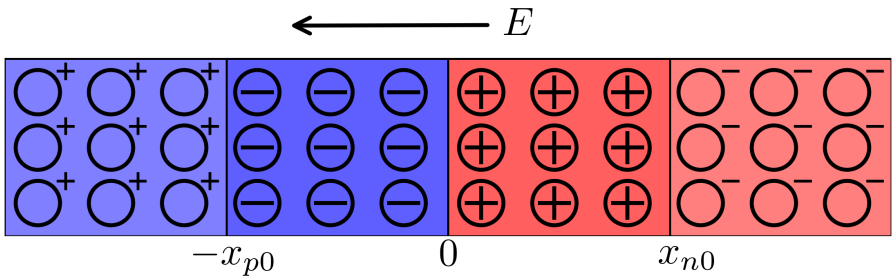


(b) The p-n junction shortly after the initial joining, after the diffusal of free carriers across the junction. The depletion region is now populated by uncompensated acceptor and donor atoms. The carriers stripped from the dopant atoms neutralize a small number of dopant atoms just outside of the depletion region, shown in Figure 2.5.

Figure 2.1

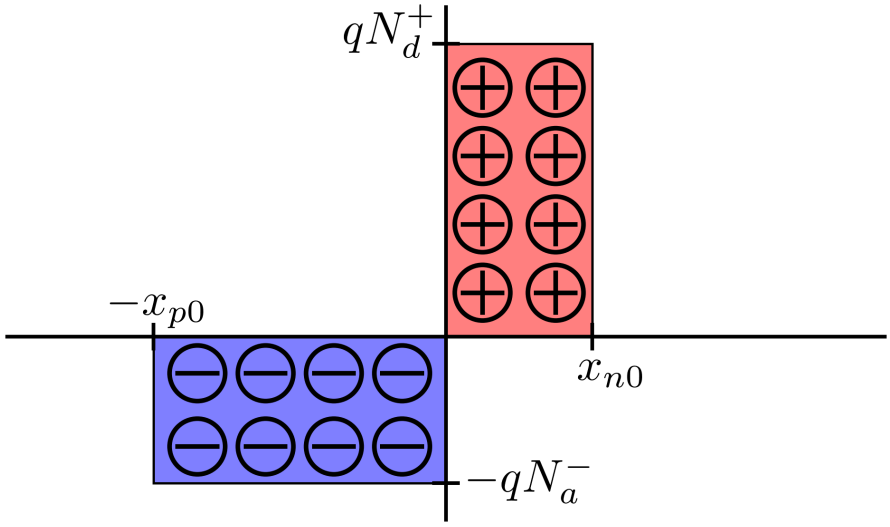


(a) A charge density distribution for the p-n junction at equilibrium. The abrupt borders at $x_{p0}$ and $x_{n0}$ due to carrier depletion within the depletion region and neutrality outside it are an approximation; In reality, the edge is a sharp gradient.

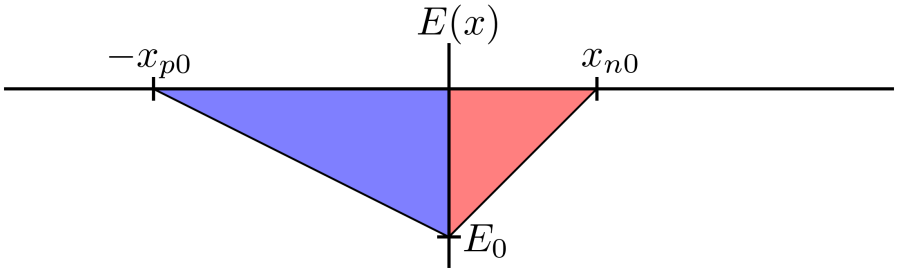


(b) A depiction of the strength of the electric field within the depletion region of the p-n junction, with a peak strength of $E_0$.

Figure 2.2

separation establishes a depletion region devoid of mobile carriers and produces a built-in electric field directed from the n-side to the p-side (Figure 2.1b) [22].

Although the depletion region is often drawn symmetrically for simplicity, the depletion widths on the two sides are generally unequal ($x_{p0} \neq x_{n0}$). This asymmetry arises because charge neutrality requires the total positive charge on the n-side to equal the magnitude of the total negative charge on the p-side ($Q_+ = |Q_-|$), while the doping concentrations themselves are typically very different ($N_a \neq N_d$, often by orders of magnitude). Figure 2.2a and Equation 2.1.1 show that the total uncompensated charge on either side of the junction is equal:

$$Q_+ = |Q_-| \implies qAN_d^+ x_{n0} = qAN_a^- x_{p0} \tag{2.1.1}$$

where $A$ is the cross-sectional area of the junction. Importantly, this charge-balance equation simplifies to $N_d x_{n0} = N_a x_{p0}$, which will be useful below (note that $N = N^{+/-}$ as the density of ions is an intrinsic property of the physical material). The maximum strength of the electric field $E_0$ in Figure 2.2b can be calculated by integration for either side of the p-n junction:

$$\frac{dE}{dx} = \frac{qN_d}{\epsilon\epsilon_0}, \quad 0 < x < x_{n0} \implies \int_{E_0}^{0} dE = \frac{qN_d}{\epsilon\epsilon_0} \int_0^{x_{n0}} dx \implies E_0 = -\frac{qN_d}{\epsilon\epsilon_0} x_{n0} \tag{2.1.2}$$

$$\frac{dE}{dx} = \frac{qN_a}{\epsilon\epsilon_0}, \quad -x_{p0} < x < 0 \implies \int_0^{E_0} dE = \frac{qN_a}{\epsilon\epsilon_0} \int_{-x_{p0}}^{0} dx \implies E_0 = -\frac{qN_a}{\epsilon\epsilon_0} x_{p0} \tag{2.1.3}$$

The built-in potential $V_0$ across the depletion region can be obtained by integrating the electric field, $E(x) = -\mathrm{d}V/\mathrm{d}x$, or equivalently by evaluating the area under the electric-field profile shown in Figure 2.2b:

$$V_0 = -\frac{1}{2}\left(x_{p0}E_0 + x_{n0}E_0\right) = -\frac{1}{2}E_0 W_{\mathrm{dep}} \tag{2.1.4}$$

where $W_{\mathrm{dep}} = x_{p0} + x_{n0}$ is the total width of the depletion region. Substituting Equation 2.1.2 for $E_0$:

$$V_0 = \frac{1}{2}\frac{q}{\epsilon\epsilon_0} N_d x_{n0} W_{\mathrm{dep}} \tag{2.1.5}$$

Recalling that $N_d x_{n0} = N_a x_{p0}$ and $W_{\text{dep}} = x_{p0} + x_{n0}$, we can solve for $x_{n0}$ as:

$$x_{p0} = x_{n0}\frac{N_d}{N_a} \implies W_{\text{dep}} = x_{n0}\left(1 + \frac{N_d}{N_a}\right) = x_{n0}\left(\frac{N_a + N_d}{N_a}\right) \implies x_{n0} = \frac{W_{\text{dep}} N_a}{N_a + N_d} \quad (2.1.6)$$

and make a final substitution into Equation 2.1.5 to get the intrinsic potential across the junction:

$$V_0 = \frac{qN_d N_a}{2\epsilon\epsilon_0(N_d + N_a)} W_{\text{dep}}^2 \quad (2.1.7)$$

where $N_a$ is the concentration of acceptor ions in the p-type material, $N_d$ is the concentration of donor ions in the n-type material. Under the assumption of a linearly graded junction, $V_0$ can be calculated independently of $W_{\text{dep}}$ [23, 22], or even just approximated as $V_0 = E_g/q$ [24, 25]:

$$V_0 = \frac{kT}{q}\ln\left(\frac{N_a N_d}{n_i^2}\right) \quad (2.1.8)$$

where $n_i$ is the intrinsic carrier concentration of the parent material due to thermal excitation of electrons from the valence to the conduction band [26]. $n_i$ is given by:

$$n_i = (5.585 - 3.820x + 1.753 \times 10^{-3} xT)\left[10^{14} {E_g}^{3/4} T^{3/2} e^{-\frac{E_g}{2k_b T}}\right] \quad (2.1.9)$$

where $x$ is the cadmium mole fraction, $T$ is the temperature in Kelvin, and $E_g$ is the bandgap energy of the MCT material [18]. $W_{\text{dep}}$ can be derived by solving Equation 2.1.7 for:

$$W_{\text{dep}} = \left[\frac{2\epsilon\epsilon_0(V_0 - V_a)}{q}\left(\frac{N_a + N_d}{N_a N_d}\right)\right]^{\frac{1}{2}} \quad (2.1.10)$$

where $\epsilon$ is the dielectric constant for the detector material, $\epsilon_0 = 8.85 \times 10^{-12}\,\text{F/m}$ is the vacuum permittivity, $q = 1.6 \times 10^{-19}\,\text{C}$ is the elementary charge. $V_a$ is a variable added to represent any externally applied voltage, and for $Hg_{1-x}Cd_xTe$, $\epsilon \approx 20.5 - 15.5x - 5.7x^2$, where $x$ is the cadmium mole fraction [15, 27, 28].

A p-n junction is forward-biased when the p-region is held at a positive voltage relative to the n-region. In this regime the potential barrier is reduced, the depletion region narrows,

and current can flow across the junction. Conversely, the junction is reverse-biased when a negative voltage is applied to the p-region relative to the n-region. The depletion region then widens and only a very small saturation current flows. The ideal diode equation that describes this behaviour is:

$$I_{\text{ideal}} = I_0 \left( \exp \left[ \frac{qV}{kT} \right] - 1 \right), \tag{2.1.11}$$

where $I_0$ is the reverse saturation current, $q$ is the elementary charge, $V$ is the applied voltage (positive for forward bias), $k$ is Boltzmann's constant, and $T$ is the absolute temperature.

The ideal diode equation holds until the reverse bias reaches a critical magnitude, at which point the junction undergoes reverse breakdown and large currents flow. Figure 2.3 shows the current–voltage characteristic of a p-n junction, illustrating exponential current increase under forward bias and breakdown at large reverse bias.

Figure 2.4a presents the equilibrium band diagram of the p-n junction, while Figure 2.4b shows the band diagram under an applied reverse bias $V_r$. The potential difference between the conduction (and valence) bands in the p- and n- regions is proportional to $V_0 - V_r$, while the depletion width increases with the square root of this potential difference, as given in Equation (2.1.10). As the reverse bias magnitude increases, the bands tilt more steeply and the probability of band-to-band tunneling rises significantly. This mechanism will be examined as a source of dark current in Section 2.2.3.

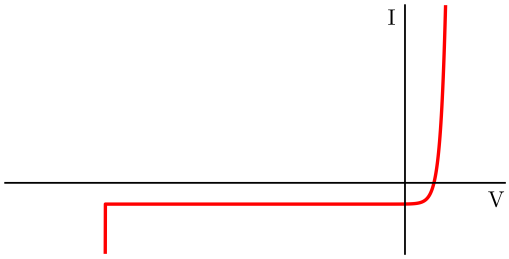


Figure 2.3: This figure shows the current–voltage characteristic of a p-n junction, illustrating exponential current increase under forward bias and breakdown at large reverse bias.

### 2.1.2 Capacitance of a p-n Junction

The p-n junction under reverse bias behaves like a parallel-plate capacitor. The associated depletion capacitance $C_{\text{dep}}$ depends on both the junction area and the depletion width. It

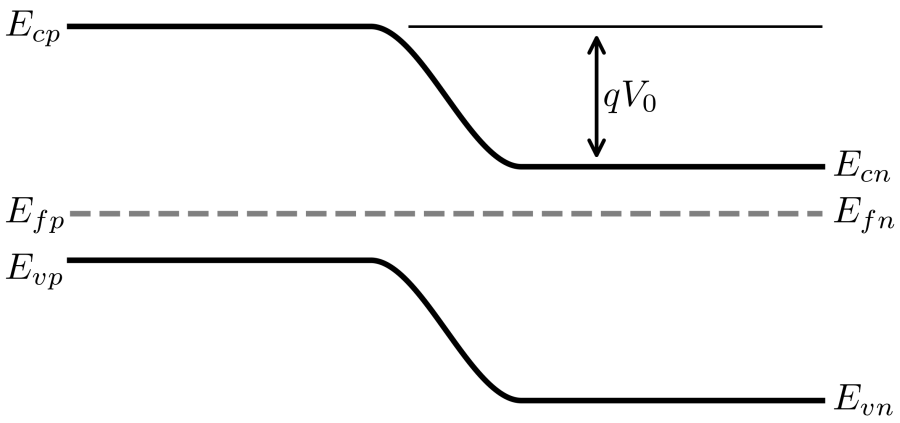


(a) The figure shows the band diagram of a p-n junction at equilibrium. The conduction-band edge is labeled $E_c$, the valence-band edge is $E_v$, and the Fermi level is $E_f$. Subscripts $p$ and $n$ denote the p-side and n-side of the junction, respectively.

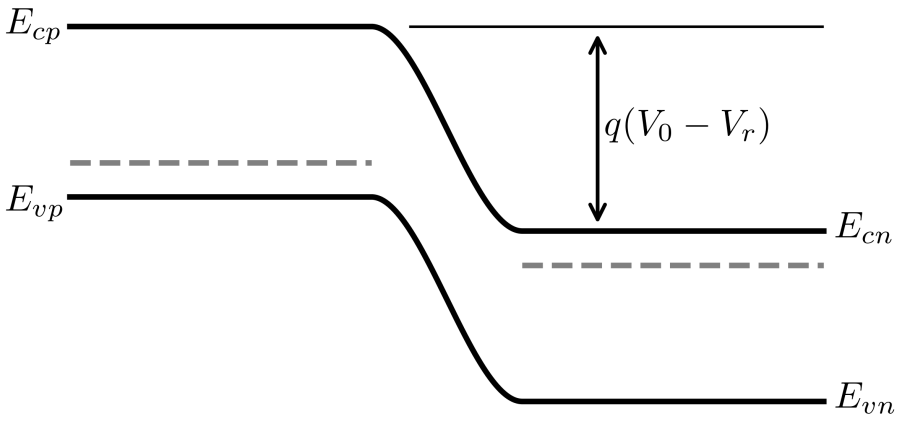


(b) The figure shows the band diagram of a p-n junction under an applied reverse bias $V_r$. The Fermi levels remain at approximately the equilibrium value in its respective neutral region; $E_{fp}$ and $E_{fn}$ are separated by the applied voltage from one another.

Figure 2.4

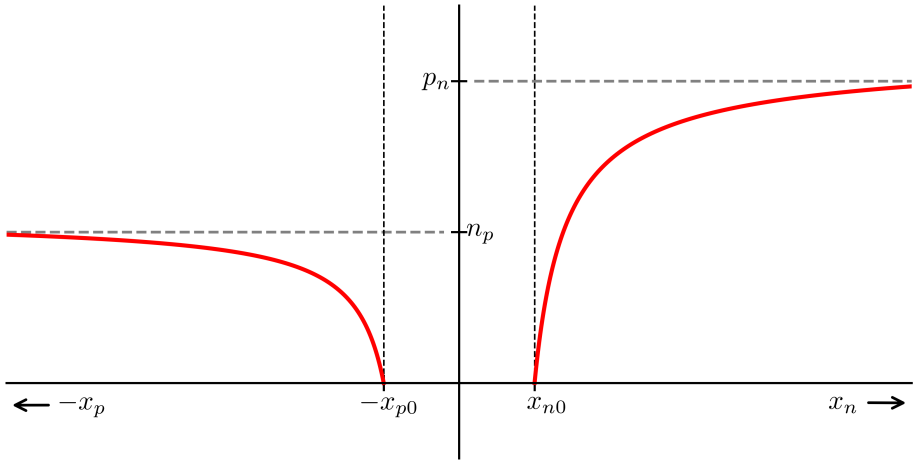


Figure 2.5: This figure shows a diagram of minority carrier distribution in the neutral regions that surround the depletion region of the p-n junction.

consists of two contributions: the bottom-junction capacitance $C_b$ (Equation (2.1.12)) and the sidewall capacitance $C_s$ (Equation (2.1.13)). The total depletion capacitance is therefore $C_{\text{dep}} = C_b + C_s$.

$$C_b = \frac{\epsilon\epsilon_0 A}{W_{\text{dep}}} \left(1 - \frac{V}{V_0}\right)^{-m_b} \tag{2.1.12}$$

$$C_s = \frac{\epsilon\epsilon_0 A_s}{W_{\text{s}}} \left(1 - \frac{V}{V_0}\right)^{-m_s} \tag{2.1.13}$$

where $V_0$ is the intrinsic potential of the junction, $V$ is the voltage across the junction when accounting for the reverse bias and integrated charge, $W_s$ is the sidewall depletion depth, $A_s = Pd$ is the area of the sidewall component which is the product of the perimeter $P$ of the implant and the depth $d$ of the implant, $A$ is the bottom area of the p-n junction, and $m_s$ and $m_b$ are junction grading coefficients for the sidewall and bottom gradients, respectively. There are additional sources of capacitance in each pixel arising from the MOS gate ($C_g$) and other sources of parasitic capacitance, though modeling them is rather difficult without knowledge of grading profiles, ROIC component locations, and other proprietary detector parameters. For the purposes of the modeling within this thesis, the gate capacitance is modeled as such:

$$C_g = \frac{\epsilon\epsilon_0 LW}{Z} \left(1 - \frac{V}{V_0}\right)^{-m_g} \tag{2.1.14}$$

where $L$ and $W$ are the length and width of the gate implant, $Z$ is the thickness of the gate, and $m_g$ is a scaling factor.

The capacitance of the pixel depends strongly on the size of the junction implant, and affects a number of detector parameters, namely the conversion gain and linearity. From Equation (2.1.15) the reciprocal of this capacitance represents the voltage response per unit charge. Consequently, as charge accumulates in the pixel the incremental sensitivity to additional photoelectrons decreases. This well-documented effect is commonly known as pixel non-linearity [29, 30, 31, 32, 33].

$$C_{\text{dep}} = \left| \frac{\mathrm{d}Q}{\mathrm{d}(V_0 - V_r)} \right| \implies \left| \frac{\mathrm{d}(V_0 - V_r)}{\mathrm{d}Q} \right| = \frac{1}{C_{\text{junc}}} \tag{2.1.15}$$

The change in the voltage response (conversion gain) of the detector as charge is integrated leads to "non-linearity." In an ideal detector, the conversion gain from electrons to volts is the same when the pixel is empty as it is when the pixel is nearly saturated. The best detectors have nearly perfectly linear response across their entire dynamic range. If the response changes significantly as charge is integrated, the non-trivial problem of linearity correction becomes a significant issue for data reduction.

In the models presented in this thesis, the gate capacitance is used as an effective lumped parameter that accounts for multiple parasitic capacitance contributions. Accurate modeling of the various capacitance contributions within a pixel is highly complex, even when the pixel and ROIC geometry are fully known. (Entire PhD theses have been devoted to this subject; see, for example [34, 35].) A discussion of the dominant capacitance terms and their impact on detector linearity is presented in Section 3.6.

### 2.1.3 Charge Generation and Collection within the p-n Junction

When a photon with energy greater than the bandgap $E_g$ is absorbed in the detector, it excites an electron from the valence band to the conduction band, generating a free electron–hole pair. Photons with energy below $E_g$ cannot bridge the bandgap and therefore produce no photocarriers; this defines the intrinsic cutoff wavelength of the detector.

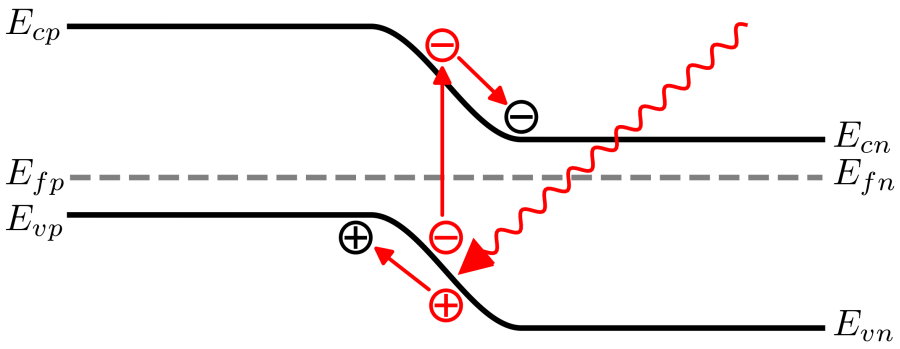


Figure 2.6: The figure illustrates the photogeneration process in a p-n junction. An incident photon with energy greater than the bandgap is absorbed and excites an electron from the valence band to the conduction band, thereby creating an electron–hole pair. The built-in electric field then sweeps the electron toward the n-side and the hole toward the p-side.

The built-in electric field, directed from the n-type cathode to the p-type anode, separates the photogenerated carriers. The electron drifts toward the cathode and accumulates there, while the hole drifts toward the anode (Figure 2.6) [36]. As electrons collect on the cathode, the effective reverse bias across the junction decreases and the depletion region contracts. Figure 2.7 shows a diagram of the pixel, demonstrating the structure of the pixel and how the depletion region contracts as charge is integrated. This phenomenon, often termed debiasing, gives rise to several secondary effects, including persistence. Persistence occurs due to the dynamic size of the depletion region. Traps are filled during illumination, when charge is collected and the traps are immersed in the collected charge. These traps are emptied when the pixel

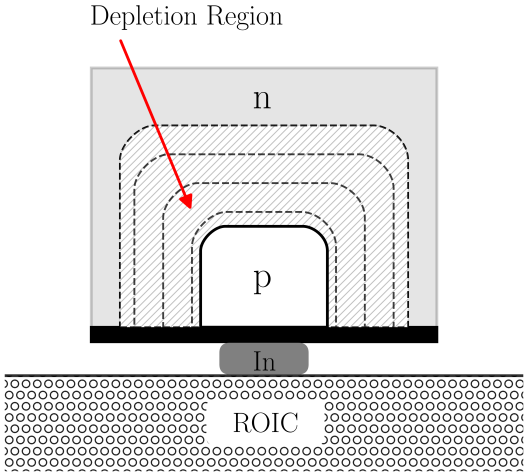


Figure 2.7: This figure shows a simple diagram of the pixel structure. The n-type and p-type regions are labeled, as are the indium bump and ROIC. The frontside surface passivation is depicted as a black rectangle. The depletion region contracts from its maximum size (determined when the pixel is reset) down to the p-implant as charge is integrated and the pixel approaches saturation.

reset removes surrounding collected charge, allowing the traps to eject the captured charge back into the depletion region. The timescales for this trapping and release are varied, which is discussed in more detail in Section 3.3.

At the end of the integration period, the pixel is selected, the accumulated charge is measured through the resulting voltage change across the junction, and the signal is digitized and stored. The photodiode is then reset to its original reverse-bias voltage, clearing the collected charge and preparing the pixel for the next integration cycle.

### 2.1.4 Defective Pixels

Defective pixels generally fit into two categories, those that are "dead" and those that are "hot" or "warm." A dead pixel is one that does not integrate charge or respond to stimulation from light or the ROIC. This can occur due to defects in the pixel itself or defects within the ROIC - disconnected indium bumps, defective ROIC implants, and internal shorts. Hot pixels are overly electrically active and exhibit abnormally high signal. Hot pixels are always at the maximum possible signal, while others are "warm," and exhibit abnormally high signal gain or dark current. These are often caused by material defects which can warp the energy band structure of pixel or introduce mid-gap traps to facilitate tunneling across the bands [8, 14, 13, 4].

## 2.2 Dark Current

Dark current refers to the collective current generated in a photodiode in the absence of illumination. The primary mechanisms responsible for dark current in HgCdTe detectors are thermal generation of carriers within the depleted region and tunneling across the narrow bandgap. In state-of-the-art infrared and visible detectors, dark current can be extremely low, on the order of $10^{-5}$ e/pixel/s [37]. For certain long-wavelength applications, however, significantly higher values are tolerated; the HgCdTe GeoSnap detectors, for example, exhibit dark currents above $10^{5}$ e/pixel/s [38]. This section presents models for the dominant dark current mechanisms, which are compared with the measurements obtained for V23 in Section 3.4.

### 2.2.1 Diffusion

Diffusion current arises from thermally generated carriers that reach the edge of the depletion region and are subsequently swept across the junction by the built-in electric field. In the neutral p-type region, a small fraction of the electrons generated within one diffusion length of the depletion-region boundary diffuse to the junction and are injected into the n-side. Similarly, holes generated within one diffusion length of the junction in the neutral n-type region diffuse to the depletion-region edge and are injected into the p-side [39, 22, 26, 40]. Diffusion current is given in Equation 2.1.11, and can be expanded to this form in units of $e^-/s/\text{pix}$:

$$J_{\text{diff}} = \frac{A{n_i}^2 d}{N_d \tau_b} \left( e^{\frac{qV_{\text{actual}}}{k_b T}} - 1 \right) \tag{2.2.16}$$

where $A$ is the area of the p-n junction in in $\text{cm}^2$, $d$ is the thickness of the absorber region in cm, $N_d$ is the donor ion dopant concentration in $\text{cm}^{-3}$, $\tau_b$ is the minority carrier lifetime in seconds, $q = 1.6 \times 10^{-19}$ is the elementary charge in coulombs, $V_{\text{actual}}$ is total potential across the junction at any point in time, $k_b = 1.38 \times 10^{-23}$ J/K is the Boltzmann constant, $T$ is the temperature in Kelvin, and $n_i$ is the intrinsic carrier concentration in $\text{cm}^{-3}$ given by Equation 2.1.9. For the SATIN detectors, which are strongly reverse biased (1 V for nominal operation) diffusion is only expected to contribute at very high temperatures, dominating other sources of dark current above 120K.

### 2.2.2 Generation-Recombination

The generation-recombination component of dark current (in units of $e^-/s/\text{pix}$) is given by [41]:

$$I_{\text{G-R}} = \frac{qAn_iW}{\tau_{GR}} \frac{\sinh\left(\frac{-qV_{\text{actual}}}{2k_bT}\right)}{\frac{q(V_0 - V_{\text{actual}})}{2k_bT}} f(b) \tag{2.2.17}$$

where $f(b)$ and $b$ are given by

$$f(b) = \int_{z_1}^{z_2} \frac{dz}{z^2 + 2bz + 1} \tag{2.2.18}$$

$$b = e^{\frac{-qV_{\text{actual}}}{2k_bT}} \cosh\left(\frac{E_i - E_{\text{trap}}}{k_bT}\right) \tag{2.2.19}$$

and $z_{1,2}$ are:

$$z_{1,2} = \left(\frac{\tau_{p0}}{\tau_{n0}}\right)^{1/2} e^{\mp\left(\frac{q(V_0 - V_{\text{actual}})}{2k_bT}\right)} \tag{2.2.20}$$

where $q = 1.6 \times 10^{-19}$ is the elementary charge in coulombs, $A$ is the area of the p-n junction in in cm$^2$, $\tau_{GR}$ is the carrier lifetime in seconds, $V_{\text{actual}}$ is the bias applied to the detector in volts, $V_0$ is the intrinsic bias of the junction, $k_b$ is the Boltzmann constant, $T$ is the temperature in Kelvin, and $n_i$ is the intrinsic carrier concentration in cm$^{-3}$ given by Equation 2.1.9 [18].

Treatments of this model in the literature (Bacon [39], Cabrera [42]) extend the integration limits of $f(b)$ to be from 0 to $\infty$, which can be done when the applied bias is several $kT/q$ less than the intrinsic bias of the junction, as is the case for Teledyne devices treated in those theses [41]. However, as the SATIN devices are meant to operate at much higher applied biases this simplification does not apply. Moreover, as the regime of interest for the SATIN detectors is at low temperatures, we find that the G-R current at high temperatures is adequately modeled by the simplest form of the G-R function [24]:

$$I_{\text{G-R}} = \frac{qAn_iW}{\tau_{GR}} \tag{2.2.21}$$

### 2.2.3 Tunneling

Quantum-mechanical tunneling contributes to dark current through two principal mechanisms: direct band-to-band tunneling (BTBT), in which electrons tunnel from the valence band to the conduction band, and trap-assisted tunneling (TAT), in which electrons tunnel via mid-gap trap states. The band-to-band tunneling current (in e/s/pixel) is given by [25, 43]:

$$I_{bb} = -\frac{q^2AEV_{\text{actual}}}{4\pi^3\hbar^2}\sqrt{\frac{2m_{eff}}{E_g}} \exp\left(-\frac{\pi\sqrt{m_{eff}}{E_g}^{3/2}}{2\sqrt{2}q\hbar E}\right) \tag{2.2.22}$$

where $E_g$ is the bandgap energy, $m_{eff}$ is the effective mass of an electron, and $E$ is the electric field across the depletion region given by:

$$E = \sqrt{\frac{2N_d(E_g - qV_{\text{actual}})}{\epsilon\epsilon_0}} \tag{2.2.23}$$

$I_{bb}$ also encodes Zener breakdown, which is an increase in current resulting from a narrowing of the gap between the conduction and valence bands as the applied voltage increases. Since the potential difference between the conduction and valence bands of their respective regions is proportional to $V_0 - V_r$ and depletion width scales with the square root of this relation (Equation 2.1.10), the gap between the bands narrows more quickly and increases the probability of tunneling across the potential barrier (Figure 2.8).

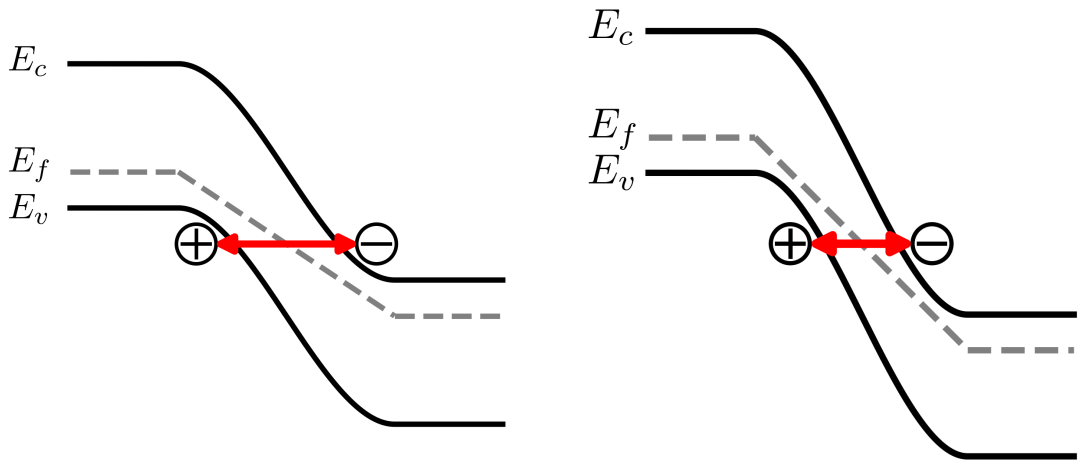


Figure 2.8: This figure compares band diagrams of a p-n junction under two different reverse-bias conditions. The left diagram corresponds to low reverse bias, while the right diagram corresponds to high reverse bias. The increased reverse bias reduces the effective tunneling distance across the gap and increases the probability of band-to-band tunneling.

In the trap assisted case,

$$I_{tb} = \frac{q^2 m_{eff} n_t A V_{\text{actual}} M^2}{8\pi\hbar^3(E_g - E_t)} \exp\left(-\frac{4\sqrt{m_{eff}}E_g^{3/2}}{2\sqrt{2}qE\hbar}G(a)\right) \tag{2.2.24}$$

where $E_t$ is the trap energy relative to the valence band, and $n_t$ is the density of traps with

that energy. $M^2 \approxeq 10^{-23}$ eV$^2$cm$^3$ is the mass matrix associated with the trap potential [42, 24] $G(a)$ is a geometric factor:

$$G(a) = \frac{\pi}{2} - a(1 - a^2) - \text{asin}(a) \tag{2.2.25}$$

where $a$ is a factor representing the trap location within the bandgap energy:

$$a = 2\frac{E_t}{E_g} - 1 \tag{2.2.26}$$

In V23, which has a high defect density $n_t$, $I_{tb}$ dominates over $I_{bb}$ by several orders of magnitude, despite the high reverse bias.

### 2.2.4 Surface Currents

The SATIN detectors are novel in part due to the growth method used to create them, which starts with a silicon wafer, buffer layers, and finally the HgCdTe material. The large lattice mismatch between the silicon and the buffer layers causes threading dislocations which propagate through the buffer layers and extend into the HgCdTe. After growth, most of the buffer material is removed by selective etching, a step that—together with the presence of threading dislocations—produces surface defects that require passivation. Imperfect passivation results in surface currents, which can contribute significantly to the overall dark current. Following the work of Bacon [39], we model the surface currents as:

$$I_s = \frac{qAn_{is}s}{2} \tag{2.2.27}$$

where $s$ is given by:

$$s = s_0\frac{W_d}{\tau_s}\left[\exp\left(\frac{qV}{\beta k_b T} - 1\right)\right] \tag{2.2.28}$$

where $s_0$ is a unitless velocity coefficient, $\tau_s$ is the lifetime of the surface states, $W_d$ is the width of the depletion region, $T$ is the temperature, $q$ is the elementary charge, $V$ is bias across the junction, and $k_b$ is the Boltzmann constant. $\beta$ is an ideality factor, and is also used to modify

the usual $n_i$ to $n_{is}$:

$$n_{is} = (5.585 - 3.820x + 1.753 \times 10^{-3}xT) \left[10^{14} {E_g}^{3/4} T^{3/2} \exp\left(-\frac{E_g}{\beta k_b T}\right)\right] \tag{2.2.29}$$

$\beta$ is not the only variable that can be modified to affect the behavior of $I_s$, it is also possible to adjust the composition fraction $x$ to affect it as well. Since the function describes the behavior of currents generated at the surface, it is probable that the material composition varies due to processing effects and the growth method. In the case of the V23, we find that $\beta = 3$ with an unmodified $x$ is sufficient to support the findings in the data.

### 2.2.5 Rule-22

Analytical evaluation of the dark current equations presented above is challenging and rarely yields results that fully capture the observed device behaviour. Consequently, most published studies of dark current performance rely on parameterised fits rather than detailed physically based models. This situation is further complicated by the fact that detector manufacturers typically do not disclose the detailed doping profiles within the pixels, information that would be essential for rigorous modelling. Nevertheless, extensive characterisation efforts, particularly those performed on Teledyne HgCdTe detectors, have produced a large and reliable dataset of dark current measurements across a wide range of material and processing conditions.

"Rule-07", and later, "Rule-22", were defined as heuristic models to estimate the performance of a device based on a range of parameters [44, 37]. These are not physical mechanisms - they are a useful comparison tool that model the behavior of the best detectors that Teledyne has produced for infrared imaging. The discussion of Rule-22 here will be used to compare and contrast the performance of V23 to the state-of-the-art in later sections, providing context for the best-case scenario. Rule-07 was created to accurately model the dark current of a pixel when the signal is dominated by the thermal generation of electrons, while Rule-22 is an update to it that extends the heuristic model to lower temperatures, where G-R and tunneling currents dominate. Zandian defines Rule-22 as a sum of functions, which individually model

aspects of dark current generation: $J_{22} = J_1 + J_2 + J_3$. $J_0$ is a prefactor which forms the baseline function and roughly describes the performance of most devices:

$$J_0 = 10^7 \lambda^{-6.2} + 70\lambda^{1.08} \tag{2.2.30}$$

$J_1$ modifies the pre-factor to more accurately model devices which are limited by Auger-1 diffusion currents:

$$J_1 = J_0 \exp\left\{-\frac{1.2896q}{\lambda kT}\right\}. \tag{2.2.31}$$

$J_2$ describes the section of the Rule-22 curve where trap-assisted-tunneling currents are believed to dominate over Auger-1 diffusion for the best of Teledyne devices:

$$J_2 = 2 \times 10^{-10} J_0 \exp\left\{-\frac{0.4836q}{\lambda kT}\right\}. \tag{2.2.32}$$

The final term, $J_3$, describes the regime where dark current is believed to be limited by a poorly understood background flux, a portion of which is attributed to glow from the ROIC electronics:

$$J_3 = 1.5 \times 10^{-21} \lambda^2 T. \tag{2.2.33}$$

Combining these equations yields Rule-22:

$$J_{22} = \left(10^7 \lambda^{-6.2} + 70\lambda^{1.08}\right) \times \left(\exp\left\{-\frac{1.2896q}{\lambda kT}\right\} + 2 \times 10^{-10} \exp\left\{-\frac{0.4836q}{\lambda kT}\right\}\right) + 1.5 \times 10^{-21} \lambda^2 T \tag{2.2.34}$$

$J_3$ is not a model of the intrinsic detector physics, it represents the non-ideal background noise introduced by the relatively minimal glow that is present in state-of-the-art Teledyne devices, which have mitigation architectures for the glow. These primarily take the form of metallization layers between the ROIC and the substrate, which are designed to prevent emission from the readout nodes from reaching the detector bulk. Such layers significantly reduce the amount of radiation that reaches the detector bulk, as the primary throughput locations are only small gaps in the metallization layer that are left bare for the indium bump

bonds [19, 45, 46, 47]. Unfortunately, such layers are not present in the SATIN devices, and as such the pixels are completely exposed to the underlying glow, which contributes significantly to the noise floor. The glow in SATIN devices is significantly worse than the state-of-the-art, and as such will not be fitted well by the $J_3$ term in Rule-22. Despite the fact that Rule-22 significantly underestimates the glow of the SATIN detectors, it provides a helpful point of reference for comparison to the SATIN data.

## 2.3 Theory of Persistence

Persistence, sometimes referred to as latency, is the phenomenon in which charge from a previous illumination continues to appear in subsequent frames or ramps even after the detector has been reset. In extreme cases the effect can persist for many hours or even days. As noted in the introduction, persistence resembles the afterimage observed in the human eye after exposure to a bright source. The effect has been documented since the earliest solid-state imaging arrays and has become a major concern for high-performance infrared detectors, particularly HgCdTe devices, over the past several decades [30, 48, 31, 49].

In an astrophysical context, long-lasting or inconsistent persistence behavior can be a significant issue for sensitive observations required to probe cosmological constants. Imagine slewing a telescope from one faint observing target to another, and incurring a streak of persistence across the detector after briefly slewing past a bright star - this persistence could render particularly challenging observations impossible for hours in the worst cases. This effect also poses an issue for observations of faint objects which have bright foreground stars, especially when dithering is utilized. Consider the effect of a strong persistence on taking a set of dithered images of a bright stellar cluster, where bright stars could present as additional dim stars on future exposures. Inconsistent persistent effects are hard to characterize and remove, adding another degree of complexity. Detector-to-detector variation in persistence poses a particular challenge, as each must be characterized and corrected independently, as is done for the Nancy Grace Roman and Euclid missions [32, 50].

### 2.3.1 The Smith Model

The currently accepted model for persistence in modern HgCdTe detectors was proposed by Roger Smith in 2008 [16, 51]. It attributes the dominant persistence mechanism to charge trapping at defect states within the p-n junction depletion region. During illumination the depletion region contracts, allowing photogenerated carriers to be captured by these traps. When the junction is subsequently reset to its full reverse bias, the depletion region expands again, but a fraction of the trapped carriers remains inside it. These carriers are then released on timescales spanning many orders of magnitude (from minute fractions second to upwards of $10^5$ seconds) and are detected as signal in subsequent readouts. Figure 2.9 illustrates the process schematically. From top to bottom the subfigures show:

- **a**) a p-n junction after sufficient time under reverse bias for all traps to empty (hole traps are denoted by squares, electron traps by circles);
- **b**) the junction after saturation by photogenerated charge (depletion region contracted);
- **c**) the junction immediately after reset (depletion region expanded, with trapped carriers remaining inside it);
- **d**) the gradual release of trapped carriers into the depletion region, where they are registered as apparent photocurrent in subsequent frames.

The schematic representation in Figure 2.9 necessarily simplifies several important aspects of the trapping process. First, hole and electron traps are not confined to the p-type or n-type regions, respectively; both types of trap can exist on either side of the junction. It is therefore possible for an electron–hole pair generated within the depletion region to be captured immediately by nearby traps on the same side before the carriers separate. Upon release these carriers follow the standard drift paths determined by the internal electric field. Second, the trapping and detrapping timescales vary widely from site to site, spanning many orders of magnitude. The quantity of charge ultimately trapped also depends strongly on the duration of the illumination period. Third, the spatial distribution of traps is far from uniform.

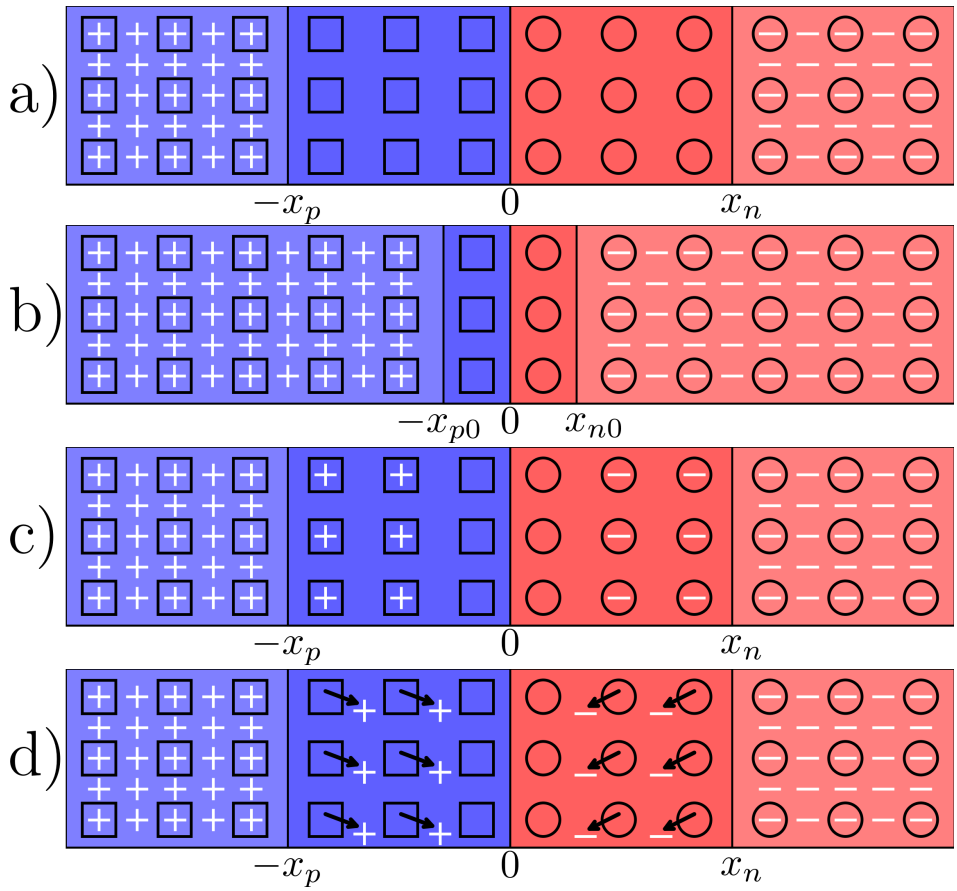


Figure 2.9: A schematic of persistence generation in a photodiode, where charge is trapped in fixed trap sites during charge integration, and released once the diode is reset for the next read.

Trap locations are governed by the underlying defect sources—threading dislocations, lattice impurities, and processing-induced defects—and therefore exhibit a semi-random distribution throughout the absorber volume.

### 2.3.2 Interpretations in the Literature

Many works have assessed persistence in various infrared detectors, sometimes in the context of astrophysical imaging, and often with reference to the Smith model [52, 53, 21, 49, 48, 30, 54]. In most publications the trapping and de-trapping is attributed to Shockley-Read-Hall (SRH) trapping centers, and the observed persistence behavior is attributed to a sum of traps with trapping and de-trapping timescales spanning a few orders of magnitude. There is no comprehensive physical model for persistence that adequately ties the behavior of persistence traps to trap physics, and many heuristic models have been used in the literature [31]. Perhaps the most effective method for modeling the trap populations treats them as a sum of exponential functions [53]. We follow Tulloch and define the amount of charge released in a persistence image $Q(t)$ as:

$$Q(t) = \sum_{n=1}^{n_{max}} N_n \left[1 - exp\left(\frac{-t}{\tau_n}\right)\right] \tag{2.3.35}$$

where $N_n$ is the number of traps with trapping or detrapping time constant $\tau_n$, $n_{max}$ is the number of time constants, and $t$ is the integration time of the exposure measuring persistence. By measuring the amount of charge $Q(t)$ released in a persistence image and adopting a set of reasonable values for the release time constants $\tau_n$, the corresponding trap densities $N_n$ can be determined. The exponential nature of the model reflects the behavior expected of SRH trapping sites, and is consistent with the many studies cited prior. Most of these opt for 2-3 trapping timescales for their models, though these studies acquire data in exposures much shorter than of those presented in this thesis. To account for this, we extend the modeling to use trap lifetimes across five orders of magnitude, which are presented later in Section 3.3. We choose these five orders of magnitude entirely based on the duration span of exposures in our persistence experimentation, as is consistent with the parameters chosen in other studies.

The precise location of the trapping is sparsely discussed, though the literature mostly

supports the Smith model. However, there has been little effort to determine if the trapping primarily occurs at the frontside surface or deeper within the bulk of the detector. An early effort of particular note is the thesis work of Steven Solomon in 1998, who attributed persistence in his InSb arrays to trapping sites within the passivation on the frontside of his detector [55]. By modeling the bandgap structure of his detector, Solomon shows that the most likely candidate for trapping is the $In_2O_3$ oxide created within the $SiO_x$ passivant on the InSb device, as the $In_2O_3$ conduction band falls within the bandgap of InSb. With extensive knowledge of his device properties, he was able to estimate the tunneling probabilities from the valence band of InSb to the conduction band of the $In_2O_3$ oxide, and demonstrate that the traps responsible had to be near the surface.

Unfortunately, a similar analysis for the SATIN devices is not possible due to a lack of detailed device/process information, and there is no clear candidate for the species that could be responsible for the trapping. Although we know that the most likely frontside passivant for this SATIN lot is CdTe, two major issues in narrowing down a responsible species present significant barriers. First, the recent debate on how to correctly calculate the electron affinity ($\chi$) of HgCdTe poses a significant problem this type of analysis [56]. The historic method most commonly cited calculates the electron affinity of MCT (in eV) as follows:

$$\chi_1 = 4.23 - 0.813(E_g - 0.083) \tag{2.3.36}$$

while the newly proposed method suggests that the old method underestimates the actual $\chi$ by approximately 1 eV. The proposed equation for a detector operating at 80 K is:

$$\chi_2 = 5.35 + 0.54x - E_g \tag{2.3.37}$$

where $x$ is the cadmium mole fraction of the MCT. Second, the most common native oxides of MCT that could occur during passivation are amorphous $TeO_2$, $CdTeO_3$, and possibly $HgTeO_3$, and the properties of these materials are not particularly well studied despite the plethora of research on CdTe as a passivant for MCT [8]. While publications exist that discuss

the electron affinities and bandgaps of some of these materials, their properties as trace elements in passivated surfaces are not well understood [57, 58, 59]. Figure 2.10 shows some best estimates for these species alongside CdTe, as well as HgCdTe with both $\chi_1$ and $\chi_2$. All of the numbers are shown in eV, with reference to the vacuum energy by their respective electron affinities. In the case of the $\chi_1$ MCT the only promising species is the CdTe passivant itself, due to the conduction band falling within the bandgap range of MCT. Even so, the errors in these energy levels are on the order of a few hundred meV, and the bandgap of MCT is only my best guess based on the longwave cutoff of the SATIN detectors. The $\chi_2$ MCT does not present a promising candidate species. Ultimately, the uncertainties associated with this type of analysis in this application do not make it a promising avenue for investigating persistence.

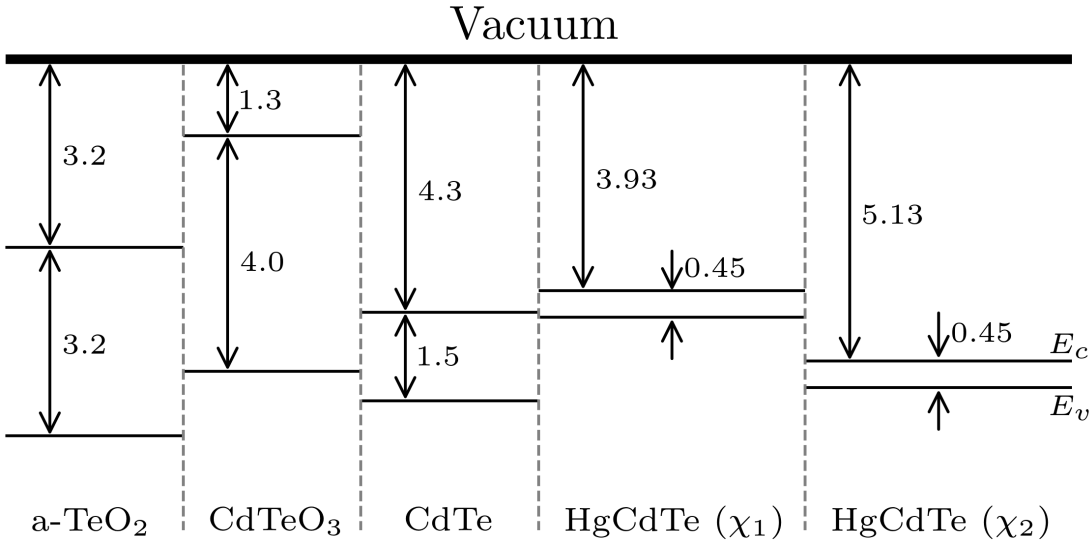


Figure 2.10: The figure shows a bandgap energy diagram for HgCdTe, the CdTe passivant, and two relevant oxides.

# Chapter 3

# Characterization

*Portions of this chapter are based on previously published works:*

**1.** Buntic, Lazar, et al. 2024, *Advancing Large Format MCT/Si Infrared Detectors for Astrophysics Research*, SPIE Proceedings Volume 13103, DOI: 10.1117/12.3019111

**2.** Figer, Donald F., Buntic, Lazar, et al. 2022, *The SATIN Infrared Detector Development Program and the Road to HELLSTAR*, SPIE Proceedings Volume 12191, DOI: 10.1117/12.2627511

## 3.1 Equipment

The testing on the SATIN devices was performed with a suite of systems and tools created for that purpose at the CfD detector laboratory. At the center of the testing apparatus is the cryogenic dewar, a custom-made (by Universal Cryogenics LLC) vacuum chamber built to house the detector and provide means to interface with it, both cryogenically and electronically, while maintaining a high-vacuum environment. The equipment setup and a diagram of the dewar are shown in Figure 3.1. The orange cylinder in the middle is the dewar - to the left is the attached cryogenic apparatus and pressure gauge (Edwards CTI Ltd. 1050 Two-Stage Refrigerator w/ 9600 Helium Compressor and Agilent Technologies Inc. Varian FRG-700, respectively). Above the dewar is a shelf, which supports the custom detector electronics (JMClarke Engineering) and their power supply, while the aluminum structure to the right

supports the monochromator (PI Acton SpectraPro 2500i) and light source (Princeton Instruments TS-428.) Between the monochromator and dewar is an integrating sphere wrapped in blackout curtains. In front of the dewar is a stack of controllers, which power and operate light-sensing diodes that are mounted on the integrating sphere.

The bottom image in Figure 3.1 shows a crosscut diagram of the dewar internals. The detector is in the middle of the dewar, within the detector housing, which provides protection from light leaks and provides feedthroughs for the cryogenic and electronic connections. The detector is thermally coupled to the cold finger by a copper strap. In the system used for our experiments, only the filter wheel closest to the detector was installed; The filters are discussed in more depth in Chapter 4. The light path for the system starts at the light source, passes through the monochromator, integrating sphere, dewar window, and filter wheel before reaching the detector. The ingress slit between the monochromator and light source is mechanical and remotely controlled, allowing for fine control of the amount of light reaching the detector. The array of temperature sensors and heaters within the dewar are monitored and operated by a temperature controller (not pictured, Lake Shore Cryotronics Inc.).

## 3.2 Pixel Masking

In order to properly characterize pixel behavior, we first identify and reject anomalous pixels that would otherwise contaminate the data. Aside from the obvious, *i.e.* dead pixels (those that fail to integrate any charge) and hot pixels (those which are permanently saturated), a number of other behaviors were observed in the V23 data (Figure 3.2.) The two columns of plots were created using different gains, hence the pixels in the second column reaching saturation in earlier frames. Among them are pixels that saturate early, exhibit significant non-linearity at low signal levels, reset to a level higher than the pixel nominally should, or exhibit some combination of those effects. The signal plots in the top row of Figure 3.2 are for pixels that don't reset to the expected level, one of which also exhibits a strong early non-linearity (purple) and one of which saturates early (light pink). The bottom row of plots shows a selection of well behaved (green) and hot pixels (red).

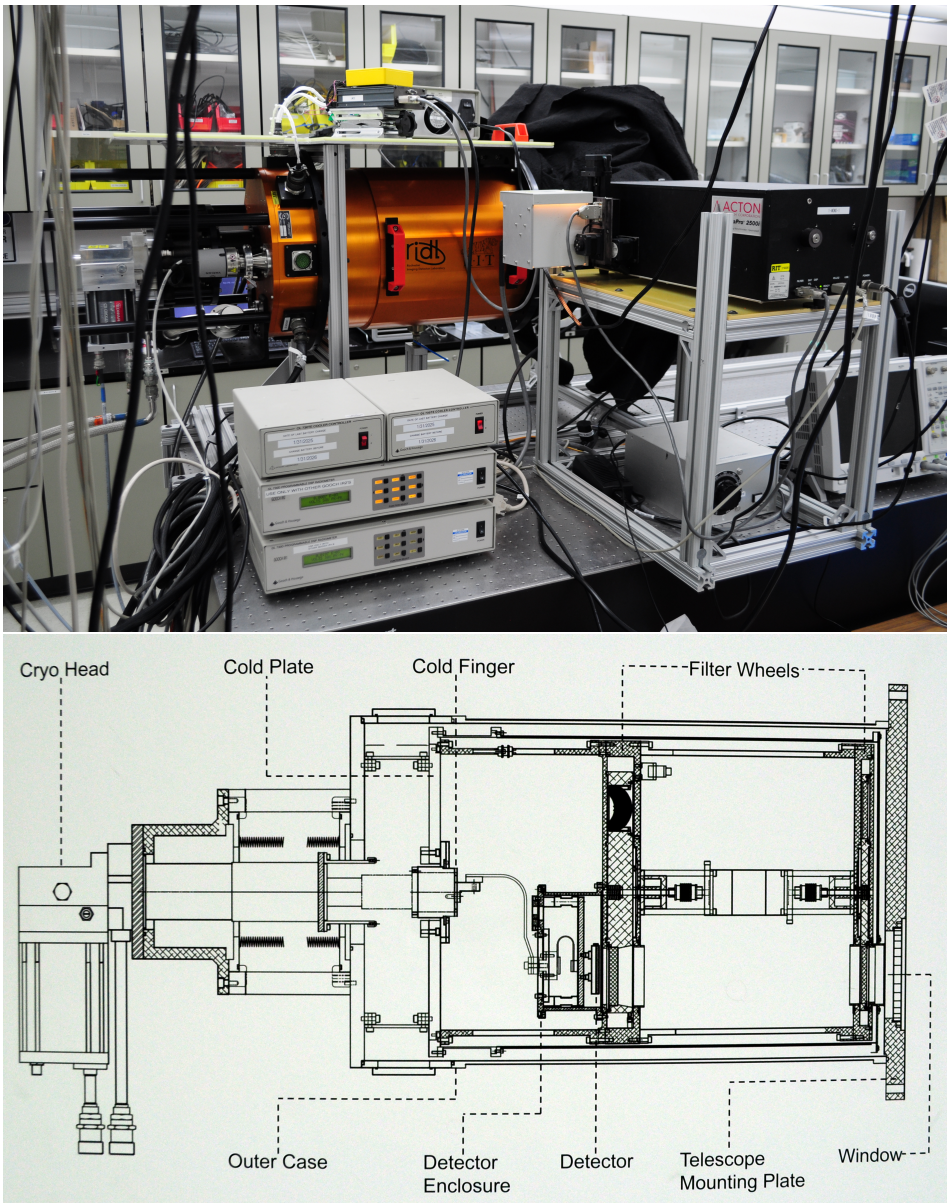


Figure 3.1: This figure shows the equipment setup at the detector laboratory, and a cross-section diagram of the cryogenic dewar.

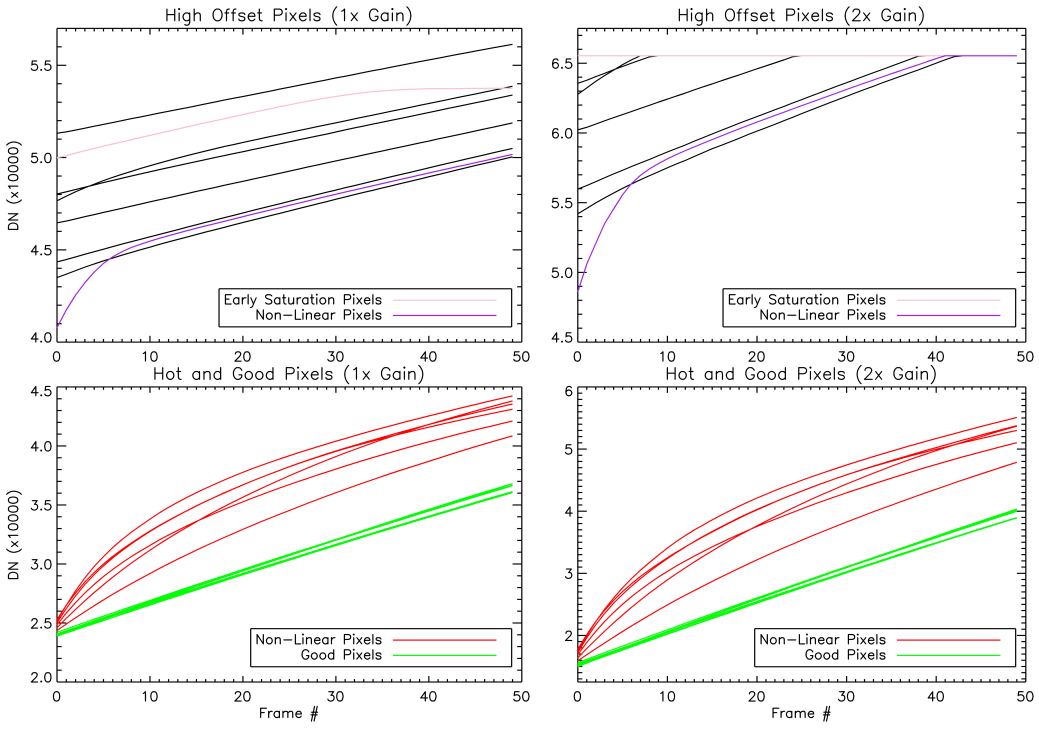


Figure 3.2: These plots show dark current plots for well behaved, linear pixels (green), pixels that exhibit non-linear behavior (red), pixels that start at an abnormally high signal (black), high-offset pixels that saturate earlier than others (pink), and high-offset pixels that exhibit non-linear behavior (purple.) Note the change in electronic gain between columns of plots.

A simple Boolean search for pixels that have signal outside of a certain threshold in the first frame after the detector reset is used to mask high-offset, dead, and saturated pixels. In order to mask out the pixels that exhibit odd and non-linear behavior, we identify linear and non-linear pixels by measuring the concavity of their signals versus time via the second derivative. We calculate the second derivative of the signal up the ramp for each pixel and reject all pixels whose second derivative has a standard deviation above a rejection threshold. Figure 3.3 shows two relevant plots. The first depicts the second derivative of pixel values through the test ramp, showing that the good pixels behave linearly, and thus have a constant second derivative. Pixels that do not have linear behavior produce the curves shown in red. Taking the standard deviation of the second derivative (SDSD) has proven a simple and effective way to find the number of pixels that behave anomalously. The second plot shows the SDSD of pixels in each quadrant, as well as the full array. Note that Q4 has the smallest tail, implying that it has fewest hot/non-linear pixels, which is consistent with our dark current maps. Of the full array, 1.6% of the pixels have an SDSD$\geq$10. In Q4, only 0.8% of pixels have an SDSD$>$10, while nearly 2.6% of pixels in Q1 exceed this limit. Table 3.1 lists the number of pixels rejected for most of the analysis performed in this thesis (mainly dark current) using three base criteria: all pixels with SDSD$\geq$7, all saturated and high-offset pixels, and all neighbors of hot and high-offset pixels. Minor variations in the masking choices made here do not greatly change the conclusions. For example, reducing the strictness of the SDSD threshold from 7 to 10 changes the dark current results, where masking choices are most impactful, by $\leq$5%.

| **Criterion** | **# Rejected** | **% of Q4** |
|---|---|---|
| SDSD$\geq$7 | 23,249 | 8.8% |
| Hot/High Offset | 25,520 | 9.7% |
| Hot Neighbors | 121,483 | 46.3% |

Table 3.1: This table shows rejected pixel counts based on various criteria in Q4 of V23.

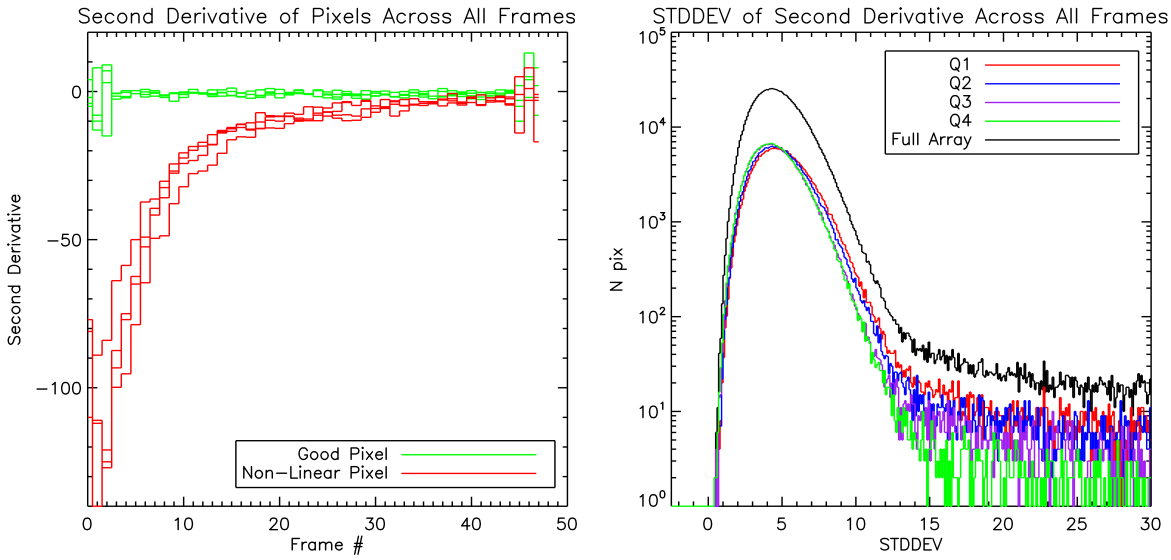


Figure 3.3: This figure presents two plots that show how we calculate the second derivative of the signal through a series of 50 frames for V23. Shown on the left are plots for a few good pixels (green), and hot pixels (red). Shown on the right are the standard deviations of pixel values in each quadrant; Note that the tail for Q4 is lower than the other quadrants.

## 3.3 Persistence

The goal of persistence testing the SATIN devices is threefold. First, we test the Smith model of persistence by using two unique testing methods to confirm that the trapping happens primarily in the active region of the detector. Second, we attempt to distinguish between trapping that occurs at either detector surface or the internal bulk of the detector material. Third, we want to understand the persistence behavior and the magnitude of the effect in order to compare with current state-of-the-art technology.

### 3.3.1 Experimental Methods for Persistence Testing

Three distinct experimental protocols were developed to characterize persistence in the SATIN detectors and thereby estimate the number of charge traps in each pixel. The first protocol, designated the LEAVEOPEN test, continuously illuminates the detector with strong flux throughout a integration ramp to ensure that all accessible traps become filled. After this "soak" period the detector is reset and a sequence of dark frames is acquired to record the

time-dependent release of trapped charge. Figure 3.4 illustrates the illumination and charge-collection timeline for this mode: the solid black line represents the total integrated signal during illumination, the dashed red line is the incident photon flux, and the solid red line is the latent charge released after reset.

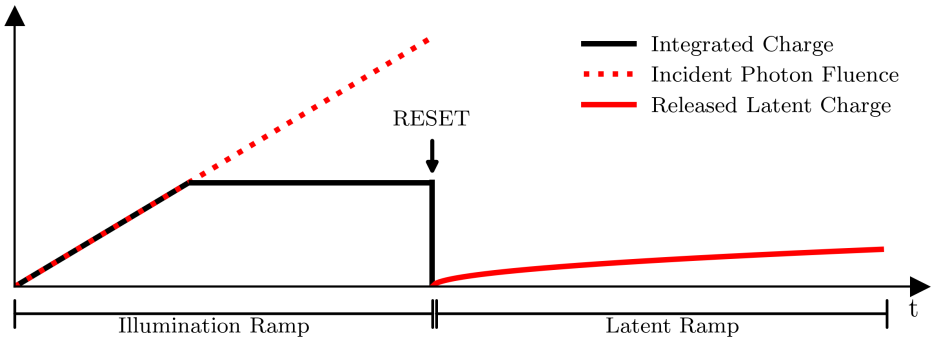


Figure 3.4: The figure illustrates the illumination and readout sequence used in the LEAVEOPEN persistence test protocol. The vertical axis and all features are schematic and not drawn to scale.

The second protocol, denoted "BIASONLY," eliminates optical illumination entirely. Instead, the reverse bias across the photodiode is reduced (or briefly made forward) to collapse the depletion region and allow carriers from the neutral regions to fill traps (see Section 1.4.3 for more information on this process.) In the measurements reported here the diode was forward-biased just sufficiently to eliminate the built-in depletion region. In all three protocols the duration of the period during which charge is available to fill traps is referred to as the soak time.

The third protocol, designated FWD%, operates as follows. The detector is illuminated to a target fraction of full-well capacity within the first 15 s of the ramp. This level is then held constant for a controlled soak duration, after which the detector is reset and the subsequent persistence release ramp is acquired. The required photon flux is determined automatically at the start of each run. The control software iteratively adjusts the monochromator entrance-slit width and acquires short test exposures until the desired signal level is reached within the 15 s window.

The LEAVEOPEN and BIASONLY test modes were designed to serve essentially the same

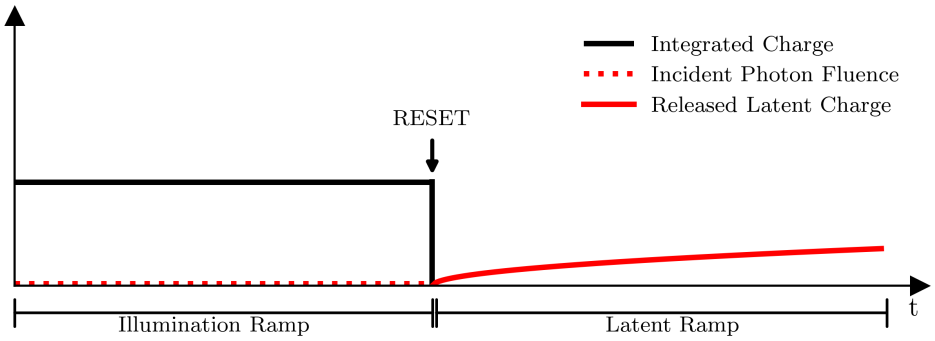


Figure 3.5: The figure illustrates the illumination and readout sequence used in the BIASONLY persistence test protocol. The vertical axis and all features are schematic and not drawn to scale. Note the lack of actual illumination, as all charge integration is achieved by bias manipulation.

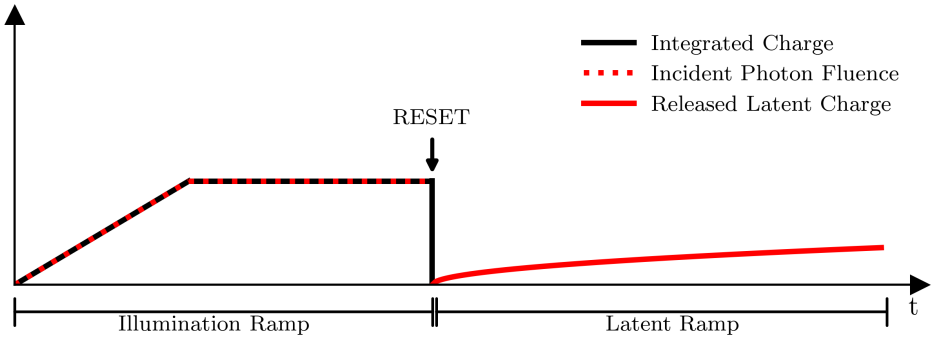


Figure 3.6: The figure illustrates the illumination and readout sequence used in the BIASONLY persistence test protocol. The vertical axis and all features are schematic and not drawn to scale. Note that the light source is shut off when the desired level of illumination is achieved.

purpose: both supply the depletion region with a carrier population greatly exceeding the number of available traps, thereby ensuring near-complete trap filling. One important difference is that the LEAVEOPEN protocol, by generating carriers throughout the entire absorber volume, can populate traps located outside the nominal depletion region (for example, near the backside surface) that the bias-only protocol cannot reach. This distinction is exploited later in the present section to discuss the spatial distribution of the dominant trapping sites within the pixel.

### 3.3.2 Variable-Integration-Time Readout Mode

The variable-integration-time scheme discussed in Section 1.4.3 enables total exposure times exceeding 10,000 s while retaining high temporal resolution during the critical early portion of the ramp—a resolution that would be lost in conventional constant-integration-time (fixed-duration) sampling. With fixed integration time the observer must choose between very few long frames (e.g., ten frames of 1000 s) or many short frames (e.g., 10,000 frames of 1 s); Only the latter preserves early-time resolution, but it exceeds the memory capacity of the IDL 6.3 data-acquisition system used to store the raw frames before conversion to `.fits` format. The variable-integration-time mode therefore provides the necessary combination of long total exposure and fine initial sampling required for accurate fitting to Equation (2.3.35).

### 3.3.3 Persistence in V23

Persistence constitutes a major challenge in the characterization of dark current for the SATIN arrays. The standard dark current measurement protocol begins by fully rotating the filter wheels inside the dewar before closing them, a step that momentarily exposes the detector to infrared emission from the integrating sphere. This brief illumination fills a substantial number of charge traps. The subsequent release of trapped carriers contaminates the dark ramps, producing an elevated signal in the first ramp that decays over successive ramps. For short-duration measurements the persistence signal exceeds the intrinsic dark current significantly, and even experiments extending over tens of hours remain measurably affected

by this contamination.

If the locations of traps were to be concentrated on the backside (illumination) surface of the detector due to passivation issues and surface trapping, we would expect to see a morphological difference in the persistence maps for these two testing modes. As such, the latency data for the LEAVEOPEN and BIASONLY modes were inspected to determine if there were any differences in the persistence maps. Figure 3.7 shows two maps of persistence in Q4: the latent data for the LEAVEOPEN mode on the left, and for the BIASONLY mode on the right. On first inspection, the only notable difference between the two images aside from the cosmic ray impact in the bottom right of the BIASONLY image is a dark spot on the left side of that image. This spot appears in both images and correlates to a physical defect in the detector, but is significantly more pronounced in the bias-manipulated data. It is unclear why only one of these dark spots would be disproportionately affected by the bias manipulation while the others are not, as is evidenced by Figure 3.8. That figure shows a difference image of the two modes on the left and a division of the LEAVEOPEN image by the BIASONLY one on the right. Aside from the defective spot, the difference image shows the same morphology as either dataset, as is expected if all of the trapping is occurring within the bulk of the detector and not near the surface. The ratio image is essentially flat, showing that the persistence in the illuminated image is higher by approximately 10% (10.7% mean, 10.4% median.)

This result conclusively rules out the backside surface of the detector as a source of traps that cause persistence in the detector, as there is no correlation between measured persistence and surface damage on the detector. It also demonstrates that the traps being activated in both tests are the same trap populations, but that the LEAVEOPEN mode is accessing a set of traps that are evenly distributed and not accessible to the BIASONLY mode. This means that the vast majority of the trapping is happening within the active region of the detector, and quite possibly near the passivated frontside surface of the detector, which is always a part of the depletion region (see Figure 2.7).

Figures 3.9 and 3.10 present persistence decay curves measured in well-behaved pixels of Q4 using the LEAVEOPEN and BIASONLY exposure modes, respectively. In each figure the upper

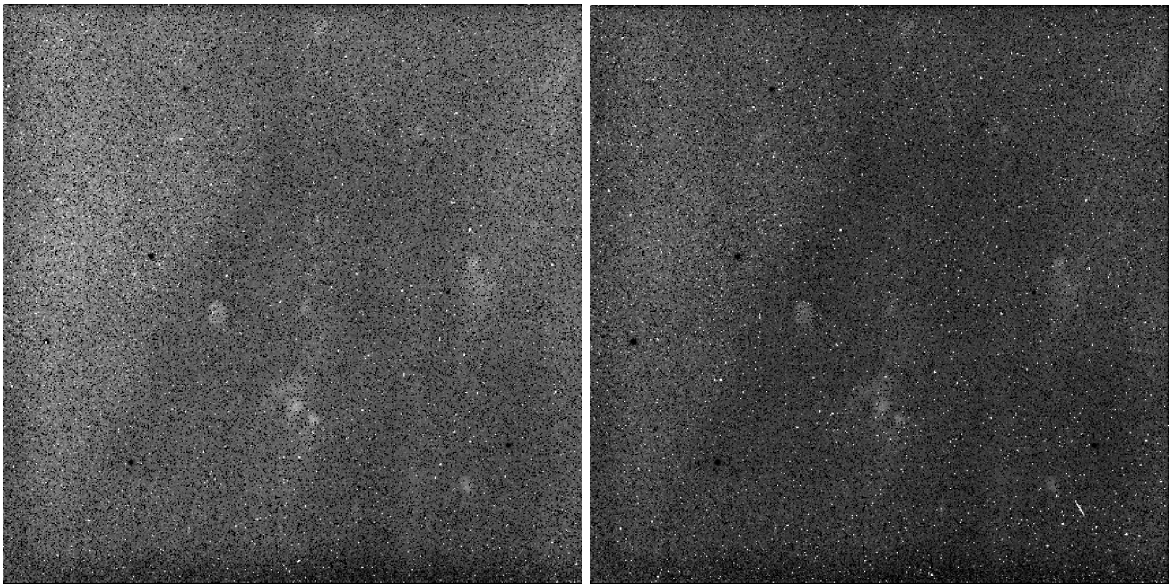

Figure 3.7: This figure shows two maps of persistence for Q4 of V23. On the left is persistence from the LEAVEOPEN test mode, on the right is persistence from the BIASONLY test mode.

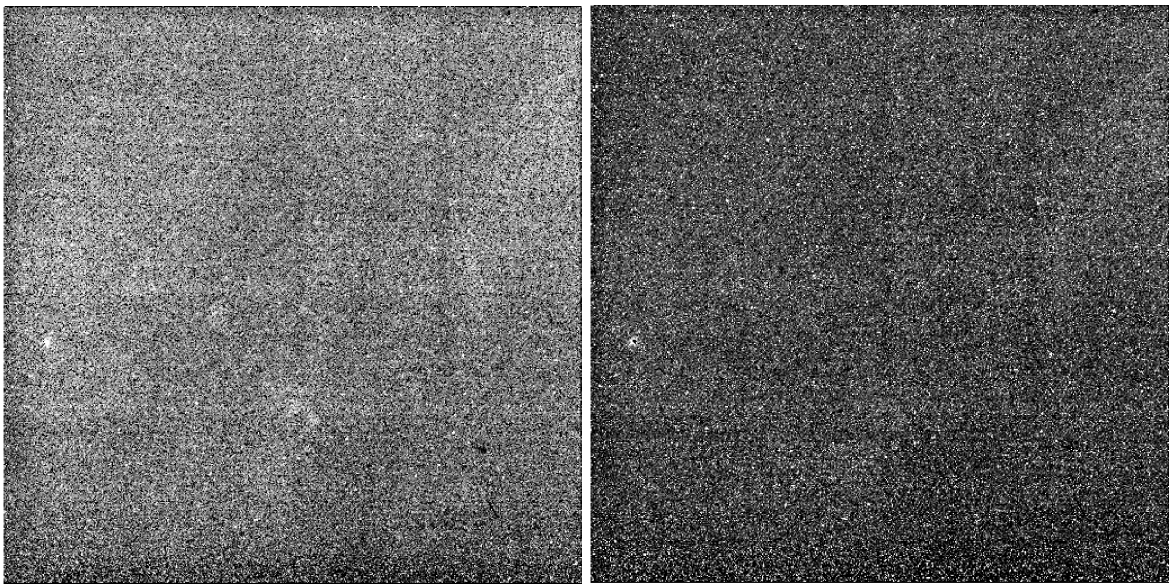

Figure 3.8: This figure shows two maps of persistence for Q4 of V23. On the left is a difference image made by subtracting the BIASONLY persistence from the LEAVEOPEN persistence. On the right is a map made by dividing the LEAVEOPEN data by that from the BIASONLY data.

panel displays the individual exponential components obtained from fitting Equation (2.3.35) together with their sum, while the lower panel shows the cumulative released charge as a function of time. The cumulative trace in the lower panel includes the contribution from the labeled time constant and all shorter time constants.

Table 3.2 lists the number of traps $N_n$ derived for each time constant in both exposure modes. Previous studies of comparable detectors indicate that trap populations associated with different time constants are typically of similar magnitude [52, 53]. The noticeably lower $N$ obtained for $\tau = 1\,\mathrm{s}$ is therefore likely an artifact of the measurement procedure: the first 1-second frame is subtracted from itself and all subsequent frames to remove reset-level variability, which necessarily discards a fraction of the charge released on the shortest timescale. A complementary excess in the longest time-constant bin is likewise attributed to a small population of traps with release times exceeding the $10^4\,\mathrm{s}$ duration of the present measurements.

The total charge released in the LEAVEOPEN protocol exceeds that measured in the BIASONLY protocol by approximately 12%. This excess demonstrates that optical illumination likely populates traps located outside the nominal depletion region—regions that remain inaccessible when charge is introduced solely by bias manipulation. Carriers released from these extra-depletion traps subsequently diffuse via random walk until they enter the depletion region, where the built-in field sweeps them to the collection junction and registers them as apparent photogenerated signal in later readouts.

| | **LEAVEOPEN** | **BIASONLY** |
|---|---|---|
| $\tau$ | $N_i$ | $N_i$ |
| 1 | 269 | 212 |
| 10 | 588 | 484 |
| 100 | 523 | 465 |
| 1000 | 432 | 470 |
| 10000 | 617 | 532 |
| **Sum:** | 2429 | 2163 |

Table 3.2: This table shows fitting parameters for the chosen $\tau$ values to the released latent charge after the flooded and bias-manipulated exposure modes.

Figure 3.11 shows the increase in persistence signal as a function of pseudo-forward-bias

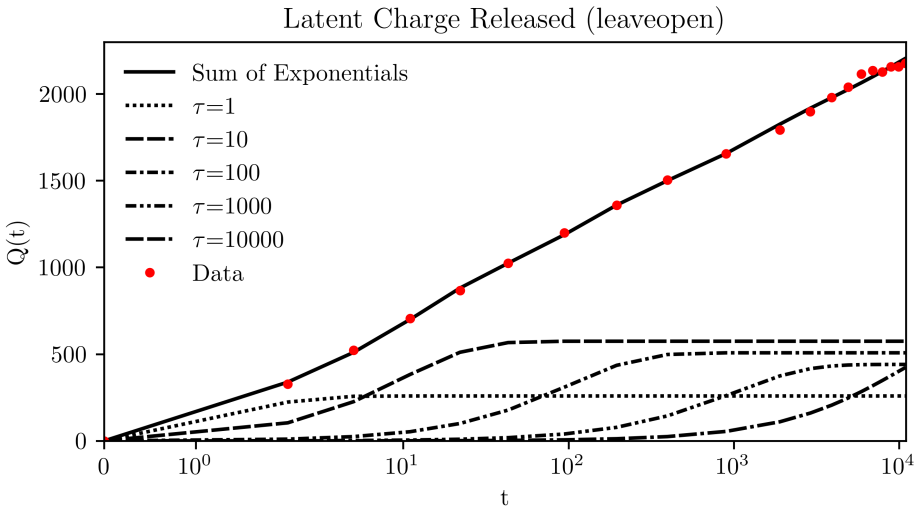


(a) This plot shows each of the fitted time constant functions (Equation 2.3.35) for the data acquired via the LEAVEOPEN read mode, as well as their sum, shown as a solid black line.

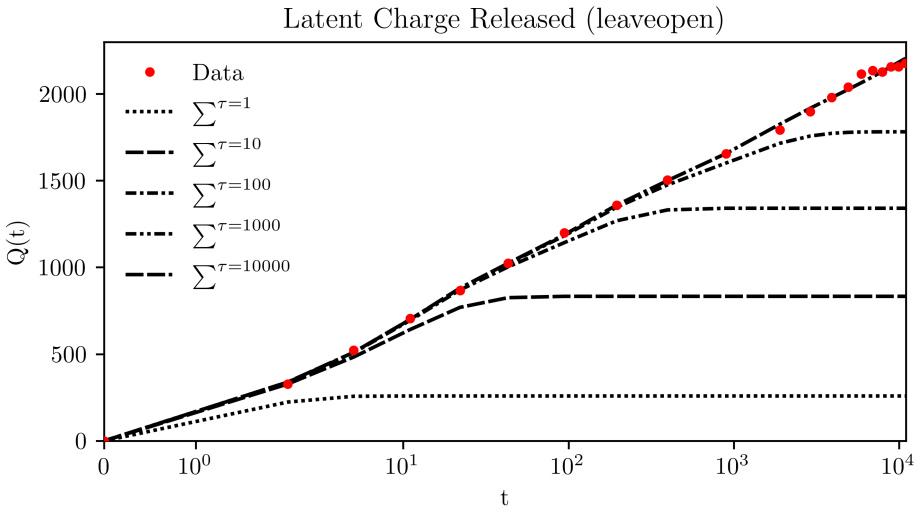


(b) This plot shows the cumulative sums of the fitted time constant functions (Equation 2.3.35) for the data acquired via the LEAVEOPEN read mode.

Figure 3.9

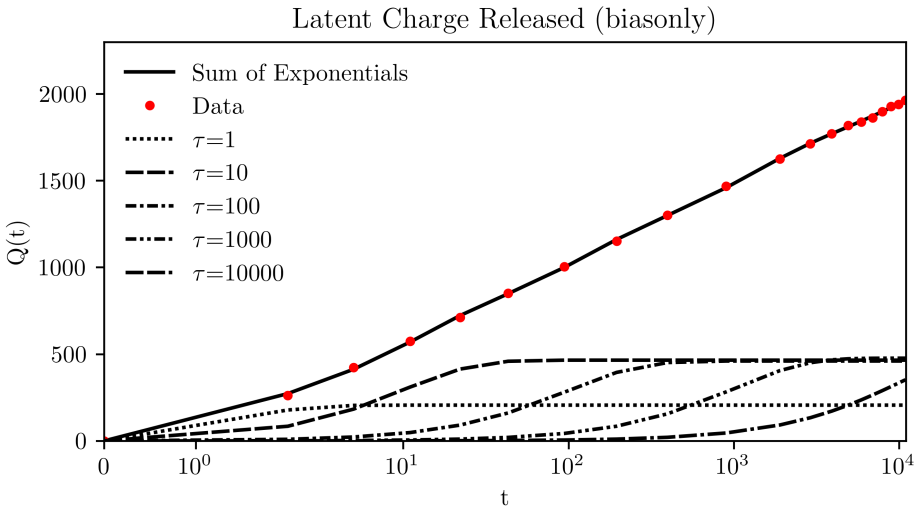


(a) This plot shows each of the fitted time constant functions (Equation 2.3.35) for the data acquired via the BIASONLY read mode, as well as their sum, shown as a solid black line.

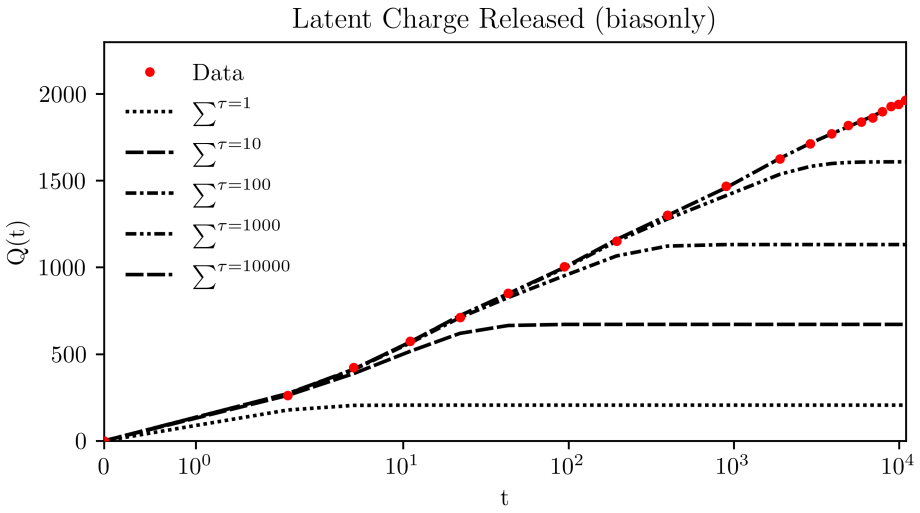


(b) This plot shows the cumulative sums of the fitted time constant functions (Equation 2.3.35) for the data acquired via the BIASONLY read mode.

Figure 3.10

magnitude during the charge-soak phase. The left panel corresponds to a 100 s soak time; the right panel corresponds to a 1000 s soak time. In each panel multiple latent-charge release curves are plotted, with each curve labeled by the value of the reset-gate voltage VRSTUC applied during the preceding soak ramp.

As discussed in Section 1.4.3, under nominal operating conditions the detector is reverse-biased by 1 V ($V_r = -1$ V), achieved by setting VRSTUC = 0.002 V and VDETCOM = 1.002 V. Positive values of VRSTUC shown in Figure 3.11 therefore reduce the applied reverse bias during the soak period. After the soak ramp the detector is returned to its standard reset parameters, allowing previously filled traps to release their charge, which is subsequently recorded as persistence signal in the following readout sequence.

A direct comparison with persistence measurements reported for the state-of-the-art H4RG-10 detectors developed for the Nancy Grace Roman Space Telescope is instructive [31]. Although the test protocols differ, the Roman data provide a useful benchmark. In those measurements the detector was illuminated for 100 s at the end of a 600 s ramp, allowed to soak charge for a 60 s period, reset, and the released latent charge was quantified between 150 s and 300 s of the subsequent dark ramp. The median persistence signal reported with this protocol is approximately 20 electrons (0.02% of the ≈100,000 electron full well depth).

The uppermost curve in the left panel of Figure 3.11 yields approximately 95 electrons of released charge over the same 150–300 s interval. This value is nearly five times higher than the Roman result. However, that difference surprisingly small given the larger V23 pixel volume (20 $\mu$m versus 10 $\mu$m pitch), longer effective soak time, substantially higher defect density in the MCT-on-Si substrate, and full-well capacity at least four times larger than that of the H4RG-10 detectors. If threading dislocation density were the dominant source of persistence traps, a considerably larger increase would be anticipated. The comparison therefore suggests that bulk material defects are not the sole driver of persistence in these arrays. This supports the notion that material defects due to threading dislocations are not the primary source of persistence traps. Recalling the pixel geometry shown in Figure 2.7 and knowing that the threading dislocations begin at the backside surface (top) of the detector, it is likely that

many terminate before reaching the active pixel area, or serve primarily as charge-generation sites, not trapping ones. Definitive conclusions, however, require more detailed comparative measurements and knowledge of the H4RG-10 junction implant geometry.

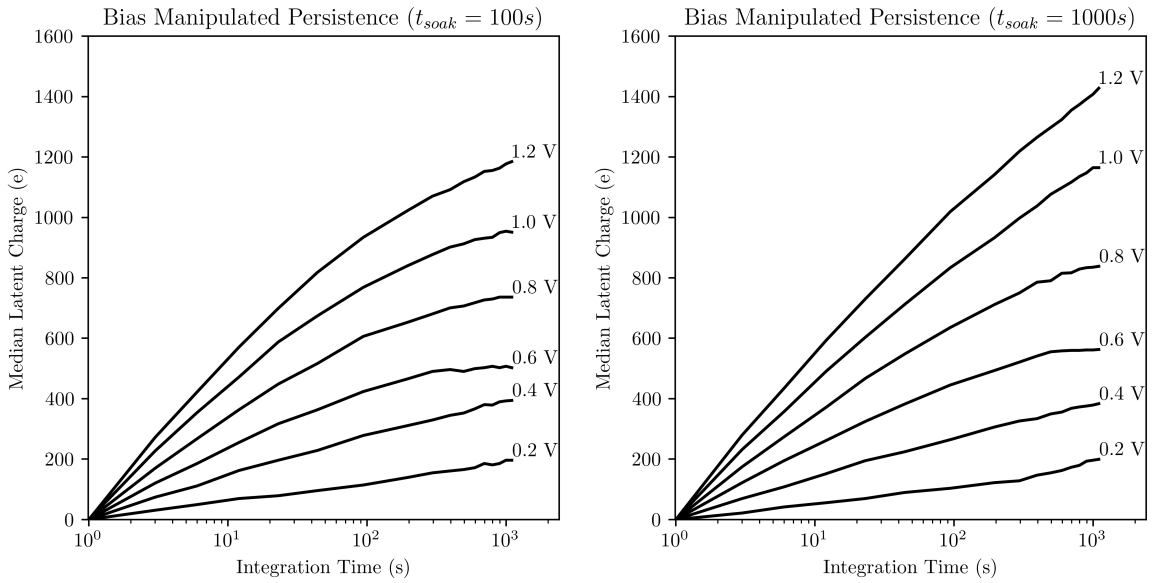


Figure 3.11: This figure shows two plots of BIASONLY persistence for Q4 of V23 across a large range of reverse biases, for soak times of 100 s and 1000 s respectively.

Figure 3.12 presents persistence release curves obtained using the FWD% test protocol with a fixed 1000 s soak time. Each curve corresponds to a different initial fill level of the pixel well, expressed as a percentage of full-well capacity and indicated by the label. After the illumination/soak phase the detector is reset (to nominal reverse bias), and the subsequent latent-charge release ramp is recorded.

Table 3.3 summarizes the persistence measurements presented in Figure 3.12. The three rows list, respectively: (1) the illumination level expressed as a percentage of full-well capacity for the soak ramp, (2) the total number of electrons released during the subsequent persistence ramp, and (3) the released charge expressed as a percentage of the maximum observed value (1361 electrons, obtained at 100% illumination). The near-identical growth rates of rows 1 and 3 demonstrate that the total number of filled traps scales linearly with incident fluence.

Figure 3.13 shows vertical cross-sections through the persistence images of Figure 3.11 at

selected times after reset. These profiles confirm that the magnitude of the released latent charge increases linearly with the total fluence delivered during the preceding illumination/soak phase. Taken together, the data in Table 3.3 and Figure 3.13 establish that trap occupancy in the SATIN detectors rises linearly with integrated illumination over the range examined. This supports the notion that the traps are not clustered, but are evenly distributed within the depletion region, or along the passivated frontside surface. This is contrary to the evidence published by Anderson and Regan, who found that trap density increased in a small layer within the depletion region by performing a bias manipulation experiment [60]. Such an increase would manifest as a step-up in Figure 3.13 - which is clearly not present - though admittedly the data shown here is taken in significantly coarser voltage steps. The errors on the figures in Table 3.3 are on the order of a few percent, and we find them to demonstrate excellent agreement. It is not clear why the data features a consistent droop at high integration times after the 0.6 V soaking ramps, or why there's an inverse effect for the 0.2 V data.

| % of FWD | 19 | 37 | 54 | 64 | 77 | 86 | 93 | 100 |
|---|---|---|---|---|---|---|---|---|
| total released charge (e) | 249 | 464 | 702 | 853 | 1039 | 1164 | 1265 | 1361 |
| % of total released charge | 18 | 34 | 52 | 63 | 76 | 86 | 93 | 100 |

Table 3.3: This table shows the amount of trapped charge released as a function of the percentage of the full well depth to which the detector was illuminated, and as a percentage of the total charge released in the most illuminated ramp.

### 3.3.4 Conclusions on Persistence

The results presented here allow us to make a few definitive conclusions. First, the complete lack of morphological correlation of persistence to the backside surface damage on the detector implies that little-to-none of the trapping is occurring at or near it. Second, the linear growth in trapped charge with total fluence leads us to conclude that the traps are evenly distributed in the active region of the pixel, or at least evenly distributed along the passivated frontside surface. Third, there is an evenly distributed excess charge ($\approx$ 10%) found in saturated images taken with true illumination as compared to bias-manipulated ones. From this we infer that the trap population is strongly dominated by traps near the frontside surface, where the

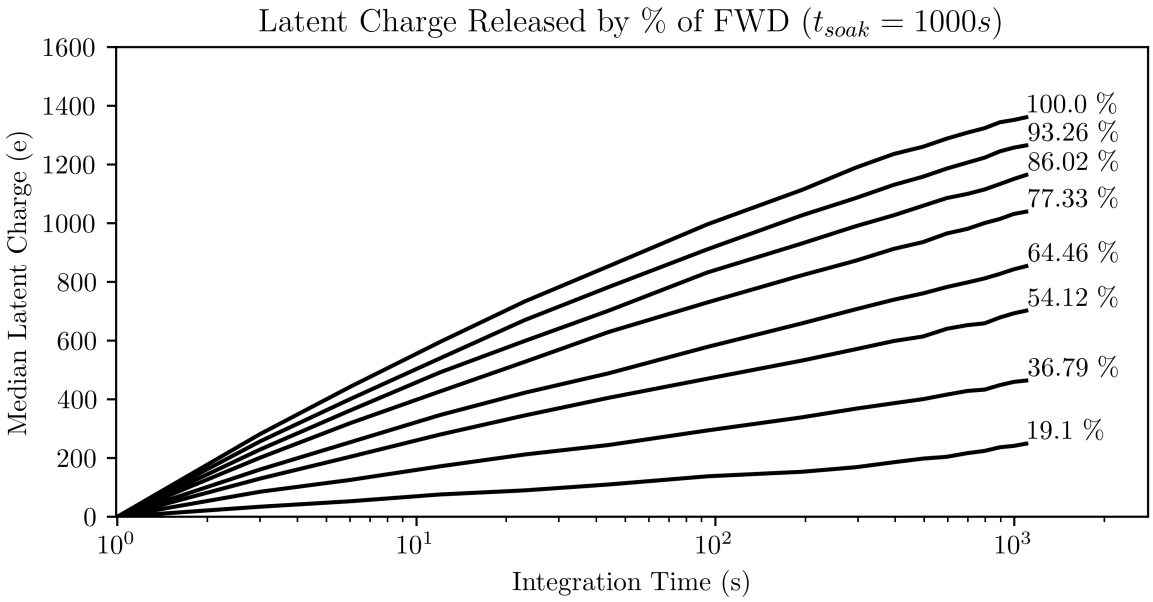


Figure 3.12: This figure shows a plot of persistence for Q4 of V23, taken after illuminating the detector a certain percentage of the full well depth.

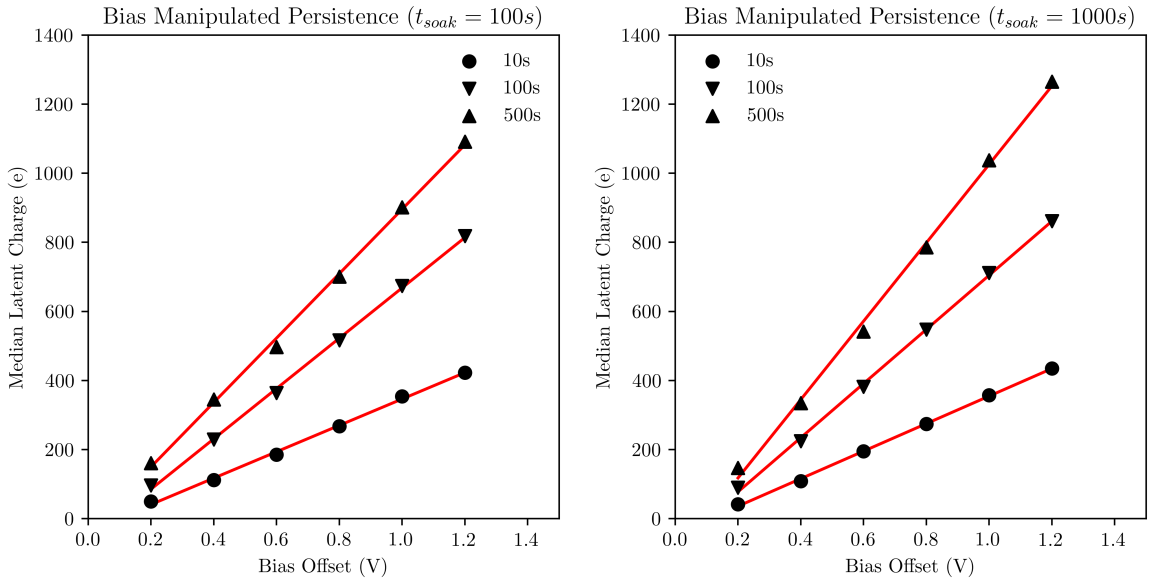


Figure 3.13: This figure shows cross-cuts of the persistence in Figure 3.11 at 10, 100, and 500 seconds.

morphology can be explained by imperfect passivation or mutation of the passivated surface by the epoxy that was wicked between the indium bumps to improve the structural integrity of the detector. The portion of the persistence that shows no significant morphology, *i.e.* the $\approx 10\%$ excess, is from trapping sites that are evenly distributed throughout the detector material. Some portion of these trapping locations exist outside the reach of the bias-manipulation, which accounts for the excess. It is worth noting, however, that this conclusion only stands if the morphology of the persistence images is indeed an effect of surface manipulation by passivation or wicking. The idea that it could be a result of such effects is supported by Ives, who posited that the presence of an epoxy void correlated with persistence behavior in his H4RG detector [49].

The comparison to persistence found in the Nancy Grace Roman detectors is promising, and demonstrates that the persistence performance is approaching the state-of-the-art, though direct comparison is difficult. If the passivated frontside surface is indeed the primary source of persistence trapping, passivation and gradient sculpting methods adopted in the decade since the SATIN detectors were manufactured are sure to reduce the persistence further [8].

## 3.4 Dark Current and Glow in V23

Accurate characterization and modeling of the dark current in V23 have been complicated by the absence of detailed doping concentrations and profiles from the manufacturer. The results of the measurements and the corresponding physical models are presented in this section.

### 3.4.1 Pixels Used in Dark Current Analysis

The pixels selected for the dark current analysis were chosen using objective performance criteria, specifically their isolation from hot pixels and the linearity of their response. Two independent masks were constructed and combined to exclude poorly performing pixels. The first mask eliminates all pixels that are either persistently hot or neighbor hot pixels. The second mask, derived from photon transfer measurements, excludes pixels exhibiting non-linear or anomalously rapid charge accumulation (see Section 3.2). Convolution of the masks

therefore rejects all pixels that are hot, neighbor hot pixels, or have SDSD>7. Application of the combined mask removes approximately 150,000 pixels from Q4, which contains 262,144 pixels in total. Because of the glow artifact present in the lower portion of the array (discussed below), only pixels in the top 50 rows of Q4 were retained. The final sample therefore consists of approximately 13,000 well-behaved pixels that display consistent and acceptable dark current characteristics.

Construction of the pixel masks revealed a clear correlation between defective-pixel fraction and junction implant area. Figure 3.14 presents two ratios for each of the four quadrants: the fraction of hot pixels $N_h/N_q$ (black) and the ratio of implanted junction area to total pixel area $A_{\text{junc}}/A_{\text{pix}}$ (red). The nearly identical scaling of these two quantities demonstrates that the proximity of lattice defects to the p-n junction is a primary cause of anomalous pixel behavior, including elevated dark current. This data explicitly shows that as the implant size increases, the probability of defect intersection with the active region of the pixel does as well. This relationship is well established in the literature for a wide variety of semiconductor photodiodes [13, 61, 62, 14, 63].

The lesson for future detector development is clear: if the other effects of small implant size can be mitigated or leveraged, smaller junction implants should increase the operable pixel yield. The pixel yield argument is particularly impactful in the context of MCT-on-Si detectors, given the increased defect density derived from the growth method. The effect is intuitively less impactful on low-defectivity detectors, such as the state-of-the-art grown on lattice-matched CZT.

Multiple studies report that defect densities below $10^5\,\text{cm}^{-2}$ produce negligible impact on photodiode performance, whereas state-of-the-art HxRG detectors achieve defect densities on the order of $10^4\,\text{cm}^{-2}$ or lower [14, 62]. Although the exact defect density in the SATIN detectors cannot be disclosed (Raytheon proprietary), it is several orders of magnitude higher than $10^5\,\text{cm}^{-2}$. This elevated defect density plays an important role in the discussion of the relative contributions of edge glow (Figures 3.15, 3.16), source-follower glow (Section 3.4.3), and trap-assisted tunneling (Section 2.2.3) to the measured dark current in Section 3.4.6.

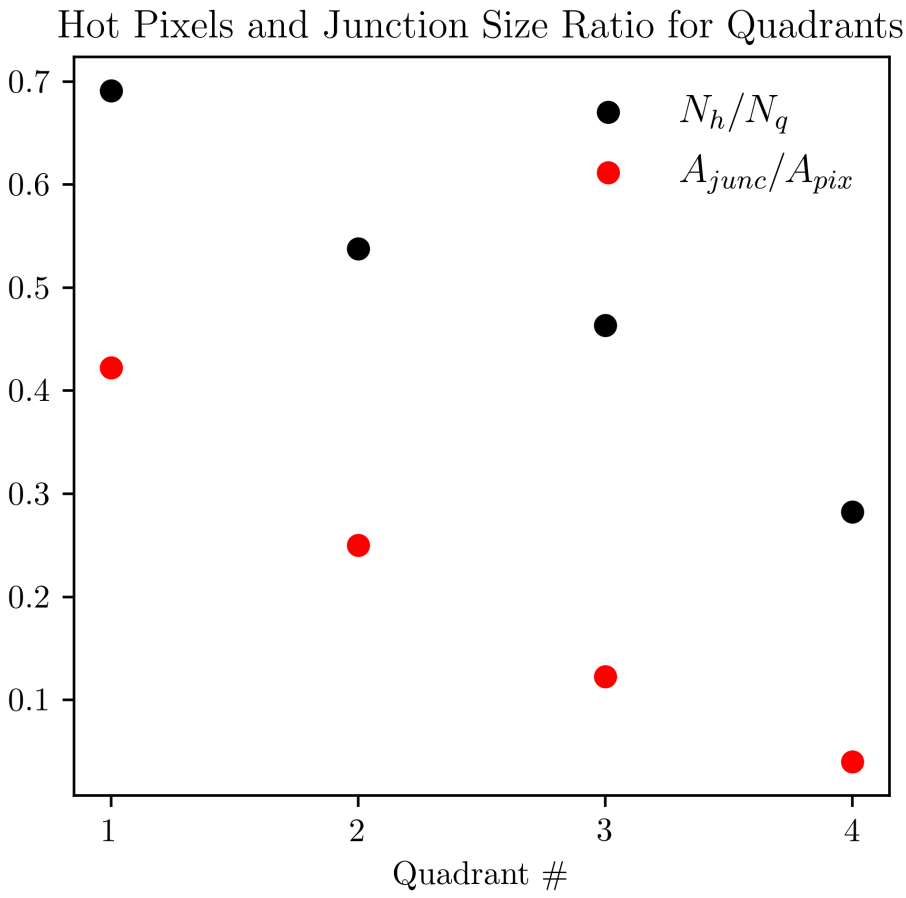


Figure 3.14: This figure presents the fraction of hot pixels $N_h/N_q$ (black) and the geometric fill factor $A_{\rm junc}/A_{\rm pix}$ (red) for each of the four quadrants of detector V23.

### 3.4.2 Glow Background

Glow is an electroluminescence phenomenon that increases the background signal in modern infrared detectors. In detector systems it typically originates from photon emission by the readout integrated circuit (ROIC) [64, 49, 20, 19, 65]. The earliest observation of light emission from a semiconductor diode was reported by Henry Round in 1907, who noted visible luminescence from a silicon carbide crystal under applied voltage. Oleg Losev subsequently demonstrated in the 1924 that the emission from SiC junctions was not thermal in origin. The first quantitative explanation for glow in p-n junctions was provided by Kurt Lehovec in 1951, who attributed it to carriers injected across a forward-biased junction [66, 67].

Several models have since been proposed to describe ROIC glow in infrared arrays. Tam and Hu attributed the emission primarily to bremsstrahlung from hot carriers accelerated in high electric fields [68]. Bude et al. and Carbone et al. predicted peak photon energies in the 0.5–1 eV range [69, 70]. Stellari et al. developed a probabilistic model for photon emission from MOSFET channels that depends on electric-field strength and carrier density [71]. Maestre et al. directly imaged source-follower glow using an infrared EMCCD camera [72, 19]. The most comprehensive study of glow in HgCdTe detectors remains that of Regan and Bergeron who demonstrated that essentially all measured dark current (at cryogenic temperatures) in H2RG devices originates from multiplexer glow. They demonstrated correlations between glow intensity and frame rate, number of samples per ramp, and detector cutoff wavelength—the last providing support for the hot-carrier bremsstrahlung mechanism of Tam and Hu.

### 3.4.3 Sources of Glow

While multiplexer glow is not a completely understood phenomenon, there have been a number of efforts to characterize it in various systems and determine which elements of the circuitry generate it. Of the possible sources of glow, three have been identified in the literature. The first has a drastic effect, and is associated with the clocking circuitry of the ROIC. Overshoot on the clock lines is known to cause glow for these types of IR devices, as it activates diode protection circuitry on the ROIC that cause infrared emission [73]. The location of this diode

protection circuitry was discussed prior and shown as a red region in the bottom-left of the detector in Figure 1.4. The left image in Figure 3.15 shows how this glow manifests in V23 data.

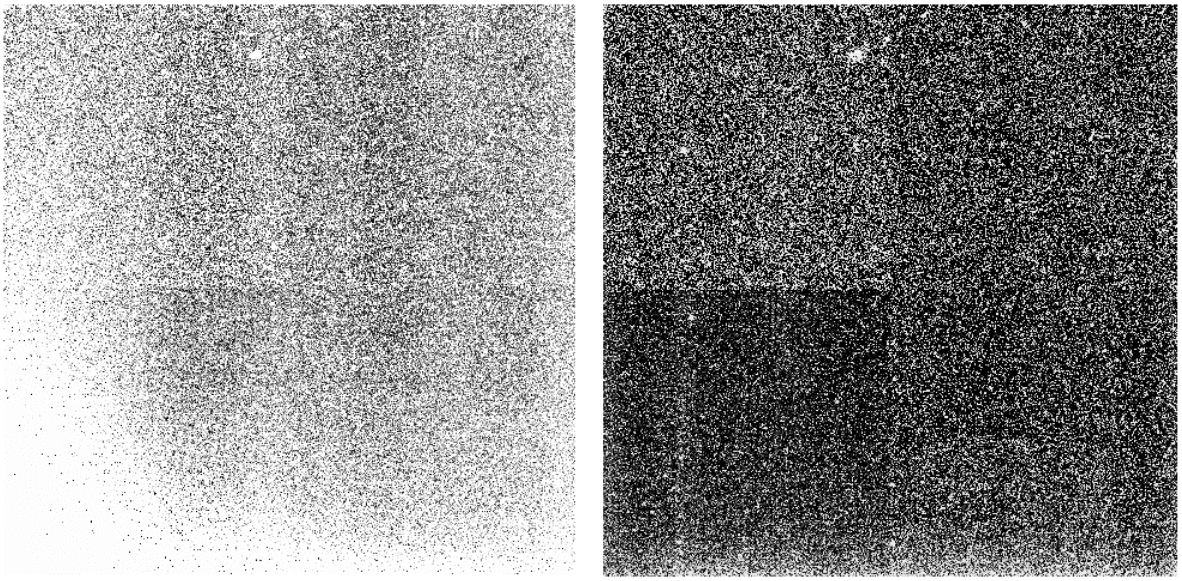

Figure 3.15: This figure shows two dark current slope maps of V23. The scale on both images is drawn such that black represents a pixel slope of 0 e/s and white 0.2 e/s. The image on the left is from data generated without additional resistance in the clock lines, and the image on the right is data taken with an additional 100 ohms on the pixel master clock (PMC) and frame start clock (FSC).

The second glow component arises from the column-selection and output-amplifier circuitry located along the bottom edge of the array. This source produces a pronounced gradient that increases toward the amplifiers, as seen in the right panel of Figure 3.15 [9, 64, 20]. Figure 3.16a displays the median pixel value per row for quadrants Q4 and Q1 (see Figure 1.4), extending from the bottom of Q4 to the top of Q1. The gradient is evident in Q4 and appears to continue into Q1, although the signal-to-noise ratio in Q1 is insufficient for reliable fitting owing to the limited number of well-behaved pixels.

An exponential-plus-constant fit to the Q4 median row profile is presented in Figure 3.16b. The constant term corresponds to the spatially uniform dark current contribution, which includes intrinsic detector dark current plus any glow emitted by the in-pixel source-follower

transistors (whether readout-dependent or steady-state emission). The exponential term represents the distance-dependent glow from the circuitry at the array edge. We find that a double-exponential term fits the data much better than a single exponential, indicating that two component populations are contributing to the glow. The constant component derived from the fit puts an upper limit to the portion of the measured signal that can be attributed to the sum of in-pixel glow and true dark current, amounting to 0.00365 e/s. Unfortunately these two components are tightly entangled, and efforts to completely separate them were unsuccessful, as discussed in the following paragraph.

The third glow component, the in-pixel glow, arises from within the individual pixel unit cell and is generally attributed to the in-pixel source-follower transistor [20, 72, 19]. One method to separate the glow that occurs from reading out each frame from the actual dark current of the pixel is to perform fitting on multiple sets of data which use increasingly more sparsely sampled frames [20]. The electronics used for our experiments allow for the implementation of 'dropped' frames, which is a wait time during which no clocking is sent to the detector chip. In the idealized case, the detector should not accumulate any charge aside from the actual dark current during these dropped frames. We attempt to generate maps of the dark current and per-frame glow components by taking three datasets of equivalent total integration time (t≈100 s): a) UTR,100,1,0 b) UTR,34,1,2 and c) UTR,12,1,9 (see Section 1.4.3 for UTR naming convention). For each ramp type we take 30 sets of ramps, subtract the first frame of the ramp to remove the reset effects, average the results of the last 20 sets, and then perform fitting of the results using:

$$S_{\text{total}} = \frac{S_{\text{PFG}} X}{t} + S_D \tag{3.4.1}$$

where $S_{\text{total}}$ is the total signal of the pixel, $S_{\text{PFG}}$ is the signal from per-frame glow, $X$ is the total number of frames (reads) in the ramp, $t$ is the integration time, and $S_D$ is the signal from the dark current component.

Fitting this to the data and solving for $S_D$ and $S_{\text{PFG}}$ yields the two maps shown in Figure 3.17. Of particular note is the presence of increased current at the bottom of the array even in

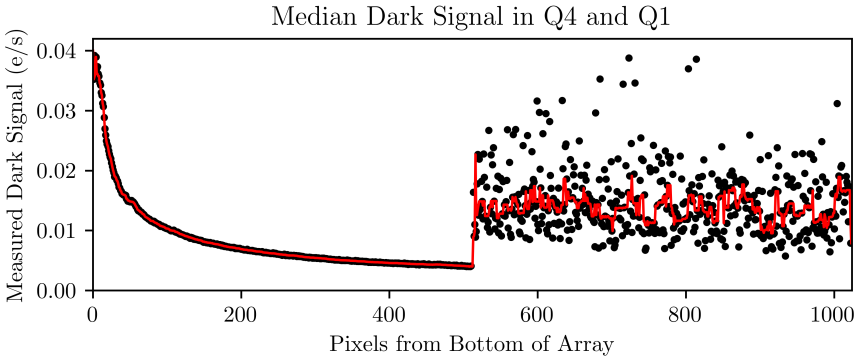


(a)

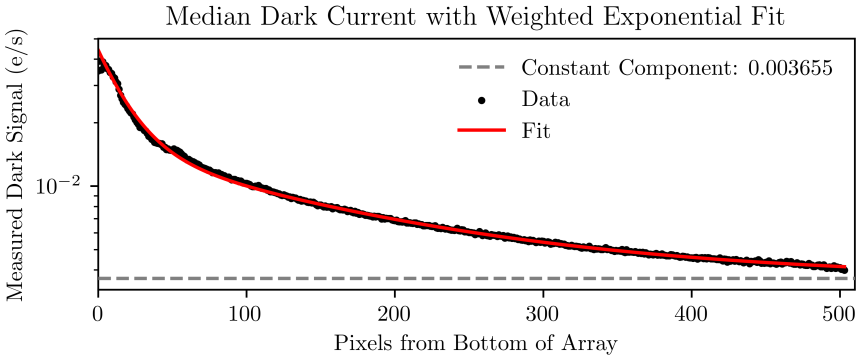


(b)

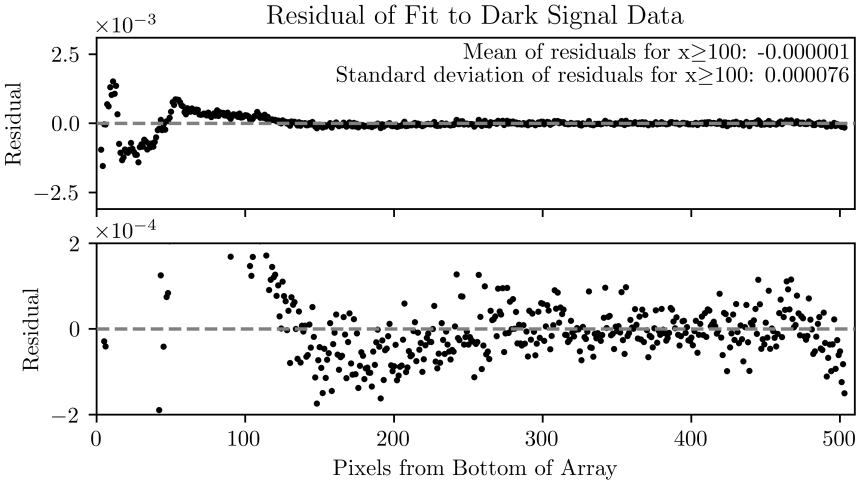


(c)

Figure 3.16: The top panel of this figure displays the median signal per row across quadrants Q4 and Q1, showing the glow-induced gradient that increases toward the column/output circuitry at the bottom of the array. An exponential-plus-constant fit to the Q4 data is overlaid as a solid curve in the middle panel, and the fit residuals are presented in the bottom panel.

the dark current map, likely due to persistence from the signal introduced by per-frame glow. Unfortunately, the convolution of noise sources (actual dark current, edge glow, persistence from the glow, source follower glow, etc) makes it so this simple model is insufficient to accurately separate the dark current and per-frame glow components. The median value of the best Q4 pixels selected for this analysis in $S_D$ is an order of magnitude higher than the measured dark current, and a number of pixels carry negative values. Similarly, the per-frame glow values are too high, and would result in dark currents far higher than what we measure in our devices. Attempts to refine the model to include these factor were fruitless, as were all attempts to improve the input data (more frames, longer exposures, more datasets, using only datasets with frame times longer than 10 seconds, etc). The nature and magnitude of the edge glow discussed earlier makes it difficult, if not impossible, for this model to converge on reasonable results, though future work should explore more advanced fitting analysis.

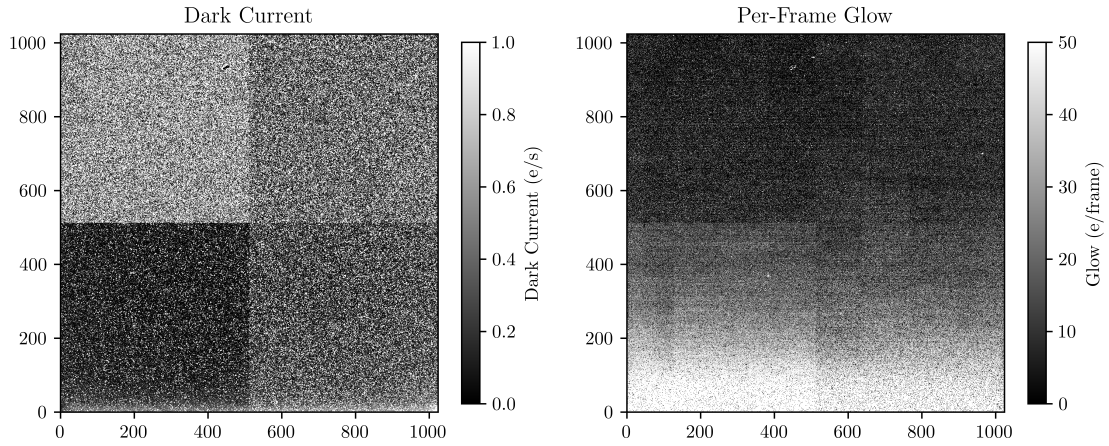


Figure 3.17: This figure shows maps of dark current and per-frame glow for V23, though the values provided by the analysis are incorrect, and too high for the measured dark current.

### 3.4.4 Mitigating Glow

The prominent clocking-overshoot glow component in detector V23 can be suppressed by two independent methods. The first method reduces the clock power-supply voltage CLKPWR, thereby decreasing the overshoot amplitude, which scales with the applied voltage. The second method inserts series resistance into the clock lines, damping the ringing and preventing the

overshoot from activating the ROIC protection diodes. Adding sufficient series resistance eliminated this glow contribution entirely: beyond approximately 20 Ω the overshoot no longer triggered electroluminescence, and further resistance produced no additional reduction.

Figure 3.18 presents oscilloscope traces of the frame-start clock (FSC) which triggers the readout of a single frame within a ramp, and the pixel-master clock (PMC) which initiates pixel timing at the start of the ramp, with and without added series resistance. The left panel shows the large ringing present without resistance; the right panel shows the effectively damped waveforms obtained with 100 Ω of added resistance on each line.

Modifying CLKPWR was shown to be effective, but unnecessary when sufficient resistance is added to the clock lines. Figure 3.19 shows two plots; The left panel plots measured glow intensity versus CLKPWR voltage, both with and without added clock-line resistance. The right panel plots glow intensity versus added series resistance, demonstrating saturation of the suppression effect above approximately 20 Ω. In both cases, all data is taken using a fast readout mode: UTR,35,1,0.

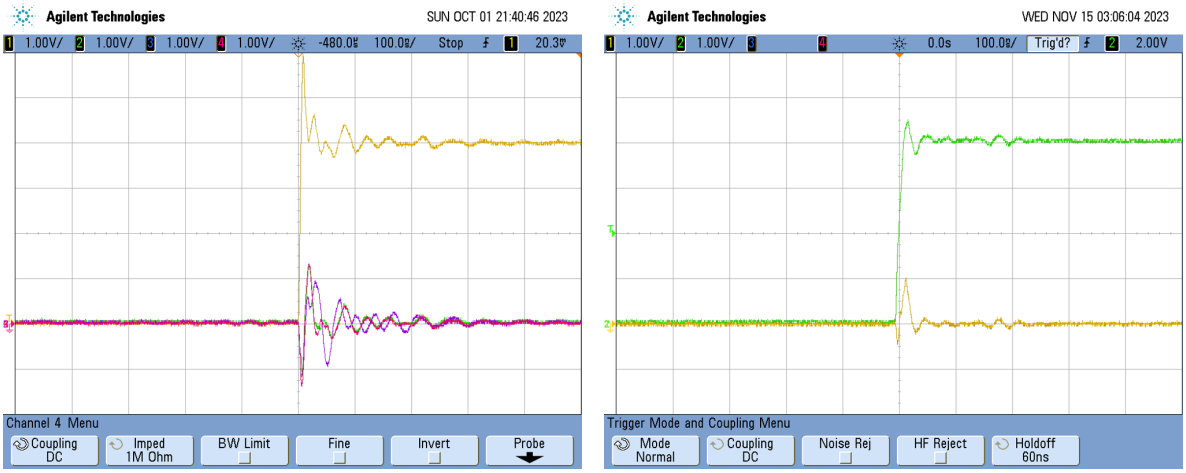


Figure 3.18: This figure shows two oscilloscope measurements of clock ringing in V23. The image on the left is generated without additional resistance in the clock lines (PMC, yellow; FSC, green), and the image on the right is data taken with an additional 100 ohms on the PMC (yellow) and FSC (green).

The persistent glow at the bottom of the detector has proven much harder to mitigate. Literature on glow reduction in the HxRG family of detectors has shown that changing certain

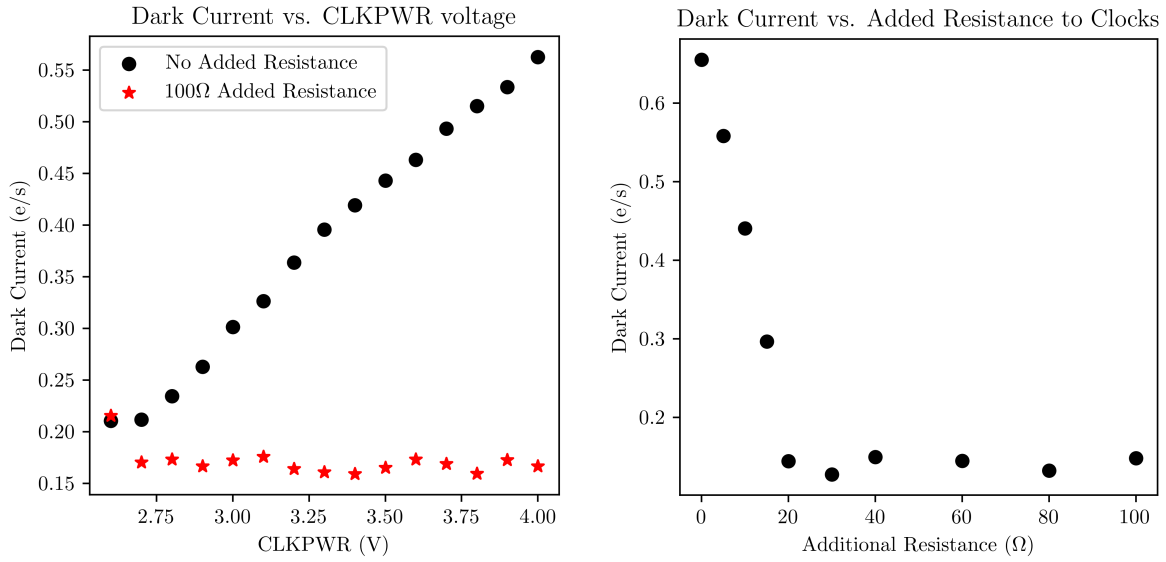


Figure 3.19: This figure shows two plots; On the left, the median measured dark signal is shown as a function of the CLKPWR voltage, with and without added clock line resistance. On the right, the plot shows a decrease in dark current with added clock resistance at a constant CLKPWR voltage.

voltages, such as increasing the drain voltage on the output buffers, can significantly reduce the edge glow, albeit with significant diminishing returns as the drain voltage rises [65]. However, testing this effect in the VIRGO ROIC (*e.g.* by modulating VNOUT, see Figure 1.5) has not yielded improvements in the edge glow. Ultimately, we found it sufficient to introduce additional resistance into the lines, and forego reducing CLKPWR. This entirely eliminated any contribution from the clocking glow to the dark current data.

### 3.4.5 Dark Current and Glow as a Function of Sampling Rate

Two types of up-the-ramp read modes were used for the majority of the testing. The first read mode uses continuous 'fast' sampling which reads out frame after frame without pause, is heavily dominated by glow, and is the default operating mode of the device. For the dark current data labeled 'fast' we use UTR,65,1,0, which takes a 65 image sequence of 1 second frames (see Section 1.4.3 for a discussion of the UTR naming convention). The second read mode uses sparse sampling, where the individual frames have large integration times, during

which the electronics are dormant. For this mode we use UTR,35,1,999, which is to say that we take 35 frame ramps with individual frame exposure times of 1000 seconds. Figure 3.20 shows two histograms of the dark current, for the fast and sparse dark current modes. The measured dark current for this population of pixels when sampled is invariant with respect to the number of frames in a ramp, so long as the frame integration time remains constant.

The histograms reveal two important features. First, reducing the readout sampling density decreases the median dark current by a factor of approximately 5. Second, the high-current tail of the distribution becomes considerably more populated in the sparsely sampled data.

Each distribution was fitted with a Gaussian function near its peak. The number of pixels lying beyond $\mu+3\sigma$ is indicated on the plots; the sparsely sampled dataset contains nearly three times as many pixels in this tail as the densely sampled dataset. This marked increase in the tail population indicates that the intrinsic pixel-to-pixel dark current variation is substantially larger than apparent in high-sampling-rate measurements, where per-read multiplexer glow dominates the signal and masks the true tail. By reducing the glow contribution through sparse sampling, the underlying dark current distribution of the detector array is uncovered, revealing a significant number of pixels with elevated dark current that are otherwise obscured.

Figure 3.21 shows the measured dark current as a function of frame integration time over the range 1–64 s. Each point represents the median measured dark current for a 65-frame ramp, from UTR,65,1,0 to UTR,65,1,99. The observed decrease with longer integration time provides insight into the origin of the edge glow component that arises from the column circuitry at the bottom of the array. As discussed in Section 3.4.2, this glow is not a thermal effect, but electroluminescence originating in the offending circuitry. However, the measured behavior is not unlike a thermal system at equilibrium being perturbed. Consider adapting a model akin to thermal perturbation, where we treat current running through the circuitry as perturbing ('activating') the system and causing an increase in signal generation. The ROIC circuitry must not fully return to equilibrium between successive read cycles. Consequently, the steady-state contribution from glow reached during the available relaxation interval (equal to the frame integration time) governs the magnitude of the induced glow. We model contributions

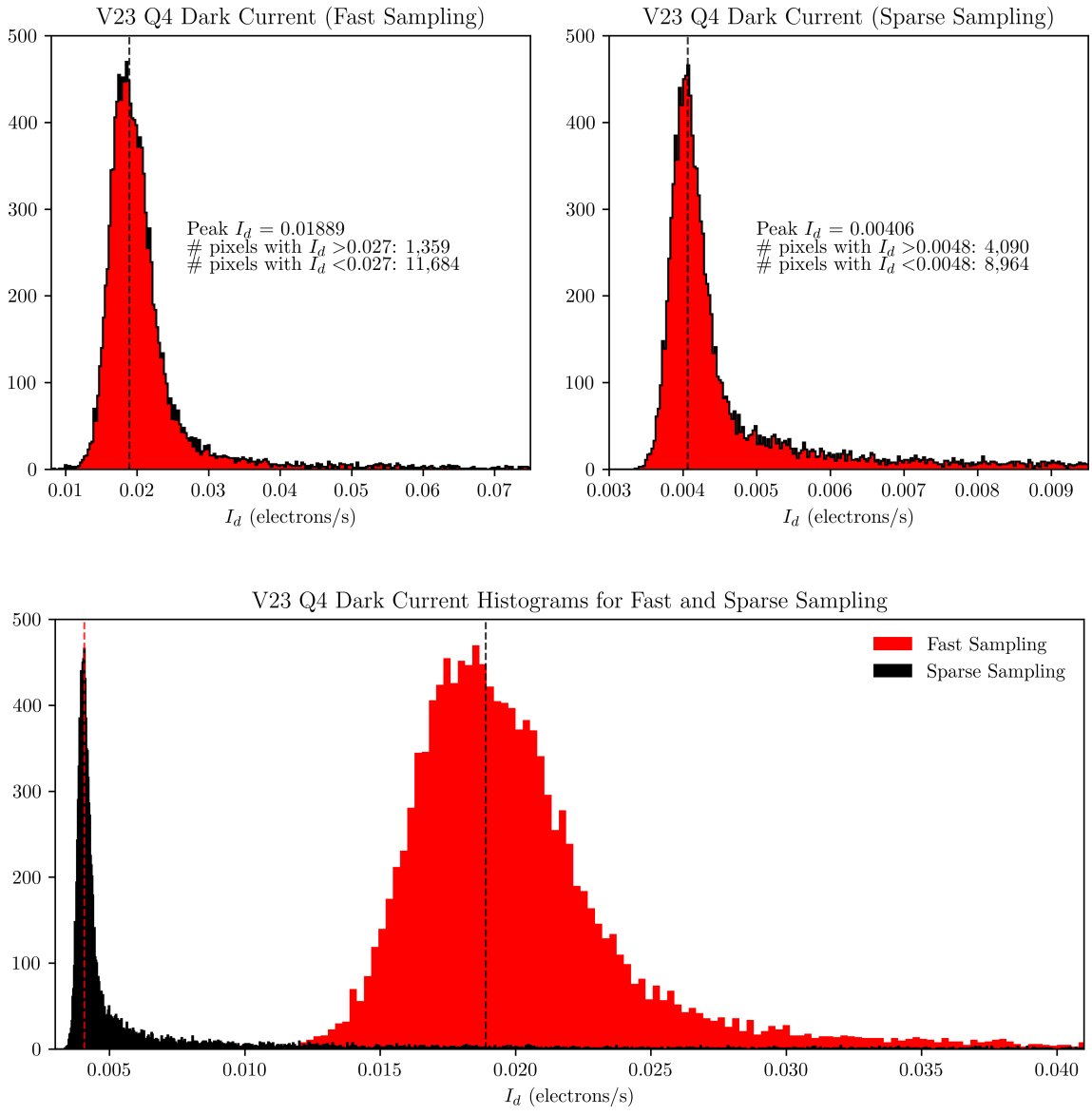


Figure 3.20: This figure shows two dark current histograms for V23. On the left is one taken for continuously sampled UTR frames, while the one on the right shows dark current for UTR frames with 1000 s integration times. The bottom histogram displays both on the same axis, for comparison.

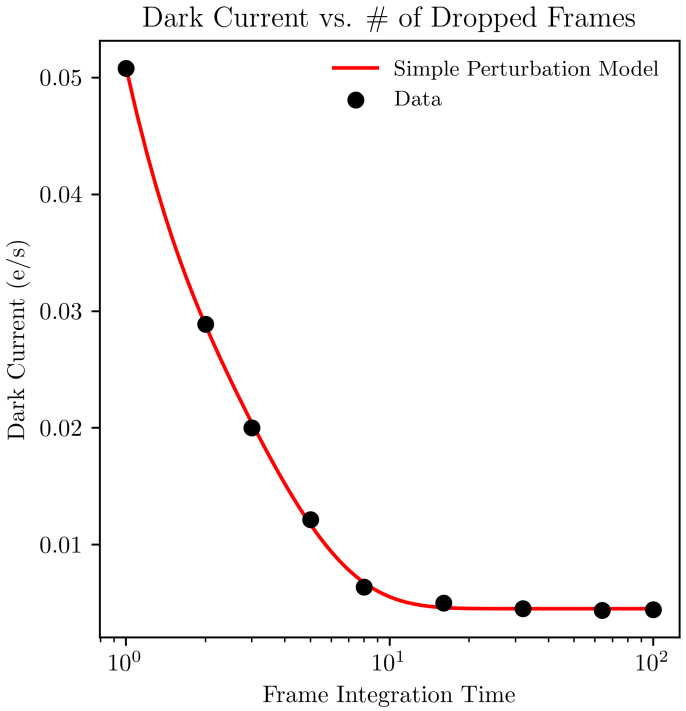


Figure 3.21: This figure shows how measured dark current decreases as the frame integration time increases.

to this glow from two component populations, one which equilibrates quickly and one that does so slowly, as was done for the work regarding this edge glow shown in Figure 3.16. A simple relaxation model like this is overlaid on Figure 3.21, which reproduces the observed trend without requiring detailed knowledge of the circuitry. The simple model is shown in Equation 3.4.2:

$$S_s = S_1 \exp\left(-\frac{t}{\tau_1}\right) + S_2 \exp\left(-\frac{t}{\tau_2}\right) + \alpha \tag{3.4.2}$$

where $S_s$ is the glow signal generation rate to which the readout circuitry settles, $S_1$ and $S_2$ are the signal generation rates for continuous operation of the two component populations, $t$ is the integration time, $\tau_1$ and $\tau_2$ are timescale factors, and $\alpha$ represents the signal in the absence of edge glow. The fitting produced relaxation timescale factors of 0.38 s and 2.5 s, respectively. The first component produces 3× the glow of the second, but relaxes more quickly than the second.

The model presented here is deliberately simplified. It demonstrates only that a basic relaxation description can reproduce the observed dependence of edge-glow intensity on frame integration time. A comprehensive physical model, constructed with detailed knowledge of the ROIC layout, power-dissipation sites, and three-dimensional optical propagation paths, would be required to quantitatively account for the spatial gradient across the array and the partial absorption or scattering of emitted photons by intervening structures.

### 3.4.6 Dark Current Temperature Dependence

Figure 3.22 presents an Arrhenius plot of the measured dark current for the nominal pixel population in Q4 of V23. The data, plotted as red points, are the average result of four ramps, each with UTR,5,1,999. The plot displays the individual contributions from each major dark current mechanism discussed in Section 2.2, the Rule-22 prediction (adjusted for our detector parameters), and the sum of all mechanisms. Because the manufacturer does not disclose detailed device parameters (doping concentrations and profiles, defect densities, absorber thickness, etc.), the theoretical curves were calculated using the best available estimates derived from published literature, historical program documentation, and engineering

correspondence.

The edge-glow component (orange), previously isolated as the difference between the exponential term and constant component in the gradient fit of Figure 3.16, is included in the Arrhenius plot. This distance-dependent contribution establishes a lower bound on the fraction of measured dark current originating from the column/output circuitry at the bottom of the array. For the pixel population analyzed here, edge glow accounts for at least 10% of the total dark current at the lowest temperatures, corresponding to approximately 0.0004 e/s out of the measured 0.0040 e/s. The measured dark current as a function of temperature is plotted in red datapoints, with the median edge glow contribution subtracted out.

#### 3.4.6.1 Dominant Mechanisms

The dark current between 100K and 120K is dominated by G-R currents, which are plotted in dashed black as modeled in Section 2.2.2. Above 120K, the dominant effect becomes diffusion, plotted in dotted black as modeled in Section 2.2.1. The knee between 80K and 100K is where surface currents (solid black, Section 2.2.4), G-R currents, tunneling currents, and glow intermingle. The fit to the data is marginally improved by the presence of the surface currents, which bring the fit closer to the data, although the cumulative components still underestimate the dark current between 80K and 90K. Below 90K the dominant mechanism in the measured dark current is an inseparable combination of in-pixel glow and tunneling currents.

The high slopes of the diffusion, G-R, and surface current models reflect their strong temperature dependence, whether directly or through $n_i$ as defined in Equation 2.1.9. The flat profile of the tunneling components reflects independence from temperature, as they depend primarily on intrinsic doping concentrations and the applied bias voltage.

The remaining dark current floor consists of entangled TAT current and in-pixel glow, which amounts to 0.0036 e/s - only twice the median reported for the WFIRST detectors [32]. We are unable to put reasonable limits on the contributions of the individual components to this final dark current factor, but it is clear that at 70 K the data are still dominated by ROIC glow, especially in read-modes that don't use excessively long frame integration times. Future

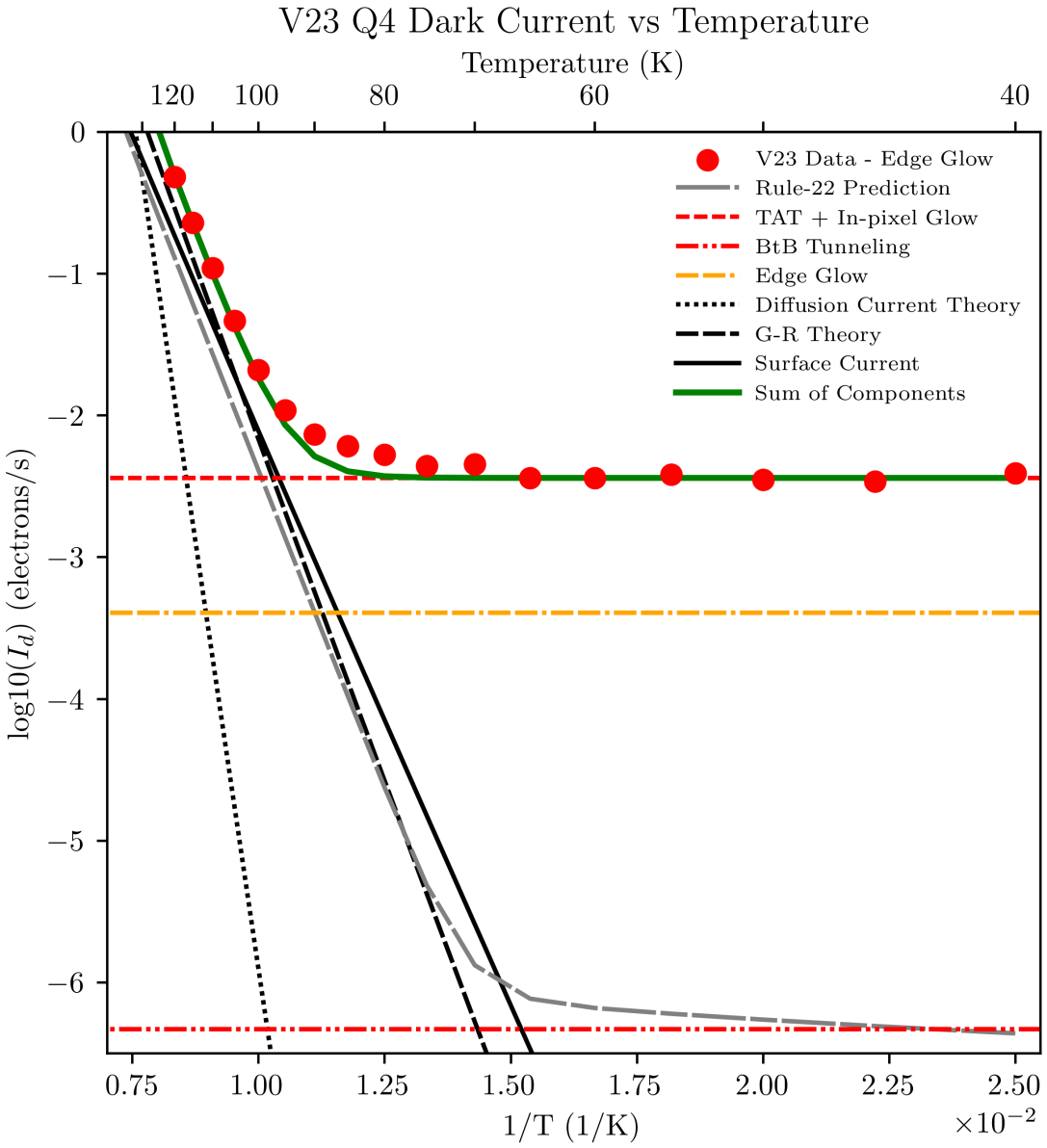


Figure 3.22: This figure shows the dark current as a function of temperature for Q4 of V23. The black lines show the components that come from diffusion, G-R, and surface currents, the red lines show contributions from direct and trap-assisted tunneling, the orange line represents the edge glow, the gray line shows the Rule-22 model adjusted for our cutoff wavelength and junction implant size, and finally a green line representing the sum of orange, red, and black components.

work to fully characterize the in-pixel glow may be possible, and measurements with a more advanced ROIC would significantly reduce the difficulty in making this possible.

#### 3.4.6.2 Rule-22 Comparison

The Rule-22 model (discussed in Section 2.2.5) is plotted in light-gray dashes in Figure 3.22. The model was evaluated using pixel parameters for the V23 device. The first slope, the $J_1$ term, is in good agreement with the data, albeit slightly underestimating the actual dark current. The second and third terms, $J_2$ and $J_3$, obviously significantly underestimate the measured dark current. The knee in the Rule-22 model from the $J_2$ term reflects the behavior seen in the data, despite the underestimation of the magnitude. As discussed previously, this is because the $J_2$ and $J_3$ terms are meant to model the non-ideal backgrounds present in the highly-developed Teledyne detectors, not this engineering array from the SATIN lot. As the combined contribution from the glow background and TAT dark current components are significantly higher than in low-defectivity arrays, this deviation is expected.

### 3.4.7 Conclusions on Dark Current

The dark current results for V23 are extremely promising, and demonstrate that the actual dark current of the detector pixels is more than an order of magnitude lower than previously published [33]. The high dark current reported previously was heavily dominated by glow, not true dark current mechanisms. This means that the fundamental MCT-on-Si performance is far closer to the state-of-the-art than previously indicated.

One unresolved question concerns the contribution from emission by the in-pixel source-follower transistor. In more mature Teledyne HxRG detectors, multiplexer glow generated within the pixel itself has been shown to dominate the dark current even when extensive mitigation techniques (including opaque metal shielding layers) are employed [20]. Mitigation strategies shown to be effective for the HxRG series—modulation of the source-follower drain voltage and increased pixel clocking speed to reduce current flow duration through the transistor—were tested on the SATIN detectors, yet produced no measurable reduction in

dark current [19]. Given the significant contribution from edge glow, it is still not possible to disentangle the TAT current from in-pixel glow, nor make definitive statements on which is dominant within the remaining signal.

## 3.5 Crosstalk

Crosstalk is a phenomenon where neighboring pixels in an array exhibit a coupling of signal between them. Crosstalk can be caused by many mechanisms, but the simplest form can be imagined as charge being generated in one pixel and being captured by a neighboring one. It is a charge diffusion process described by random walk of electrons, weighted by the electric field within the pixel. The term random walk was first defined by Karl Pearson in 1905 [74]. He wrote:

> *A man starts from a point $O$ and walks $\ell$ yards in a straight line; he then turns through any angle whatever and walks another $\ell$ yards in a straight line. He repeats this process $n$ times. I require the probability that after these $n$ stretches he is at a distance between $r$ and $r + \delta r$ from his starting point, $O$.*

The solution to this problem is:

$$P_n(r) = \frac{2}{n\ell^2} \exp\left\{-\frac{r^2}{n\ell^2}\right\} r dr \tag{3.5.3}$$

where $r$ is measured in the same units as $\ell$. This treatment isn't ideal for our situation as it assumes equal step sizes and fails to account for the aforementioned drift, but it serves as a good starting point [31]. Mosby uses this solution and tailors it to apply more appropriately to the physics of the pixel, accounting for the fact that the pixels drift in three dimensions, not two, and that the hole drift ends after $n$ collisions due to the electric field. Mosby generalizes Rayleigh's solution by replacing $\ell$ with the mean free path of holes $\lambda_h$ projected onto the x-y plane:

$$\ell = \frac{\pi}{2} \int_0^{\frac{\pi}{2}} \sin(\phi) d\phi \lambda_h = \frac{2}{\pi} \lambda_h \tag{3.5.4}$$

Substituting that into Equation 3.5.3 and solving to get the charge-spreading point spread function (PSF):

$$\Psi(r) = \frac{\pi}{4n{\lambda_h}^2} \exp\left(-\frac{\pi^2 r^2}{4n{\lambda_h}^2}\right) \tag{3.5.5}$$

which is a two-dimensional gaussian with a standard deviation of:

$$\sigma = \frac{\lambda_h}{\pi}\sqrt{2n} \tag{3.5.6}$$

The number of steps taken ($n$) can be calculated as a ratio of the time needed for a hole to drift out of the absorber ($\tau_d$) to the mean scattering time ($\tau_s$):

$$\tau_d = \frac{z}{\mu_h |E_d|} \tag{3.5.7}$$

$$\tau_s = \frac{\mu_h m_h^*}{q} \tag{3.5.8}$$

$$n = \frac{\tau_d}{\tau_s} \tag{3.5.9}$$

where $|E_d|$ is the drift field amplitude (which decreases with distance from the 'center' of the p-n junction), $\mu_h$ is a hole mobility parameter, $m_h^*$ is the effective mass of holes, and $q$ is the elementary charge. The mean thermal velocity of holes ($v_{th}$) multiplied by the mean scattering time yields the mean free path of holes in the detector:

$$v_{th} = \sqrt{\frac{kT}{m_h^*}} \tag{3.5.10}$$

$$\lambda_h = v_{th}\tau_s \tag{3.5.11}$$

which yields the charge-spreading PSF as a function of real detector parameters:

$$\sigma = \frac{1}{\pi}\sqrt{\frac{2kTz}{q|E_d|}} \tag{3.5.12}$$

where $T$ is the temperature, and $z$ is the vertical distance traveled, which is on the order of the thickness of the absorber layer [31]. Mosby's solution, presented above, presents an

important inverse-root relation between $E_d$ and $\sigma$. It is extremely relevant for detectors like V23, which operate at high reverse biases, and thus have high $E_d$. Modeling of threading dislocations in MCT also suggests that the space around threading dislocations has increased electric potential, which should contribute to this shrinking of $\sigma$, especially in a material as defective as that of V23 [14].

Several techniques exist for measuring interpixel crosstalk. Passive approaches rely on rare, randomly occurring events: cosmic ray hits during long dark exposures or X-ray photons from a radioactive source such as $^{55}$Fe [31, 32]. Although effective, these methods require substantial total integration time to accumulate sufficient statistics.

Active techniques deliberately create localized charge sources. One established method, developed by Teledyne for HxRG detectors, forward-biases selected pixels to generate controlled hot spots, exploiting the per-pixel reset capability of those ROICs [75, 76]. The VIRGO ROIC used in the SATIN detectors lacks individual pixel addressing, so this approach is not feasible. Gert Finger developed a method in conjuction with Teledyne for measuring crosstalk that directly measures the node capacitance of a pixel and capacitive coupling to the neighbors [77]. Andrew Moore performed spatial autocorrelation of Poisson noise in his data to determine the diffusive and capacitive crosstalk components[78]. For this thesis, crosstalk is quantified using naturally occurring hot pixels within the array as charge-injection sites, and compared to cosmic-ray data.

The crosstalk measurement technique developed for the SATIN detectors circumvents the limited statistics inherent in cosmic ray based methods. At the Center for Detectors the standard approach identifies cosmic ray hits in long dark exposures; however, the extensive shielding of both the dewar and laboratory, combined with the detector orientation, severely suppresses the cosmic ray flux. Moreover, surviving events typically deposit large, highly asymmetric charge clouds that complicate the isolation of conventional interpixel coupling, necessitating rejection of most candidates [76, 79]. Because the engineering-grade SATIN arrays contain abundant naturally occurring hot pixels, an alternative procedure was implemented that exploits these defects as controlled charge-injection sites. The algorithm proceeds as

follows:

1. All persistently high-signal, unsaturated, hot pixels are identified in a dark ramp dataset.
2. Any hot pixel within three pixels of another hot pixel is excluded, along with its neighbor, to eliminate mutual contamination.
3. Hot pixels within four pixels of the array edge are also excluded to avoid boundary artifacts.
4. An empty $3 \times 3 \times N$ array is constructed, where $N$ is the number of identified hot pixels.
5. Each of the $N$ $3 \times 3$ subarrays is populated with the values of the hot pixel and its neighbors, normalized to the signal in the hot pixel.
6. Two $3 \times 3$ arrays are created and populated with the mean and median values for each element through the master $3 \times 3 \times N$ array.

The central hot pixels used in the crosstalk evaluation contain a median of approximately 56,000 electrons, and the rejection algorithm described above ensures that there is no cross-contamination and that the neighboring pixels are all well-behaved. These hot pixels all exhibit this increased signal gain, possibly caused by activation of charge generation sites due to the high reverse bias [39, 61]. Figure 3.23 shows the signal gain in one such pixel in the absence of illumination, plotted for a range of applied reverse biases. While this hot pixel may not be representative of a 'good' pixel, there is no evidence that the source defect causing charge generation would significantly affect the crosstalk mechanisms.

Pixels in Q4 of V23 exhibits a characteristic crosstalk that is very low in the 4-neighbors and near-zero in the 8-neighbors, as shown in Figure 3.24 with the hot-pixel method on the left and the cosmic ray method on the right. All of the results shown are derived from sparsely sampled dark current data, discussed previously. The increased crosstalk in the pixel directly right of center is consistent with capacitive coupling in pixels that follow high signal pixels in the read direction, often attributed to incomplete settling of the output amplifier. This form of capacitive-coupling crosstalk is separate from crosstalk due to charge diffusion. Although the

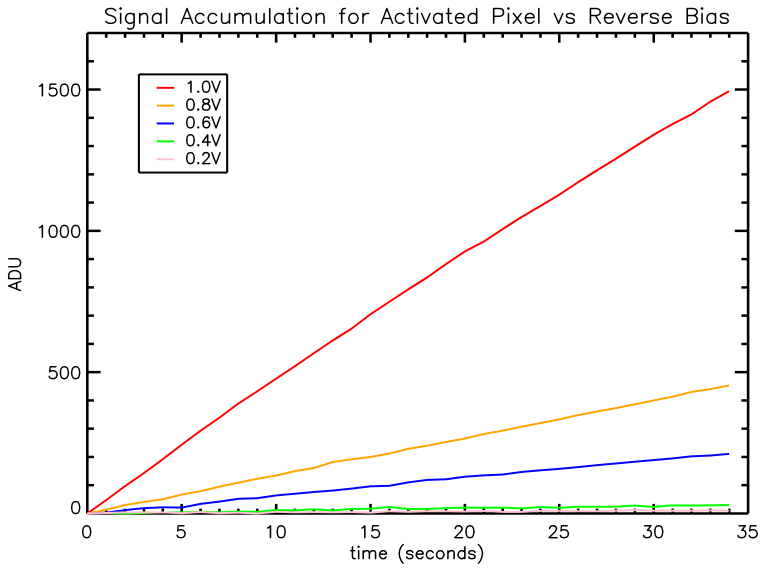


Figure 3.23: This figure shows the increased signal gain in an activated pixel during a dark ramp exposure for a range of applied reverse biases.

number of events shown for the cosmic ray method experiment are low, they are representative of the many other experiments done to test the crosstalk in Q4 of V23. The agreement between the two results is exceptionally close, albeit with some negative values in the 8-neighbors for the cosmic ray result. This effect likely arises due to the much less strict rejection algorithm used in the cosmic ray analysis and the small number of samples.

### 3.5.1 Conclusions on Crosstalk

The crosstalk results for the SATIN detectors are extremely promising, and currently exceed the requirements for a state-of-the-art mission. The Nancy Grace Roman Space Telescope (WFIRST), which will be used to perform challenging observations for weak gravitational lensing studies, has detectors with crosstalk of approximately 2% [31, 32, 80]. Figure 3.24 shows interpixel crosstalk values for V23 that are approximately one order of magnitude lower than those measured in the WFIRST H4RG-10 detectors, more than acceptable for modern science applications. This substantial reduction arises primarily from two factors: minority-carrier lifetime and pixel pitch. V23 employs a 20 $\mu$m pitch (twice that of the H4RG-10) and is

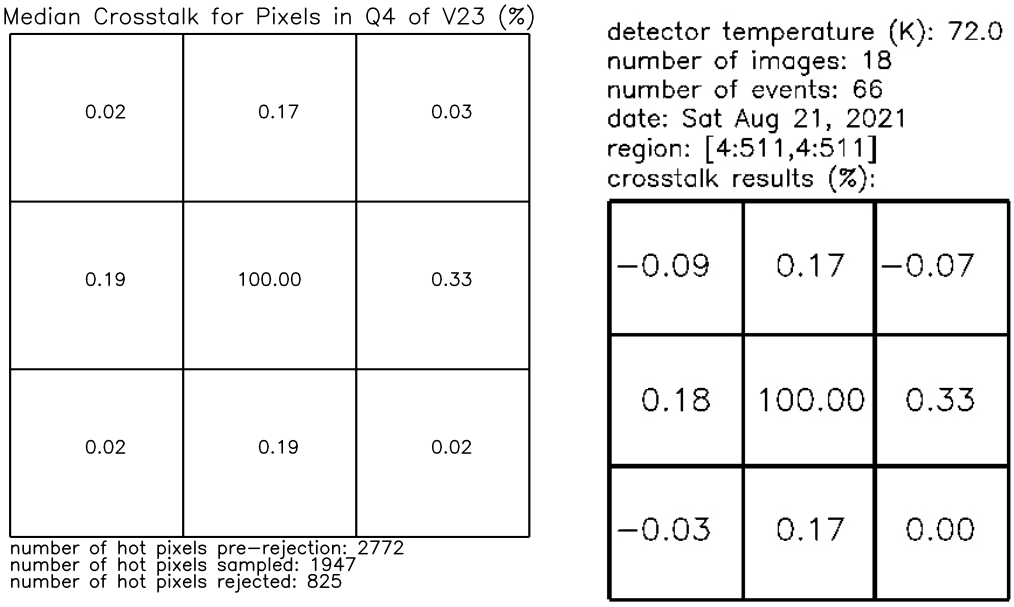


Figure 3.24: The figures above show median values for crosstalk around hot pixels ("events") and as measured from cosmic ray events.

fabricated on significantly more defective HgCdTe material, which decreases carrier lifetime, diffusion length, and thereby suppresses lateral charge spreading. The two devices operate under comparable conditions in other respects: identical detector reverse bias magnitude (1 V), similar absorber thickness, and low-viscosity epoxy fill between indium bumps for mechanical support—a feature known to increase crosstalk relative to air-filled gaps because of the higher dielectric constant of epoxy [33]. Unfortunately, as the MCT-on-Si detectors are refined to improve dark current performance, defectivity will be reduced, and pixels are likely to shrink, so the crosstalk is sure to rise. It is unlikely, however, that they will rise significantly above what is acceptable in current state-of-the-art detectors.

## 3.6 Linearity

As described in Section 2.1.2, the reverse-biased p-n junction behaves as a parallel-plate capacitor whose capacitance increases with collected charge. As charge is integrated, the response of the pixel to further illumination weakens. Figure 3.25 shows the average fractional countrate

for pixels in Q1 and Q4 of V23, which have p-n junction implants of 13$\mu$m and 4$\mu$m, respectively (see Section 1.4.) The curves show how the response of the detector to individual units of charge decreases as the storage well of pixels fills. The Q1 pixels behave as expected, with a gradual and near-linear drop in response as charge is integrated. This trends as expected with the dominant source of capacitance in the pixel, which is the sum of $C_s$ and $C_b$ (defined in Section 2.1.2). We base these capacitance values on reasonable estimates for the sizes of the components based on engineering communications for earlier SATIN devices, including the gate geometry and the depth of the pixel. The Q4 pixels exhibit a significant drop in signal response at about 50% of the full well depth, which seemingly approaches a plateau before the pixel saturates and detector response goes to zero.

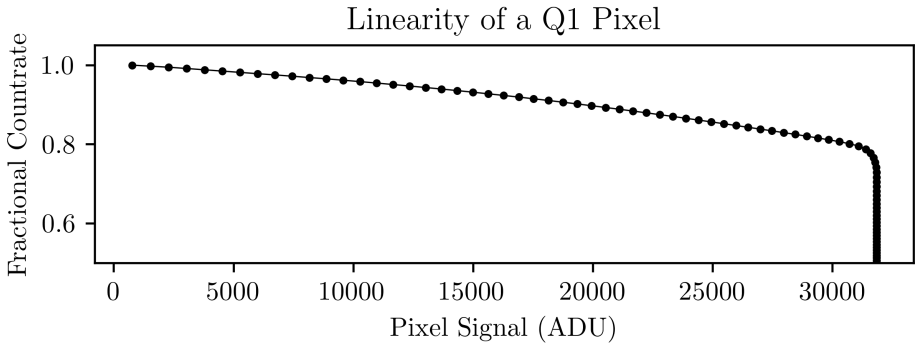


(a)

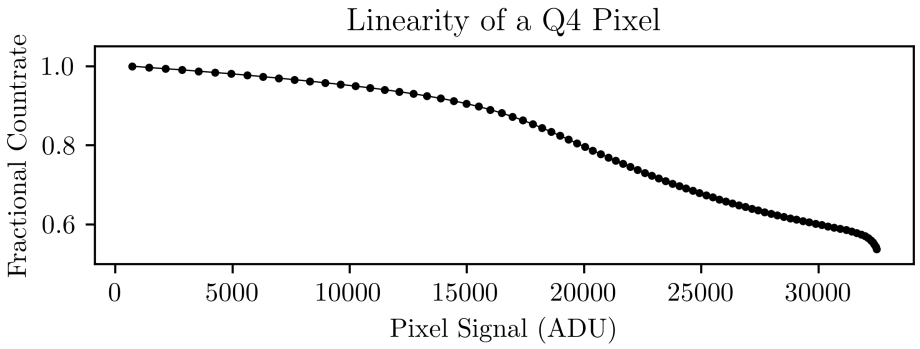


(b)

Figure 3.25: These plots show the fractional countrate of pixels in Q1 and Q4 as a function of increasing charge within the pixel.

Figure 3.26 presents calculated capacitance contributions for the p-n junctions in quadrants

Q1 and Q4. The bottom-junction capacitance $C_b$ scales with implanted area, whereas the sidewall capacitance $C_s$ scales with junction perimeter. Consequently, $C_s$ becomes dominant as the implanted junction area is reduced. This trend agrees with published results and confirms that the parameter values adopted here—necessarily estimated in the absence of proprietary device specifications—yield physically reasonable behavior [81, 34, 35]. The gate capacitance $C_g$, assumed independent of junction area, is also plotted; it becomes the largest term at the smallest implant sizes.

By combining $C_b$, $C_s$, $C_g$, and a small fixed parasitic capacitance, the expected non-linearity of pixel response can be simulated. One such calculation is shown in Figure 3.27 and successfully reproduces the overall shape of the measured linearity curve presented in Figure 3.25. As noted in Section 2.1.2, accurate modeling of pixel non-linearity requires detailed knowledge of the ROIC architecture, which is not available. With knowledge of those structures, particularly their sizes, spacing, and physical location relative to one another it would be possible to perform fitting to the data, but any attempt to do so without that information would not be physically meaningful. The model presented here therefore represents the most practical approximation achievable with the information available.

### 3.6.1 Conclusions on Linearity

Linearity in V23 is shown to vary strongly with the size of the p-n junction, primarily due to conflicting capacitances within the ROIC structure. The smallest junction implant size has been shown to be the most favorable for reducing dark current, as discussed in Section 3.4, but clearly displays the most non-linear behavior. While non-linearity is generally highly correctible, sciences cases with challenging observations such as those done for weak lensing surveys require low errors in those corrections [82].

Note that the VIRGO ROIC used for the SATIN detectors was not custom-built for that application, and is a generic product of RVS. Were a proper ROIC designed for these devices, with the small junction capacitance in mind, it should be possible to strongly mitigate or eliminate the highly non-linear behavior of the Q4 pixels. As with dark current there is

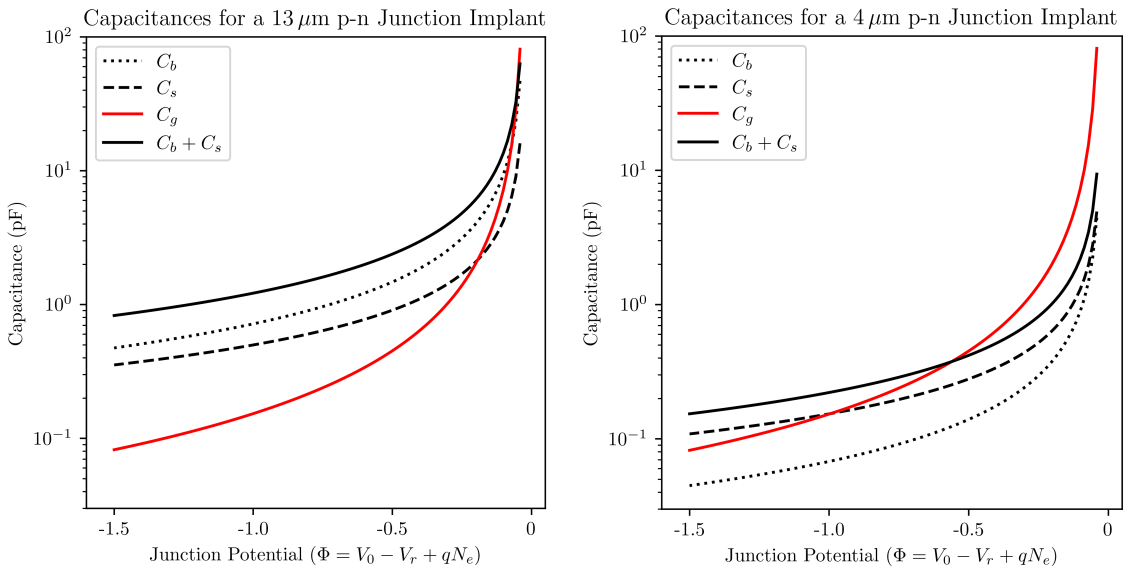


Figure 3.26: The left panel of this figure shows the bottom-junction capacitance $C_b$, sidewall capacitance $C_s$, and gate capacitance $C_g$ calculated as functions of collected charge for pixels with the 13 $\mu$m junction implant. The right panel shows the same three capacitance components for pixels with the 4 $\mu$m junction implant.

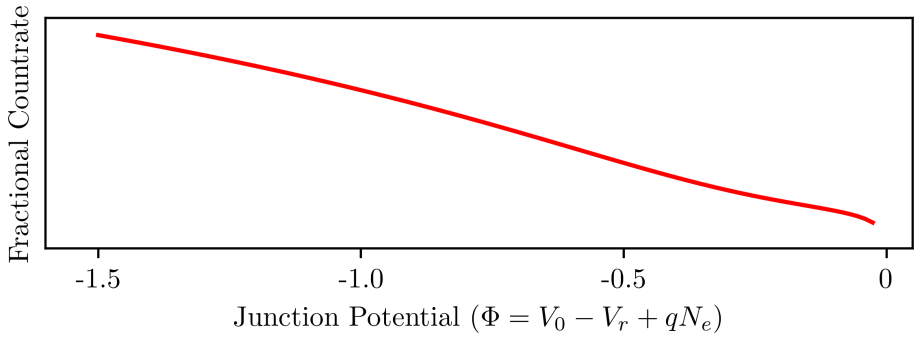


Figure 3.27: This figure shows the simulated expected non-linearity for Q4.

likely space to improve the performance by adjusting the structure of the pixel implant, but significant changes will be achieved with a more developed ROIC.

Ultimately, this is problem that arises not due to fundamental issues with the detector material or growth process, but from an incomplete detector development methodology. These detectors are engineering grade, built to test the material at base - a pointed detector development effort would involve a ROIC tuned for the detector that's being attached to it. The dominance of Teledyne in the detector market is not only owed to the excellent material processes they utilize, but also the significant investment they have made into developing the HxRG ROIC technology. A similar effort will be required to bring RVS detectors to the forefront of state-of-the-art imaging detectors.

# Chapter 4

# On-Sky Verification

*This chapter is based on previously published work:*

**1.** Buntic, Lazar, et al. 2024, *Advancing Large Format MCT/Si Infrared Detectors for Astrophysics Research*, SPIE Proceedings Volume 13103, DOI: 10.1117/12.3019111

The detector system was deployed at the University of Rochester's C.E.K. Mees Observatory (42° 42′ 1″ N, 77° 24′ 31.56″ W) from December 7, 2023, to January 18, 2024. Observations of various planets, galaxies, stars, and star clusters were planned, though not all were performed. Unfortunately, as expected in northern New York, the winter weather was uncooperative, rendering most of the scheduled nights at the observatory useless due to cloud cover and snow. However, a few clear nights (spanning December 13 to December 16, 2023) were utilized to generate the results presented here.

## 4.1 Observing Equipment

The system, as deployed, is shown in Figure 4.1. The orange dewar houses the detector, which is cooled by an Edwards Ltd. (Burgess Hill, U.K.) model 9600 helium compressor. A Lake Shore Cryotronics Inc. (Westerville, OH, U.S.A.) temperature controller monitors temperatures and maintains heater power throughout the observing period. JMClarke Engineering (Simi Valley, CA, U.S.A.) provided the set of detector electronics used to run the detector. This system and equipment are very similar to other experiments deployed by the Center for

Detectors [83, 84]. Custom fixtures were designed and fabricated by the CfD team to interface the dewar system with the telescope and mount the detector electronics. A Parker Hannifin Corp. (Mayfield Heights, OH, U.S.A) OEM750 Step Motor Indexer/Drive operates the filter wheel inside the dewar, which contains a set of J, H, and K-band filters from Materion Corp. (Westford, MA, U.S.A.). Table 4.1 lists the properties of the filters.

Table 4.1: This table lists the properties of the filters used for the observing program. The cut-on and cutoff wavelengths represent half-power points, and the transmission is the average of all transmission values above 70% for each filter. Note that the K-band filter used for this program is distinct from the 2MASS $K_s$ filter.

| **Filter Name** | **Cut-On $\lambda$ (nm)** | **Cutoff $\lambda$ (nm)** | **Transmission (%)** |
|---|---|---|---|
| J | 1111 | 1383 | 80 |
| H | 1507 | 1798 | 90 |
| K | 2005 | 2400 | 91 |

The C.E.K. Mees Observatory telescope is a 60-centimeter f/13.5 Cassegrain telescope located in Ontario County, New York State[1]. Constructed in 1965, the telescope has been modernized and is operated by a fully computerized control system built by the University of Rochester. The telescope is situated at the top of Gannett Hill, an hour south of the city of Rochester. As with many other observatories, the expansion of nearby cities over the past few decades has significantly increased light pollution in the locale. However, our NIR observations remain unaffected by city lighting because the sodium lamps typically used for street lighting cause optical line emission, which is filtered out by our near-infrared observing filters [85]. More significant challenges include tracking and focus instabilities due to the telescope's age - a few instances of gear slippage and drift in the focus position ruined some longer exposures.

## 4.2 Observation Targets

Several targets were selected for the observing program based on their accessibility during the observing period, breadth of brightnesses, and suitability for testing the detector's range of capabilities. The targets provide a rich variety of objects for both photometry and detector

[1] `https://www.sas.rochester.edu/pas/about/observatory.html`

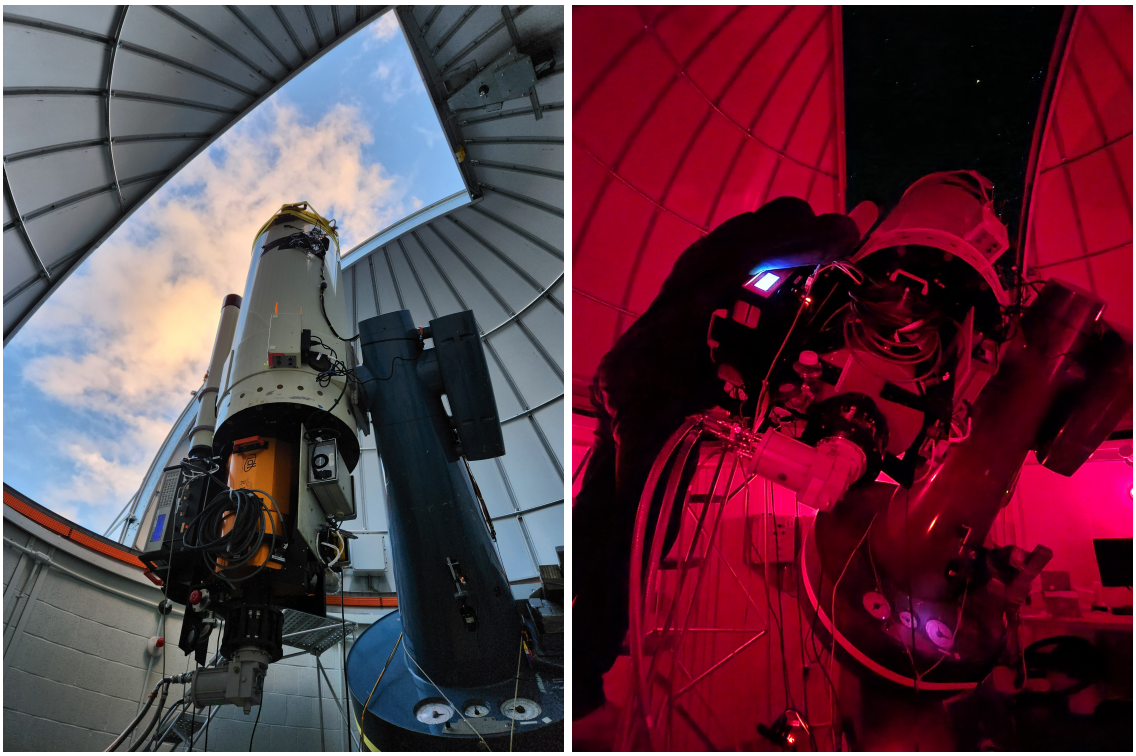

Figure 4.1: This figure shows the detector system as deployed at the Mees Observatory. In the left panel, the orange dewar contains the SATIN V23 detector chip. To the left of the dewar are the electronics used to monitor and maintain the system temperature, and to the right are the detector electronics.

characterization. This thesis presents the photometric results for the M42, M29, and M37 clusters.

## 4.3 Data Reduction for Observations

Observation data is captured from the detector and output into the astronomy-standard `.fits` format using custom IDL routines. Numerous tools are available for manipulating `.fits` files in essentially every major computing language, often rooted in code written with the IRAF command language in 1981 [86]. All results shown below were generated using custom code written in IDL.

Multiple datasets were taken for each object in each of the observing bands (Johnson J, H, K), and the telescope was dithered for each dataset. Dithering, a well-established practice in observational astronomy, involves shifting the field-of-view by a few arcseconds between exposures. This technique ensures robustness against cosmic ray hits and bad pixels during reduction by varying the landing position of the star's point-spread function (PSF) across different pixels. By doing so, one can effectively reject information that lands on bad pixels without compromising data completeness, which is maintained by co-adding exposures [87]. This also controls for pixel-to-pixel variation in QE, which is always present in CMOS devices.

We collect science data 'up-the-ramp' by taking a series of non-destructive reads over a set exposure time while the telescope tracks the target [88]. We take calibration frames to accompany each target, including dark current frames ('darks'), sky images, and flat field images ('flats'). Darks are taken when the detector is closed off from the optical path to measure the contribution from thermally generated electron noise in the detector (See Section 3.4). Since darks are independent of the optical path, we usually take them at the start or the end of the observing night, or during the day. It should be noted that taking darks at significantly different times from the data can be problematic for imaging systems that don't have precise temperature controls, since dark current is a thermal effect. Our dewar system maintains a stable 70K detector temperature at all times. We primarily take dark data during the day to maximize the observing time each night. We collect sky images during

data acquisition as one of the dither positions. We take them by dithering the telescope FOV to an area clear of stars to measure the glow and thermal emission of the atmosphere, which we subtract from the data. We take flat frames by illuminating the detector with uniform light and later use them to correct for aberrations in the optical path, such as vignetting [89, 87]. The flats used for the observing program were obtained by imaging the evening sky around sunset, which provided a well-illuminated and gradient-free flat field.

The IDL reduction code first subtracts frame zero from frame $n$ of each ramp in the data, darks, sky images, and flats to remove any residuals from the initial biasing of the detector at the start of the ramp. Second, the code subtracts the darks from the data, flats, and sky images. Third, the code normalizes the flats by their median value and subtracts the sky image from the data. Fourth, the code converts the data from digital numbers (DN) to electrons and divides it by the normalized flat, yielding the final science image which we use to perform photometry. Fifth, the code feeds the science image to a star-finding algorithm that locates the stars in the image and measures them. Finally, the code passes the locations and fluxes of the stars to the master analysis code, which matches the data from all three photometric bands to data from a query of the Vizier 2MASS database, and we plot the results [90]. The following subsections show results for observations of M42, M29, and M37.

## 4.4 M42 Results

M42 (NGC 1976), the Orion Nebula, is one of the brightest nebulae in the northern sky. It is one of the closest star-forming regions to Earth, and has been extensively studied since its discovery in the early $17^{\text{th}}$ century. In 1617, Galileo observed and documented the Trapezium cluster, a bright star association that provides most of the nebula's illumination. M42 also contains the Becklin-Neugebauer (BN) object, a heavily obscured proto-star adjacent to Trapezium [91, 92, 93]. We chose M42 primarily for the BN object, which is brightest in the K-band for our detector. The stellar density, gas structure, and BN object provide rich data for our analysis and allow extensive testing of the detector in all three observing bands.

We collected M42 data in a series of 40-second exposure ramps between 22:18 ET, December

14, 2023, and 02:30 ET, December 15, 2023. We took four sets of three ramps (each with UTR,5,1,9) with the Trapezium cluster centered in a single quadrant for each observing band. We repeated this for each of the four quadrants, resulting in 48 sets of three ramps.

Figure 4.2 shows a color-composite image of M42 with its corresponding field plot. North is up, and East is left. The image depicts the gaseous structure around the Trapezium cluster and the BN object heating its natal cloud. The photometry for M42 is the least accurate of the three objects presented in this thesis. We attribute this to several factors: (1) the images are composites generated by co-adding all observation data, meaning that data from separate quadrants were co-added - potentially introducing errors not removed during data reduction; (2) the primitive photometry routines (a DAOPHOT derivative for IDL 6.3, implemented without PSF-fitting) are not well-suited to crowded field photometry; and (3) the observing data was contaminated by wispy cloud cover, reducing the measured fluxes from stars by unquantifiable and random amounts. PSF fitting may improve the results, but issue (3) likely still dominates the uncertainties. The photometric measurements of stars in our data largely deviate from the Vizier 2MASS data, with mean deviations of 0.798, 0.949, and 0.763 magnitudes in the J, H, and K bands, respectively.

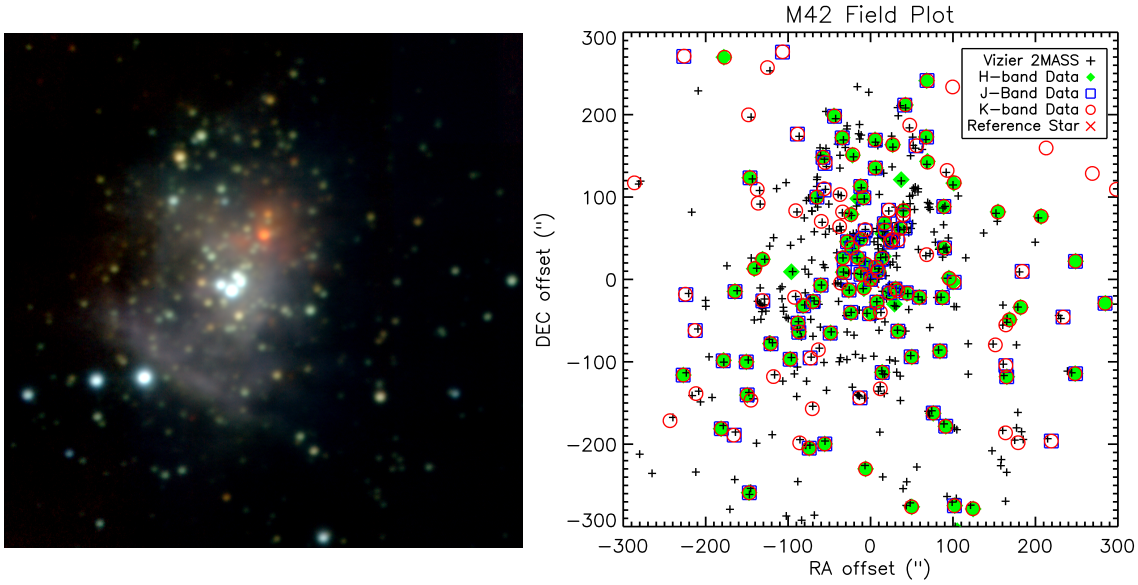


Figure 4.2: The figure on the left presents a color-composite image of M42, stretched to highlight the gas structure. The plot on the right is the field plot, showing the stars identified in each band by our analysis.

## 4.5 M29 Results

In the IR regime, M29 (NGC 6913) is a young and uncrowded open cluster, selected as an object of interest due to the presence of approximately a dozen sparsely positioned bright stars with magnitudes in the range of JHK $\approx$ 6-11. Table 4.2 lists the stars identified in our photometry, along with the magnitudes reported for them in the Vizier 2MASS catalog. Photometry results were normalized to the brightest star in the frame, meaning that we chose a zero-point magnitude to align our photometric measurement with the catalog results. This decision was primarily made because the exposures were short and had low enough fluence to remain in the linear regime of the detector. Star #0 in Table 4.2 is the brightest object in our frame and serves as the reference star.

The data for M29 were collected in a series of 40-second exposure ramps, between 20:07 and 21:45 ET, December 14, 2023. For each observing band, we took four sets of three ramps (each with UTR,5,1,9), resulting in 12 sets of three ramps each.

Figure 4.3 presents a color-composite image of M29, adjacent to its corresponding field

plot. Note the high color variation between stars. Figure 4.4 displays the J-H and J-K color-magnitude diagrams (CMD), which agree remarkably well with the Vizier 2MASS catalog data. Figure 4.5 shows one more CMD, as well as a color-color diagram, comparison to the works of Straižys et al., 2014, 2015 [94, 95]. In Figure 4.4, the stellar main sequence and turn-off stretches top-to-bottom on the left side of the plots, while the non-cluster members have higher color values. Figure 4.6 illustrates the deviations of our photometric results, which are generally within 0.2 magnitudes of the catalog data. The y-axis is the stellar magnitude as listed in the 2MASS database, and the x-axis is the difference between that value and that of our photometry. This is significantly better than the M42 data, for a number of reasons: (1), the stellar field is sparse, allowing ample space for the basic photometry routines to generate accurate measurements of the stars with stellar and inner-outer- sky annuli, without interference from other stars; (2), the stars aren't overwhelmingly bright, and thus the detector response to the light is well within the linear regime of our pixel; (3), as all the exposures kept stars in the same quadrants between exposures, the aforementioned quadrant co-adding effect may not be present; and (4), the data was uncontaminated by cloud cover, resulting in accurate flux measurements. The photometric measurements of stars in our data agree with the Vizier 2MASS data, with mean deviations of 0.046, 0.052, and 0.110 magnitudes in the J, H, and K bands, respectively.

Given the high quality of the M29 photometry, we are able to calculate QE from the data and compare against the in-lab QE experiment. With reasonable assumptions about the transmission of the atmosphere and the reflectivity of the telescope mirrors, we estimate the QE of the detector using Star #0 in Table 4.2 and the following equation,

$$\mathrm{QE_H} = \frac{F_{\mathrm{phot}}}{F_{\mathrm{expected}}} = \frac{\frac{S_{\mathrm{phot}}}{t_{\mathrm{int}}}}{(F_{0,\mathrm{H}} \times 10^{-0.4 m_{\mathrm{H}}})\,(R_{\mathrm{mirr}})^n\,\Delta\lambda_{\mathrm{FWHM}}\,T_{\mathrm{filt}}\,T_{\mathrm{atm}}\,\Delta A} \tag{4.5.1}$$

where $S_{\mathrm{phot}} = 1.26 \times 10^7\,\mathrm{e^-}$ is the total signal from aperture photometry, $t_{\mathrm{int}} = 40\,\mathrm{s}$ is the integration time of the exposure, $F_{0,\mathrm{H}} = 1.138 \times 10^{-9}\,\mathrm{erg/cm^2/s/nm}$ is the Vega zero-point flux for the H-band, $m_{\mathrm{H}} = 6.499$ is the 2MASS H-band magnitude, $\Delta\lambda_{\mathrm{FWHM}} = 291\,\mathrm{nm}$ is the bandpass of the filter, $T_{\mathrm{filt}} = 0.9$ is the average filter transmission, $T_{\mathrm{atm}} = 0.6$ is the

transmission of the atmosphere, $R_{\text{mirr}} = 0.8$ is the reflectivity of the mirror, $n = 2$ is the number of mirrors in the telescope, and $\Delta A = 2,572\,\text{cm}^2$ is the primary mirror area minus the secondary mirror obstruction. When these values are plugged into Equation 4.5.1, we get that $\text{QE}_{\text{H}} = 0.60$, which is exactly the expected QE of 60%. Granted, our value for $R_{\text{mirr}}$ is just a best guess, provided by telescope staff, as the mirrors have not been cleaned or resurfaced in many years. Additionally, $T_{\text{atm}}$ likely varies throughout the total observation time as we track the object across the sky and the amount of atmosphere the starlight passes through changes.

Table 4.2: The table below lists stars identified in our M29 data, the photometric measurements from the Vizier 2MASS catalog, and our photometry results.

| **M29** | | **Vizier 2MASS Catalog** | | | | | **Photometry** | | | | |
|---|---|---|---|---|---|---|---|---|---|---|---|
| # | **2MASS Identifier** | $\mathbf{m}_J$ | $\mathbf{m}_H$ | $\mathbf{m}_K$ | **J-H** | **J-K** | $\mathbf{m}_J$ | $\mathbf{m}_H$ | $\mathbf{m}_K$ | **J-H** | **J-K** |
| 0 | 20235311+3828220 | 7.603 | 6.499 | 6.124 | 1.104 | 1.479 | 7.604 | 6.499 | 6.124 | 1.105 | 1.480 |
| 1 | 20234596+3830033 | 7.133 | 6.734 | 6.323 | 0.399 | 0.810 | 7.055 | 6.690 | 6.282 | 0.365 | 0.773 |
| 2 | 20240466+3832172 | 7.015 | 6.822 | 6.717 | 0.193 | 0.298 | 7.061 | 6.821 | 6.557 | 0.240 | 0.504 |
| 3 | 20240654+3829332 | 7.247 | 7.093 | 6.989 | 0.154 | 0.258 | 7.280 | 7.070 | 6.913 | 0.210 | 0.367 |
| 4 | 20240130+3830496 | 7.344 | 7.178 | 7.100 | 0.166 | 0.244 | 7.361 | 7.151 | 6.897 | 0.210 | 0.464 |
| 5 | 20235100+3829343 | 7.738 | 7.572 | 7.528 | 0.166 | 0.210 | 7.730 | 7.524 | 7.401 | 0.206 | 0.329 |
| 6 | 20235501+3827588 | 7.749 | 7.584 | 7.498 | 0.165 | 0.251 | 7.730 | 7.530 | 7.516 | 0.200 | 0.214 |
| 7 | 20234432+3830430 | 9.803 | 7.704 | 6.773 | 2.099 | 3.030 | 9.712 | 7.641 | 6.719 | 2.071 | 2.993 |
| 8 | 20235906+3829406 | 10.030 | 7.981 | 7.120 | 2.049 | 2.910 | 9.800 | 7.918 | 6.991 | 1.882 | 2.809 |
| 9 | 20234116+3827000 | 9.163 | 8.311 | 7.979 | 0.852 | 1.184 | 9.250 | 8.440 | 8.193 | 0.810 | 1.057 |
| 10 | 20235954+3831479 | 8.637 | 8.488 | 8.441 | 0.149 | 0.196 | 8.680 | 8.475 | 8.221 | 0.205 | 0.459 |
| 11 | 20234594+3831476 | 10.569 | 9.122 | 8.563 | 1.447 | 2.006 | 10.342 | 8.980 | 8.305 | 1.362 | 2.037 |
| 12 | 20240896+3830306 | 10.713 | 9.147 | 8.538 | 1.566 | 2.175 | 10.809 | 9.150 | 8.690 | 1.659 | 2.119 |
| 13 | 20240022+3832445 | 10.702 | 9.209 | 8.597 | 1.493 | 2.105 | 10.741 | 9.163 | 8.305 | 1.578 | 2.436 |
| 14 | 20235507+3829080 | 9.642 | 9.441 | 9.363 | 0.201 | 0.279 | 9.612 | 9.416 | 10.940 | 0.196 | -1.328 |

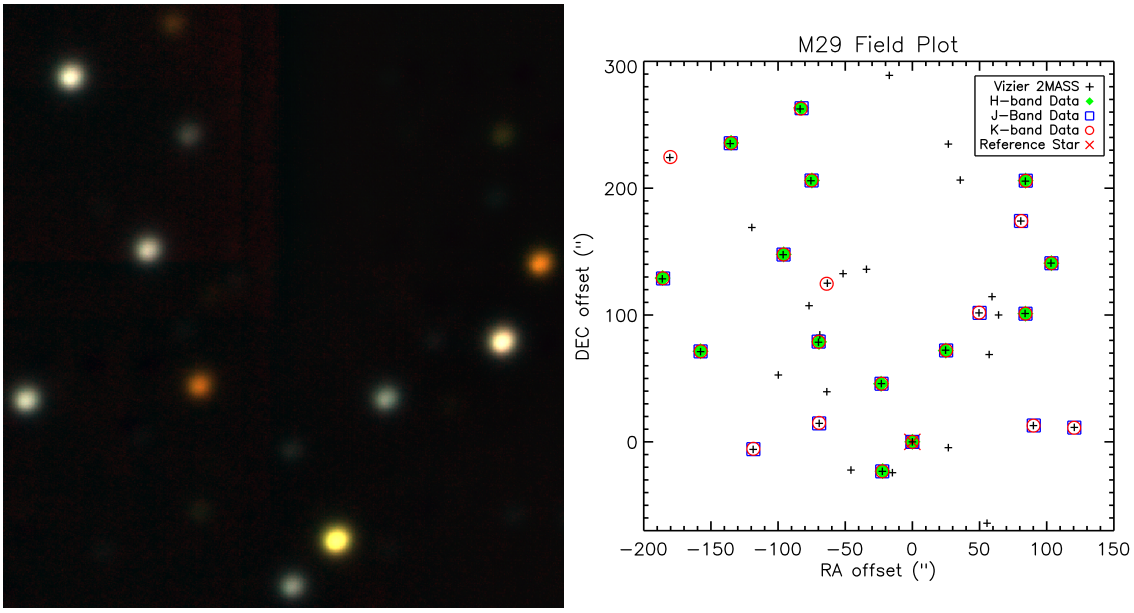


Figure 4.3: The figure on the left shows a color-composite image of the M29 cluster, after processing and stacking. The figure on the right shows a field plot of the M29 cluster. The red cross at (0,0) denotes the bright yellow star in the image, used to align the query with our data.

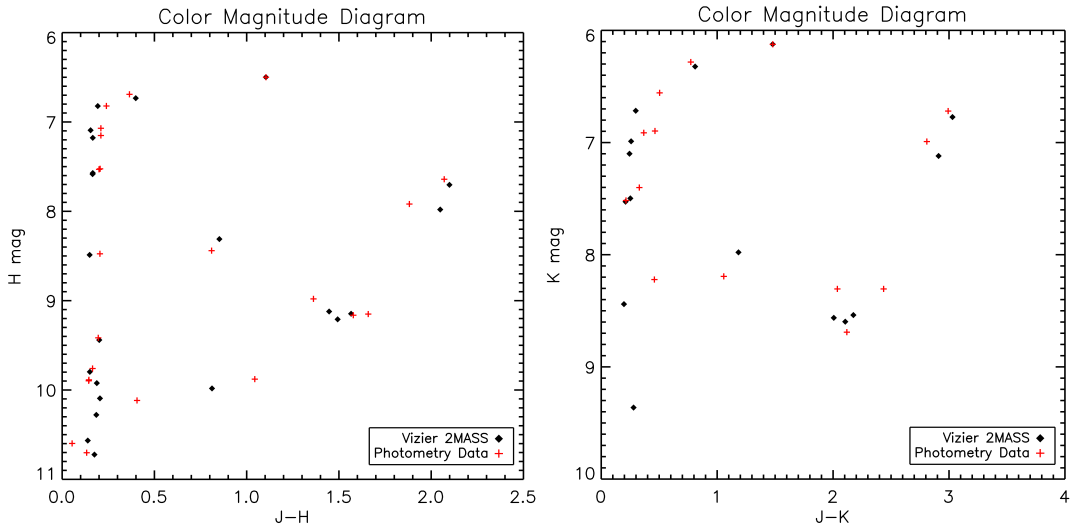


Figure 4.4: This figure shows two color-magnitude diagrams for M29. Note the clustering of the main sequence on the left side of each plot, from top to bottom, and note the turn-off near the top.

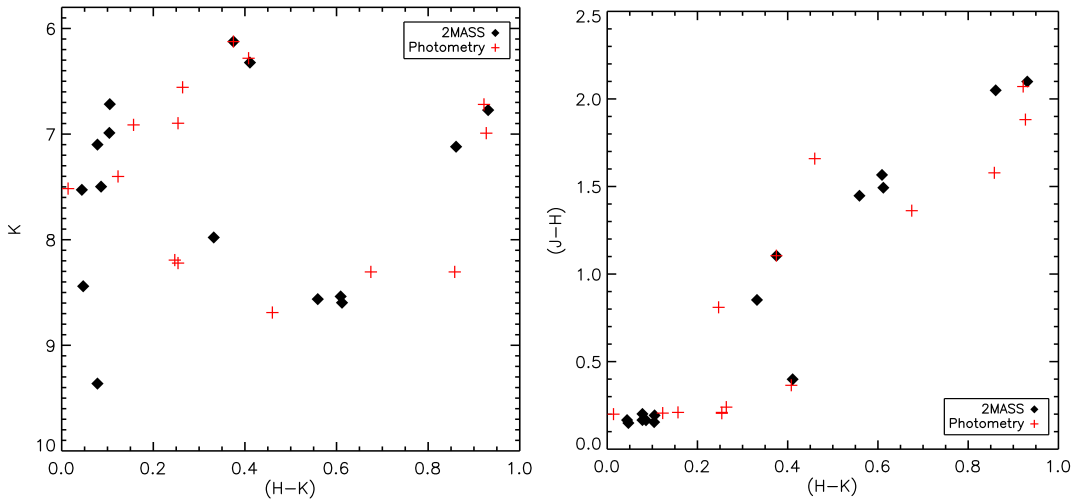


Figure 4.5: This figure shows another color-magnitude and color-color diagram for M29.

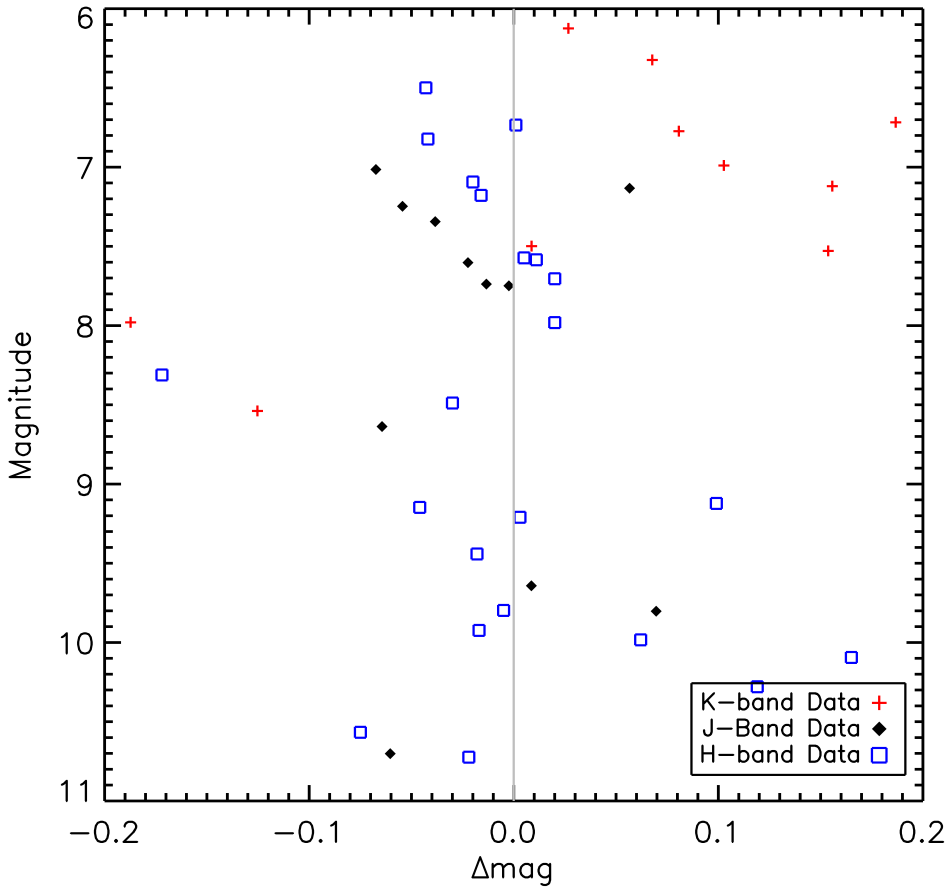


Figure 4.6: This figure shows a Δmagnitude plot of the stars identified in our M29 data. The y-axis represents 2MASS magnitude, while the x-axis is the difference between that value and our photometric measurements.

## 4.6 M37 Results

In the IR regime, M37 (NGC 2099) is a rather crowded open cluster, selected as an object of interest due to the presence of many stars with magnitudes in the range of JHK mag ≈ 6-12. The results were normalized to a star of medium brightness, meaning that a zero-point magnitude was chosen to match our photometric measurement with the catalog results. We choose this star (first star to the top-right of the brightest one in Figure 4.3) because it has sufficiently low fluence to remain in the linear regime of the detector, even over the full duration of the exposure.

The data for M37 were collected in a series of 160-second exposure ramps, between 22:13 ET, December 15, 2023, and 01:32 ET, December 16, 2023. As with M29, we took four sets of three ramps (each with UTR,40,1,3) in each band, resulting in 12 sets of three ramps.

Figure 4.7 presents a color-composite image of M37, adjacent to its corresponding field plot. Figure 4.8 shows the J-H and J-K color-magnitude diagrams (CMD), which show close agreement to the Vizier 2MASS catalog data. Figure 4.9 illustrates the deviations of our photometric results, which are generally within 0.5 magnitudes of the catalog data. The photometric measurements of stars in our data agree with the 2MASS data, with mean deviations of 0.233, 0.269, and 0.383 magnitudes in the J, H, and K bands, respectively. As with M42, the accuracy of the photometry in this cluster was worse than with M29, for the same reasons (high stellar density, primarily).

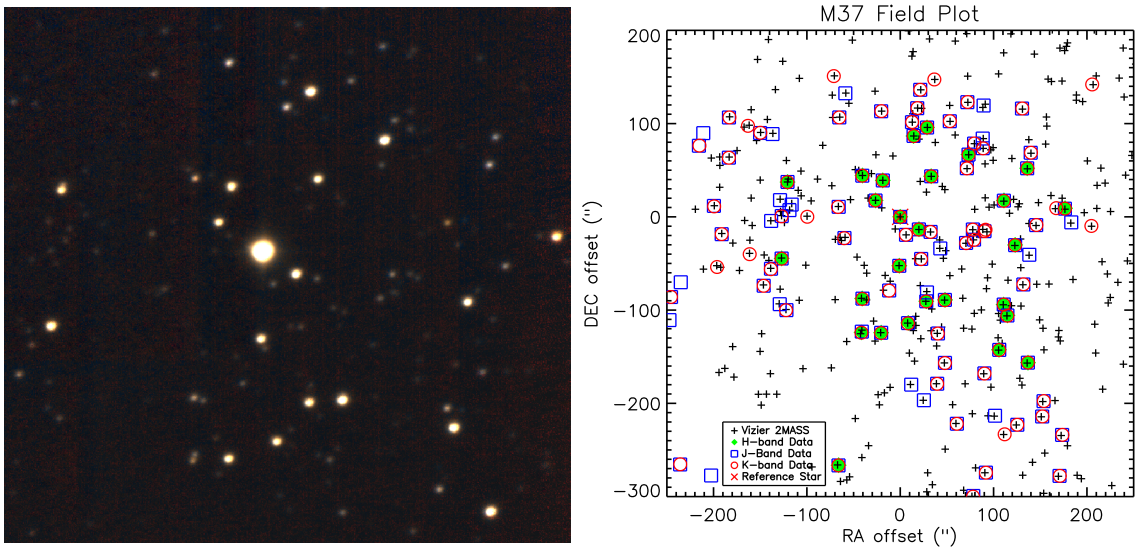


Figure 4.7: The figure on the left shows an H-band image of the M37 cluster, after processing and stacking. The figure on the right shows a field plot of the M37 cluster. The red cross at (0,0) denotes the brightest star in the image, used to align the query with our data.

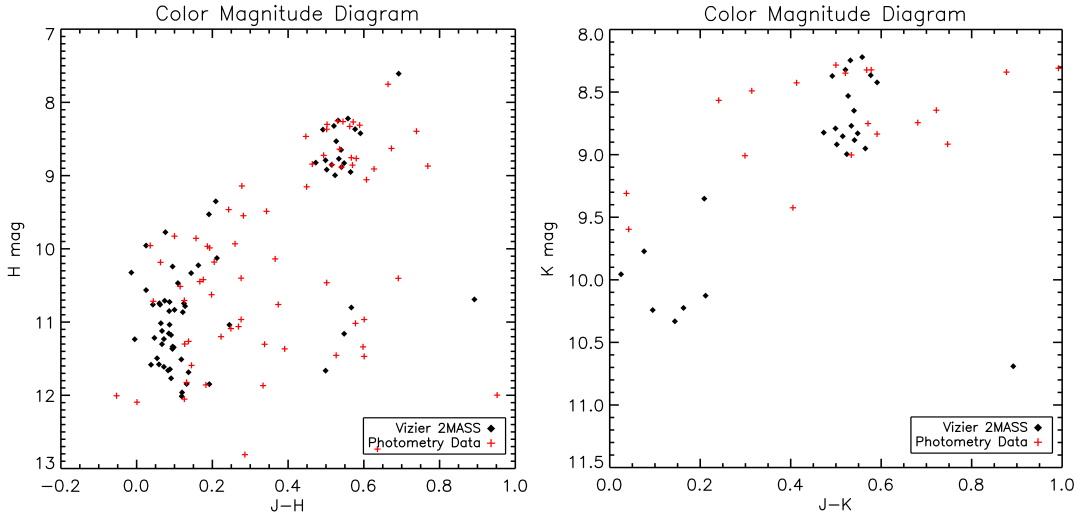


Figure 4.8: This figure shows two color magnitude diagrams for M37.

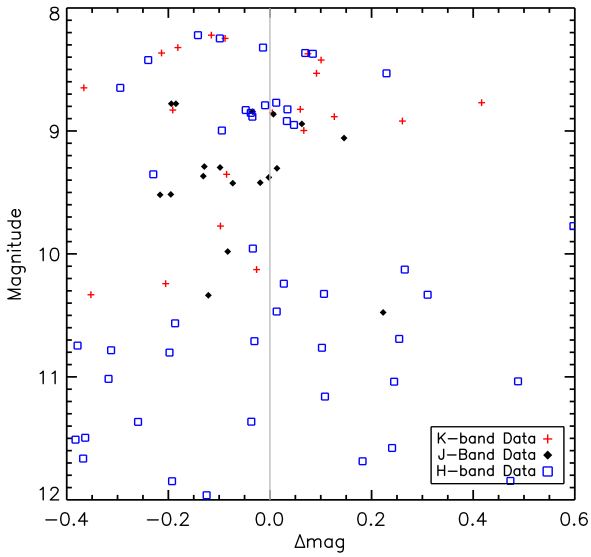


Figure 4.9: This figure shows a Δmagnitude plot of the stars identified in our M37 data.

# Chapter 5

# Summary and Conclusions

In this thesis, progress in the characterization of Raytheon's HgCdTe-on-Si detectors was discussed. Chapter 1 provided a brief history of scientific imaging and an overview of the HgCdTe material and VIRGO ROIC structure. Chapter 2 introduced the operating principles of the photodiode p-n junction and its features, including dark current and persistence mechanisms. Chapter 3 presented the results of my efforts to characterize dark current and persistence effects in the SATIN detectors, including brief discussions of crosstalk and pixel linearity. Chapter 4 presents the results of an observing run carried out with V23.

The dark current for the best pixels in the detector are shown to be more than an order of magnitude lower than the quadrant median published in previous works. The measured dark current is found to be limited by multiplexer glow. By analyzing the contributions from multiplexer glow and dark current mechanisms, the dark current floor has been isolated and modeled as a function of temperature and sampling frequency. Persistence measurements have revealed a broad spectrum of charge-trapping timescales, spanning many orders of magnitude, with trapping occurring predominantly in the depletion region. A correlation has been established between p-n junction implant area and both elevated dark current and defective-pixel fraction, attributable to increased defect density within the active volume. These findings provide valuable insights into the limitations and potential improvements for MCT-on-Si technology.

The dark current analysis has shown that the median measured dark current in the selected pixel population is approximately 0.0036 electrons per second at cryogenic temperatures - approximately twice that of the detectors used for the WFIRST array - and an order of magnitude lower than previously believed [32, 33]. Multiplexer glow is shown to contribute a significant fraction of this measured dark current even when extremely sparse sampling is used, and thus the most promising avenue for dark current reduction is ROIC development. Introduction of appropriate shielding structures and metal layers to block the edge glow and prevent in-pixel glow from contaminating the data would provide significant further reduction of the noise, bringing these detectors in line with the current state-of-the-art and allowing more accurate assessment of the contributions from true dark current mechanisms.

The only contributor to the dark current floor (of the true dark current mechanisms) is trap-assisted-tunneling, which more advanced defect reduction techniques may be able to mitigate. Of particular note is passivation of dislocation defects within the detector bulk, demonstrated by Boieriu in 2013. This method exposes HgCdTe detector substrate during MBE growth to a hydrogen plasma, which is shown to significantly reduce non-uniformity and lower dark current [8, 96]. Reducing the number of active defects within the pixels would also allow for larger junction implants, as fewer active defects would intersect the active pixel area. This would relax the requirements on future ROIC development, particularly with regard to mitigating the effects of non-linearity.

Persistence characterization has quantified the trap populations by their charge-release timescales. The excess charge observed in light illuminated versus bias manipulated measurements demonstrates that optical illumination likely accesses traps outside the nominal depletion region that bias manipulation alone cannot populate. Cross-sections through persistence images at fixed times after reset confirm linear growth of trapped charge with fluence, implying trap occupancy scales directly with integrated illumination, and that the traps are evenly distributed throughout the depletion region. We conclude that most of the traps are within the depletion region, and likely near the passivated frontside surface, given the morphology of the persistence behavior. It is possible that advanced passivation methods, such as the

one discussed above for dark current, would reduce the persistence in MCT-on-Si detectors.

Interpixel crosstalk is approximately 0.2%, an order of magnitude lower than reported for the WFIRST 10 $\mu$m-pitch H4RG-10 detectors, attributable, in part, to the larger 20 $\mu$m pitch and reduced carrier lifetimes in the defective MCT-on-Si material. Unfortunately, this low crosstalk is likely to rise as improvements to the MCT-on-Si process are made, since purer materials will increase carrier lifetimes and better processes will lower pixel size. That said, even if a significant increase in crosstalk occurs, it is unlikely that these devices will exceed what is acceptable for state-of-the-art science devices.

Linearity is shown to depend strongly on the size of the junction implant, and underscores the importance of bespoke ROIC development in tandem with detector design. The linearity issues arise from complications regarding the sources of capacitance within the ROIC and how they interact with the capacitance of the junction in determining pixel response. As with dark current, the largest improvements in this metric will come from ROIC development, and aligning the design parameters for the ROIC with that of the desired detector.

The on-sky observations obtained with the SATIN detectors validate the laboratory characterization. Despite the elevated dark current and persistence relative to CZT devices, the arrays produce usable astronomical images with acceptable noise performance after appropriate image processing, despite sub-par telescope equipment and observing conditions.

The results presented in this thesis indicate that MCT-on-Si detectors have the potential to become competitive with current state-of-the-art detectors, provided that the epitaxial growth process is improved and the arrays are hybridized to a more advanced ROIC. If the defect density can be reduced to $\leq 10^5\,\mathrm{cm}^{-2}$, a critical barrier to lowering dark current and achieving high operability will have been overcome. Even if defect density cannot reach that threshold, bulk passivation methods may be able to significantly mitigate the number of defects that meaningfully impact detector performance. Although the use of small-pixel junction implants has proven effective in improving operability, further development of the ROIC architecture will be required to ensure that pixel linearity is not degraded by parasitic capacitance effects.

# Bibliography

[1] Brandon J. Hanold, Donald F. Figer, Joong Lee, Kimberly Kolb, Iain Marcuson, Elizabeth Corrales, Jonathan Getty, and Lynn Mears. Large format MBE HgCdTe on silicon detector development for astronomy. In Paul D. LeVan, Ashok K. Sood, Priyalal Wijewarnasuriya, and Arvind I. D'Souza, editors, *Infrared Sensors, Devices, and Applications V*, volume 9609, page 96090Y. International Society for Optics and Photonics, SPIE, 2015. (document), 1.3.1, 1.3.1, 1.2, 1.3.2

[2] Brian Hayden and Suzanne Villeneuve. Astronomy in the upper palaeolithic? *Cambridge Archaeological Journal*, 21(3):331–355, 2011. 1

[3] W. S. Boyle and G. E. Smith. Charge coupled semiconductor devices (Bell System Technical Journal 1970). In A. Mampaso, M. Prieto, and F. Sánchez, editors, *Selected Papers on Instrumentation in Astronomy*, page 475. 1993. 1.1

[4] A. Rogalski. *Infrared Detectors*. Infrared Detectors. CRC Press, 2020. 1.2, 1.3, 1.3.2, 2.1.4

[5] Matthew J. Penn. Infrared solar physics. *Living Reviews in Solar Physics*, 11, May 2014. 1.2

[6] Scott M. Johnson, William A. Radford, Aimee A. Buell, Mauro F. Vilela, Jeffrey M. Peterson, Jeffrey J. Franklin, Richard E. Bornfreund, Alexander C. Childs, Gregory M. Venzor, Michael D. Newton, Edward P. G. Smith, Lee M. Ruzicka, Gregory K. Pierce, Daniel D. Lofgreen, Terence J. de Lyon, and John E. Jensen. Status of HgCdTe/Si

technology for large format infrared focal plane arrays. In Manijeh Razeghi and Gail J. Brown, editors, *Quantum Sensing and Nanophotonic Devices II*, volume 5732, pages 250–258. International Society for Optics and Photonics, SPIE, 2005. 1.3.1

[7] M. Vaghayenegar, R. N. Jacobs, J. D. Benson, A. J. Stoltz, L. A. Almeida, and David J. Smith. Correlation of etch pits and dislocations in as-grown and thermal cycle-annealed hgcdte(211) films. *Journal of Electronic Materials*, 46(8):5007–5019, Apr 2017. 1.3.1

[8] Wen Lei, Jarek Antoszewski, and Lorenzo Faraone. Progress, challenges, and opportunities for hgcdte infrared materials and detectors. *Applied Physics Reviews*, 2(4):041303, 12 2015. 1.3.1, 1.3.3, 2.1.4, 2.3.2, 3.3.4, 5

[9] Richard E. Bornfreund, Peter J. Love, Alan W. Hoffman, Ken J. Ando, Elizabeth Corrales, William D. Ritchie, Neil J. Therrien, Joe P. Rosbeck, Aimee Buell, Jeffrey Peterson, Jeffrey Franklin, Mauro Vilela, J. Bangs, Scott M. Johnson, and William Radford. Large format short-wave hgcdte detectors and focal plane arrays. 2015. 1.3.1, 1.3, 3.4.3

[10] Donald Figer, Joong Lee, Elizabeth Corrales, Jonathan Getty, and Lynn Mears. HgCdTe detectors grown on silicon substrates for observational astronomy. In Andrew D. Holland and James Beletic, editors, *High Energy, Optical, and Infrared Detectors for Astronomy VIII*, volume 10709, page 1070926. International Society for Optics and Photonics, SPIE, 2018. 1.3.1

[11] A. Rogalski, K. Adamiec, and J. Rutkowski. *Narrow-gap Semiconductor Photodiodes.* SPIE, 2000. 1.3.1

[12] S. M. Johnson, D. R. Rhiger, J. P. Rosbeck, J. M. Peterson, S. M. Taylor, and M. E. Boyd. Effect of dislocations on the electrical and optical properties of long-wavelength infrared HgCdTe photovoltaic detectors. *Journal of Vacuum Science Technology B: Microelectronics and Nanometer Structures*, 10(4):1499–1506, July 1992. 1.3.1

[13] K. Jóźwikowski, A. Jóźwikowska, M. Kopytko, A. Rogalski, and L.R. Jaroszewicz. Dislocations as a noise source in lwir hgcdte photodiodes. *Journal of Electronic Materials*, 45:4769–4781, 2016. 1.3.1, 1.3.2, 2.1.4, 3.4.1

[14] K. Jóźwikowski, A. Jóźwikowska, M. Kopytko, A. Rogalski, and L.R. Jaroszewicz. Simplified model of dislocations as a srh recombination channel in the hgcdte heterostructures. *Infrared Physics and Technology*, 55(1):98–107, 2012. 1.3.2, 2.1.4, 3.4.1, 3.5

[15] A. Rogalski. HgCdTe infrared detector material: history, status and outlook. *Reports on Progress in Physics*, 68(10):2267–2336, October 2005. 1.3.2, 2.1.1

[16] Roger M. Smith, Maximilian Zavodny, Gustavo Rahmer, and Marco Bonati. A theory for image persistence in HgCdTe photodiodes. In David A. Dorn and Andrew D. Holland, editors, *High Energy, Optical, and Infrared Detectors for Astronomy III*, volume 7021, page 70210J. International Society for Optics and Photonics, SPIE, 2008. 1.3.2, 2.3.1

[17] W. E. Tennant, J. M. Arias, and J. Bajaj. HgCdTe at Teledyne. In Bjørn F. Andresen, Gabor F. Fulop, and Paul R. Norton, editors, *Infrared Technology and Applications XXXV*, volume 7298, page 72982V. International Society for Optics and Photonics, SPIE, 2009. 1.3

[18] G. L. Hansen, J. L. Schmit, and T. N. Casselman. Energy gap versus alloy composition and temperature in Hg/1-x/Cd/x/Te. *Journal of Applied Physics*, 53:7099–7101, October 1982. 1.4.1, 2.1.1, 2.2.2

[19] Thibault Pichon and Luc Boucher. Pixel source follower glow in HxRG detector. *Astronomische Nachrichten*, 344:e20230102, October 2023. 1.4.2, 2.2.5, 3.4.2, 3.4.3, 3.4.7

[20] Michael W. Regan and Louis E. Bergeron. Zero dark current in H2RG detectors: it is all multiplexer glow. *Journal of Astronomical Telescopes, Instruments, and Systems*, 6:016001, January 2020. 1.5.2, 3.4.2, 3.4.3, 3.4.3, 3.4.7

[21] Gregory Mosby, Bernard J. Rauscher, Chris Bennett, Edward S. Cheng, Stephanie Cheung, Analia Cillis, David Content, Dave Cottingham, Roger Foltz, John Gygax, Robert J.

Hill, Jeffrey W. Kruk, Jon Mah, Lane Meier, Chris Merchant, Laddawan Miko, Eric C. Piquette, Augustyn Waczynski, and Yiting Wen. Properties and characteristics of the nancy grace roman space telescope h4rg-10 detectors. *Journal of Astronomical Telescopes, Instruments, and Systems*, 6(04), November 2020. 1.5.2, 2.3.2

[22] Ben G. Streetman and Sanjay Banerjee. *Solid state electronic devices*. Pearson/Prentice Hall, Upper Saddle River, N.J, 6th edition, 2006. 2.1.1, 2.1.1, 2.2.1

[23] M.B. Reine, A.K. Sood, and T.J. Tredwell. Chapter 6 photovoltaic infrared detectors. In R.K. Willardson and Albert C. Beer, editors, *Mercury Cadmium Telluride*, volume 18 of *Semiconductors and Semimetals*, pages 201–311. Elsevier, 1981. 2.1.1

[24] M.A. Kinch. *State-of-the-Art Infrared Detector Technology*. SPIE, 2014. 2.1.1, 2.2.2, 2.2.3

[25] S.M. Sze. *p-n Junctions*, pages 77–133. John Wiley & Sons, Ltd, 2006. 2.1.1, 2.2.3

[26] Chenming Hu. *Modern semiconductor devices for integrated circuits*. Prentice Hall, Upper Saddle River, N.J, 2010. 2.1.1, 2.2.1

[27] M. Kopytko and A. Rogalski. New insights into the ultimate performance of hgcdte photodiodes. *Sensors and Actuators A: Physical*, 339:113511, 2022. 2.1.1

[28] Ralf Dornhaus, Günter Nimtz, and B. Schlicht. Narrow-gap semiconductors. 1983. 2.1.1

[29] A. A. Plazas, C. Shapiro, R. Smith, E. Huff, and J. Rhodes. Laboratory Measurement of the Brighter-fatter Effect in an H2RG Infrared Detector. PASP, 130(988):065004, June 2018. 2.1.2

[30] Gregory Mosby Jr., Nathan Eggen, Marsha Wolf, Kurt Jaehnig, and Ralf Kotulla. Persistence characterization and data calibration scheme for the RSS-NIR H2RG detector on SALT. In Andrew D. Holland and James Beletic, editors, *High Energy, Optical, and Infrared Detectors for Astronomy VII*, volume 9915, page 99152U. International Society for Optics and Photonics, SPIE, 2016. 2.1.2, 2.3, 2.3.2

[31] Gregory Mosby, Bernard J. Rauscher, Chris Bennett, Edward S. Cheng, Stephanie Cheung, Analia Cillis, David Content, Dave Cottingham, Roger Foltz, John Gygax, Robert J. Hill, Jeffrey W. Kruk, Jon Mah, Lane Meier, Chris Merchant, Laddawan Miko, Eric C. Piquette, Augustyn Waczynski, and Yiting Wen. Properties and characteristics of the Nancy Grace Roman Space Telescope H4RG-10 detectors. *Journal of Astronomical Telescopes, Instruments, and Systems*, 6:046001, October 2020. 2.1.2, 2.3, 2.3.2, 3.3.3, 3.5, 3.5, 3.5.1

[32] Gregory Mosby, Bob Hill, Analia Cillis, Roger Foltz, Chris Bennett, Mario Cabrera, Michael Hickey, Chris Merchant, Augustyn Waczynski, Yiting Wen, Bernie Rauscher, Edward J. Wollack, Jeff Kruk, John Auyeung, Joshua Schlieder, Eric Switzer, Maxime Rizzo, Neil Zimmerman, Edward Cheng, Craig Cabelli, Eric Piquette, Jianmei Pan, Mark Farris, Anders Petersen, John Gygax, Colin Stuart, Dave Cottingham, Jonathan Mah, Stephanie Cheung, Lane Meier, Daniel Kelly, and Steven Mann. Summary of the Nancy Grace Roman Space Telescope flight detector performance. *Journal of Astronomical Telescopes, Instruments, and Systems*, 11:011210, January 2025. 2.1.2, 2.3, 3.4.6.1, 3.5, 3.5.1, 5

[33] Donald F. Figer, Justin Gallagher, Lazar Buntic, Jonathan Getty, and Stefan Lauxtermann. The SATIN infrared detector development program and the road to HELLSTAR. In Andrew D. Holland and James Beletic, editors, *X-Ray, Optical, and Infrared Detectors for Astronomy X*, volume 12191 of *Society of Photo-Optical Instrumentation Engineers (SPIE) Conference Series*, page 121910P, August 2022. 2.1.2, 3.4.7, 3.5.1, 5

[34] Fei Wang. *Linearity Research of a CMOS Image Sensor*. PhD thesis, Delft University of Technology, Delft, The Netherlands, October 2018. 2.1.2, 3.6

[35] Beatriz Blanco Filgueira. *Modelling and Characterization of Small Photosensors in Advanced CMOS Technologies*. Phd thesis, Universidade de Santiago de Compostela, Santiago de Compostela, Spain, 2012. 2.1.2, 3.6

[36] Konstantin D Stefanov. *CMOS Image Sensors*. 2053-2563. IOP Publishing, 2022. 2.1.3

[37] Majid Zandian. Rule-22: An Update to Rule-07. *Journal of Electronic Materials*, 52(11):7095–7102, November 2023. 2.2, 2.2.5

[38] Rory Bowens, Michael R. Meyer, Taylor L. Tobin, Eric Viges, Dennis Hart, John Monnier, Jarron Leisenring, Derek Ives, and Roy van Boekel. Characterization of a longwave HgCdTe GeoSnap detector. In Andrew D. Holland and Kyriaki Minoglou, editors, *X-Ray, Optical, and Infrared Detectors for Astronomy XI*, volume 13103, page 1310325. International Society for Optics and Photonics, SPIE, 2024. 2.2

[39] Candice Marie Bacon. *Development of long wave infrared detectors for space astronomy.* PhD thesis, University of Rochester, New York, January 2006. 2.2.1, 2.2.2, 2.2.4, 3.5

[40] James Janesick, James Andrews, John Tower, Mark Grygon, Tom Elliott, John Cheng, Michael Lesser, and Jeff Pinter. Fundamental performance differences between CMOS and CCD imagers: Part II. In Thomas J. Grycewicz, Cheryl J. Marshall, and Penny G. Warren, editors, *Focal Plane Arrays for Space Telescopes III*, volume 6690 of *Society of Photo-Optical Instrumentation Engineers (SPIE) Conference Series*, page 669003, September 2007. 2.2.1

[41] Chih-tang Sah, Robert N. Noyce, and William Shockley. Carrier generation and recombination in p-n junctions and p-n junction characteristics. *Proceedings of the IRE*, 45(9):1228–1243, 1957. 2.2.2, 2.2.2

[42] Mario Salvador Cabrera. *Development of 15 μm cutoff wavelength HgCdTe detector arrays for astronomy.* PhD thesis, University of Rochester, New York, January 2020. 2.2.2, 2.2.3

[43] M. A. Kinch. Chapter 7 metal-insulator-semiconductor infrared detectors. In R.K. Willardson and Albert C. Beer, editors, *Mercury Cadmium Telluride*, volume 18 of *Semiconductors and Semimetals*, pages 313–378. Elsevier, 1981. 2.2.3

[44] W. E. Tennant, Donald Lee, Majid Zandian, Eric Piquette, and Michael Carmody. MBE HgCdTe Technology: A Very General Solution to IR Detection, Described by "Rule 07", a

Very Convenient Heuristic. *Journal of Electronic Materials*, 37(9):1406–1410, September 2008. 2.2.5

[45] Guillaume Huber, Michael Bottom, Charles-Antoine Claveau, Shane Jacobson, Matthew Newland, Ian Baker, Keith Barnes, and Matthew Hicks. Glow reduction of ultra-low noise LmAPDs: towards photon counting infrared arrays. In Andrew D. Holland and Kyriaki Minoglou, editors, *X-Ray, Optical, and Infrared Detectors for Astronomy XI*, volume 13103 of *Society of Photo-Optical Instrumentation Engineers (SPIE) Conference Series*, page 1310320, August 2024. 2.2.5

[46] Ian Baker, Matthew Hicks, Chris Maxey, and Daniel Owton. Leonardo UK high performance shortwave APDs for astronomy. In Priyalal Wijewarnasuriya, Arvind I. D'Souza, and Ashok K. Sood, editors, *Infrared Sensors, Devices, and Applications XIII*, volume 12687, page 1268702. International Society for Optics and Photonics, SPIE, 2023. 2.2.5

[47] James W. Beletic, Richard Blank, David Gulbransen, Donald Lee, Markus Loose, Eric C. Piquette, Thomas Sprafke, William E. Tennant, Majid Zandian, and Joseph Zino. Teledyne Imaging Sensors: infrared imaging technologies for astronomy and civil space. In David A. Dorn and Andrew D. Holland, editors, *High Energy, Optical, and Infrared Detectors for Astronomy III*, volume 7021, page 70210H. International Society for Optics and Photonics, SPIE, 2008. 2.2.5

[48] Jarron M. Leisenring, Marcia Rieke, Karl Misselt, and Massimo Robberto. Characterizing persistence in JWST NIRCam flight detectors. In Andrew D. Holland and James Beletic, editors, *High Energy, Optical, and Infrared Detectors for Astronomy VII*, volume 9915 of *Society of Photo-Optical Instrumentation Engineers (SPIE) Conference Series*, page 99152N, August 2016. 2.3, 2.3.2

[49] Derek Ives, Domingo Alvarez, Naidu Bezawada, Elizabeth George, and Benoit Serra. Characterisation, performance and operational aspects of the H4RG-15 near infrared detectors for the MOONS instrument. In Andrew D. Holland and James Beletic, editors, *X-Ray, Optical, and Infrared Detectors for Astronomy IX*, volume 11454 of *Society of*

*Photo-Optical Instrumentation Engineers (SPIE) Conference Series*, page 114541N, December 2020. 2.3, 2.3.2, 3.3.4, 3.4.2

[50] Bogna Kubik, Remi Barbier, Gerard Smadja, Sylvain Ferriol, Simon Conseil, Yannick Copin, William Gillard, Stefano Dusini, Knud Jahnke, Eric Prieto, Natalia Auricchio, Evandro Balbi, Andrea Balestra, Paola Battaglia, Vito Capobianco, Ranga Chary, Leonardo Corcione, Fabrizio Cogato, Gaia Delucchi, Enrico Franceschi, Louis Gabarra, Fluvio Gianotti, Frank Grupp, Elisa Lentini, Sebastiano Ligori, Eduardo Medinaceli, Gianluca Morgante, Kerry Paterson, Erik Romelli, Lucas Sauniere, Mischa Schirmer, Chiara Sirignano, Gemma Testera, Massimo Trifoglio, Antonino Troja, Luca Valenziano, Marco Frailis, Marco Scodeggio, Jean-Christophe Barriere, Michel Berthé, Christof Bodendorf, Amandine Caillat, Michael Carle, Ricard Casas, Hyung Cho, Anne Costille, Franck Ducret, Bianca Garilli, Warren Holmes, Felix Hormuth, Allan Hornstrup, Murzy Jhabvala, Ralf Kohley, David Le Mignant, Per B. Lilje, Ivan Lloro, Cristobal Padilla, Gianluca Polenta, Jean-Christophe Salvignol, Gregor Seidel, Benoit Serra, Aurélia Secroun, Luca Stanco, R. Toledo-Moreo, Stefano Anselmi, Enrico Borsato, Laurence Caillat, Carlos Colodro-Conde, Vito Conforti, James Davies, Alessandro Renzi, Flavio Dal Corso, Stefano Davini, Adriano Derosa, José Javier Diaz, Sergio Di Domizio, Donato Di Ferdinando, Ruben Farinelli, Angelo Giuseppe Ferrari, Federico Fornari, Francesco Giacomini, Oliver Krause, Fulvio Laudisio, Juan Macias-Perez, Julien Marpaud, Nicoletta Mauri, Ronaldo da Silva, Mathieu Niclas, Francesca Passalacqua, Ilaria Risso, P. Lagier, A. N. Sorensen, Patrick Stassi, Jörg Steinwagner, Matteo Tenti, Cedric Thizy, Silvano Tosi, Riccardo Travaglini, Oscar Tubio Araujo, Claudia Valieri, Sandro Ventura, Christophe Vescovi, and Julien Zoubian. Performance of the image persistence model for euclid infrared detectors. In Andrew D. Holland and Kyriaki Minoglou, editors, *X-Ray, Optical, and Infrared Detectors for Astronomy XI*, page 63. SPIE, 2024. 2.3

[51] Roger M. Smith, Maximilian Zavodny, Gustavo Rahmer, and Marco Bonati. Calibration of image persistence in HgCdTe photodiodes. In David A. Dorn and Andrew D. Holland, editors, *High Energy, Optical, and Infrared Detectors for Astronomy III*, volume 7021

of *Society of Photo-Optical Instrumentation Engineers (SPIE) Conference Series*, page 70210K, July 2008. 2.3.1

[52] Simon Tulloch. Persistence Characterisation of teledyne H2RG detectors. *arXiv e-prints*, page arXiv:1807.05217, July 2018. 2.3.2, 3.3.3

[53] Simon Tulloch, Elizabeth George, and ESO Detector Systems Group. Predictive model of persistence in H2RG detectors. *Journal of Astronomical Telescopes, Instruments, and Systems*, 5:036004, July 2019. 2.3.2, 3.3.3

[54] T. Le Goff, T. Pichon, N. Baier, O. Gravrand, and O. Boulade. Model and Characterization of Persistence in HgCdTe SWIR Detectors for Astronomy Application. *Journal of Electronic Materials*, 51(10):5586–5593, October 2022. 2.3.2

[55] Steven L. Solomon. *Near Infrared Spectroscopic Imaging of NGC 7023 and Charge Trapping in InSb Photodiode Arrays.* PhD thesis, University of Rochester, New York, 1998. 2.3.2

[56] David R. Rhiger and Jamal I. Mustafa. The electron affinity of hgcdte. *Journal of Applied Physics*, 138(16):165701, 10 2025. 2.3.2

[57] Anjali, P. Srivastava, S. Mohapatra, H. P. Lenka, R. Pal, H. P. Vyas, B. R. Sekhar, and H. K. Sehgal. RBS study of annealing effects in passivated mercury cadmium telluride. *Semiconductor Science Technology*, 20(10):1072–1077, October 2005. 2.3.2

[58] Ragini Raj Singh, Diksha Kaushik, Dhirendra Gupta, R.K. Sharma, and R.K. Pandey. Investigation of passivation processes for hgcdte/cds structure for infrared application. *Thin Solid Films*, 510(1):235–240, 2006. 2.3.2

[59] John Robertson, Xuewei Zhang, Qingzhong Gui, and Yuzheng Guo. Amorphous teo2 as p-type oxide semiconductor for device applications. *Applied Physics Letters*, 124(21):212101, 05 2024. 2.3.2

[60] Rachel E. Anderson, Michael Regan, Jeff Valenti, and Eddie Bergeron. Understanding Persistence: A 3D Trap Map of an H2RG Imaging Sensor. *arXiv e-prints*, page arXiv:1402.4181, February 2014. 3.3.3

[61] Candice M. Bacon, Craig W. McMurtry, Judith L. Pipher, Amanda Mainzer, and William Forrest. Effect of dislocations on dark current in LWIR HgCdTe photodiodes. In Andrew D. Holland and David A. Dorn, editors, *High Energy, Optical, and Infrared Detectors for Astronomy IV*, volume 7742, page 77421U. International Society for Optics and Photonics, SPIE, 2010. 3.4.1, 3.5

[62] Antoni Rogalski. Infrared detectors: status and trends. *Progress in Quantum Electronics*, 27(2):59–210, 2003. 3.4.1

[63] B. S. Chaudhari, H. Goto, M. Niraula, and K. Yasuda. Analysis of dislocations and their correlation with dark currents in cdte/si heterojunction diode-type x-ray detectors. *Journal of Applied Physics*, 130(5):055302, 08 2021. 3.4.1

[64] Olivier Boulade, Vincent Moreau, Patrick Mulet, Olivier Gravrand, Cyril Cervera, Jean-Paul Zanatta, Pierre Castelein, Fabrice Guellec, Bruno Fièque, Philippe Chorier, and Julien Roumegoux. Development activities on NIR large format MCT detectors for astrophysics and space science at CEA and SOFRADIR. In Andrew D. Holland and James Beletic, editors, *High Energy, Optical, and Infrared Detectors for Astronomy VII*, volume 9915 of *Society of Photo-Optical Instrumentation Engineers (SPIE) Conference Series*, page 99150C, July 2016. 3.4.2, 3.4.3

[65] Naidu Bezawada, Derek Ives, Elizabeth George, Domingo Alvarez, Benoit Serra, Mark Farris, Anders Petersen, and Liz Corrales. Output buffer glow and its mitigation in H4RG-15 detectors. *Journal of Astronomical Telescopes, Instruments, and Systems*, 10(2):026007, 2024. 3.4.2, 3.4.4

[66] K. Lehovec, C. A. Accardo, and E. Jamgochian. Injected Light Emission of Silicon Carbide Crystals. *Physical Review*, 83(3):603–607, August 1951. 3.4.2

[67] E. Fred Schubert. *Light-Emitting Diodes (2nd Edition)*. Cambridge University Press, 2006. 3.4.2

[68] S. Tam and Chenming Hu. Hot-electron-induced photon and photocarrier generation in silicon mosfet's. *IEEE Transactions on Electron Devices*, 31(9):1264–1273, 1984. 3.4.2

[69] Jeff Bude, Nobuyuki Sano, and Akira Yoshii. Hot-carrier luminescence in Si. *Physical Review B*, 45(11):5848–5856, March 1992. 3.4.2

[70] L Carbone, R Brunetti, C Jacoboni, A Lacaita, and M Fischetti. Polarization analysis of hot-carrier light emission in silicon. *Semiconductor Science and Technology*, 9(5S):674, may 1994. 3.4.2

[71] Franco Stellari, F. Zappa, S. Cova, and L. Vendrame. Tools for non-invasive optical characterization of cmos circuits. pages 487 – 490, 02 1999. 3.4.2

[72] Stephan Maestre, Pierre Magnan, Francis Lavernhe, and Franck Corbiere. Hot carriers effects and electroluminescence in the CMOS photodiode active pixel sensors. In Nitin Sampat, Ricardo J. Motta, Morley M. Blouke, Nitin Sampat, and Ricardo J. Motta, editors, *Sensors and Camera Systems for Scientific, Industrial, and Digital Photography Applications IV*, volume 5017, pages 59 – 67. International Society for Optics and Photonics, SPIE, 2003. 3.4.2, 3.4.3

[73] JMCE Jon Clarke. private communication. 3.4.3

[74] Karl Pearson. The Problem of the Random Walk. Nature, 72(1865):294, July 1905. 3.5

[75] Rachel P. Dudik, Margaret E. Jordan, Bryan N. Dorland, Daniel Veillette, Augustyn Waczynski, Benjamin F. Lane, Markus Loose, Emily Kan, James Waterman, Chris Rollins, and Steve Pravdo. Interpixel crosstalk in teledyne imaging sensors h4rg-10 detectors. *Applied Optics*, 51(15):2877, May 2012. 3.5

[76] Bernard J. Rauscher, David Alexander, Clifford K. Brambora, Meng Chiao, Brian L. Clemons, Rebecca Derro, Charles Engler, Ori Fox, Matthew B. Garrison, Matthew A.

Greenhouse, Greg Henegar, Robert J. Hill, Thomas Johnson, Rodolfo J. Lavaque, Don J. Lindler, Sridhar S. Manthripragada, Cheryl Marshall, Brent Mott, Thomas M. Parr, Wayne D. Roher, Kamdin B. Shakoorzadeh, Miles Smith, Augustyn Waczynski, Yiting Wen, Donna Wilson, Mary Ballard, Craig Cabelli, Edward Cheng, James Garnett, Elliott Koch, Markus Loose, Majid Zandian, Joseph Zino, Timothy Ellis, Bryan Howe, Miriam Jurado, Ginn Lee, John Nieznanski, Peter Wallis, James York, Michael W. Regan, Giorgio Bagnasco, Torsten Böker, Guido De Marchi, Pierre Ferruit, Peter Jakobsen, and Paolo Strada. James Webb Space Telescope Near-Infrared Spectrograph: dark performance of the first flight candidate detector arrays. In David A. Dorn and Andrew D. Holland, editors, *High Energy, Optical, and Infrared Detectors for Astronomy III*, volume 7021, page 702124. International Society for Optics and Photonics, SPIE, 2008. 3.5

[77] Gert Finger, James W. Beletic, Reinhold Dorn, Manfred Meyer, Leander Mehrgan, Alan F. M. Moorwood, and Joerg Stegmeier. Conversion Gain and Interpixel Capacitance of Cmos Hybrid Focal Plane Arrays. *Experimental Astronomy*, 19(1-3):135–147, January 2005. 3.5

[78] Andrew C. Moore. *Operating, Testing and Evaluating Hybridized Silicon P-I-N Arrays.* PhD thesis, Rochester Institute of Technology, Rochester, NY, USA, 2005. Ph.D. dissertation, Chester F. Carlson Center for Imaging Science. 3.5

[79] Christopher V. Griffith, Stephen D. Bongiorno, David N. Burrows, Abraham D. Falcone, and Zachary R. Prieskorn. Characterization of an x-ray hybrid CMOS detector with low interpixel capacitive crosstalk. In Andrew D. Holland and James W. Beletic, editors, *High Energy, Optical, and Infrared Detectors for Astronomy V*, volume 8453, page 84530F. International Society for Optics and Photonics, SPIE, 2012. 3.5

[80] Arun Kannawadi, Charles A. Shapiro, Rachel Mandelbaum, Christopher M. Hirata, Jeffrey W. Kruk, and Jason D. Rhodes. The impact of interpixel capacitance in cmos detectors on psf shapes and implications for wfirst. *Publications of the Astronomical Society of the Pacific*, 128(967):095001, 2016. 3.5.1

[81] Fei Wang and Albert Theuwissen. Linearity analysis of a cmos image sensor. *Electronic Imaging*, 29(11):84–84, 2017. 3.6

[82] A.A. Plazas, C. Shapiro, R. Smith, J. Rhodes, and E. Huff. Nonlinearity and pixel shifting effects in hxrg infrared detectors. *Journal of Instrumentation*, 12(04):C04009–C04009, April 2017. 3.6.1

[83] Justin P. Gallagher, Lazar Buntic, Donald F. Figer, and Wei Deng. Characterization of single-photon sensing and photon-number resolving CMOS image sensors. In Andrew D. Holland and James Beletic, editors, *X-Ray, Optical, and Infrared Detectors for Astronomy X*, volume 12191 of *Society of Photo-Optical Instrumentation Engineers (SPIE) Conference Series*, page 121910T, August 2022. 4.1

[84] Lance M. Simms, Donald F. Figer, Brandon J. Hanold, Daniel J. Kerr, D. Kirk Gilmore, Steven M. Kahn, and J. Anthony Tyson. First use of a HyViSI H4RG for astronomical observations. In Thomas J. Grycewicz, Cheryl J. Marshall, and Penny G. Warren, editors, *Focal Plane Arrays for Space Telescopes III*, volume 6690 of *Society of Photo-Optical Instrumentation Engineers (SPIE) Conference Series*, page 66900H, September 2007. 4.1

[85] W. H. Krase and Kathleen A. Wolf. *Astronomy and sodium lighting*. 1984. 4.1

[86] D. C. Wells, E. W. Greisen, and R. H. Harten. FITS - a Flexible Image Transport System. *Astronomy and Astrophysics, Supplement*, 44:363, June 1981. 4.3

[87] A. Viana and T. Wiklind. *NICMOS Instrument Handbook*. STScI, 2009. 4.3

[88] J. D. Offenberg, D. J. Fixsen, B. J. Rauscher, W. J. Forrest, R. J. Hanisch, J. C. Mather, M. E. McKelvey, Jr. McMurray, R. E., M. A. Nieto-Santisteban, J. L. Pipher, R. Sengupta, and H. S. Stockman. Validation of Up-the-Ramp Sampling with Cosmic-Ray Rejection on Infrared Detectors. PASP, 113(780):240–254, February 2001. 4.3

[89] F. A. Ringwald. A Cookbook for Reducing KPNO Infrared Array Data. In Diana M. Worrall, Chris Biemesderfer, and Jeannette Barnes, editors, *Astronomical Data Analysis*

*Software and Systems I*, volume 25 of *Astronomical Society of the Pacific Conference Series*, page 328, January 1992. 4.3

[90] R. M. Cutri, M. F. Skrutskie, S. van Dyk, C. A. Beichman, J. M. Carpenter, T. Chester, L. Cambresy, T. Evans, J. Fowler, J. Gizis, E. Howard, J. Huchra, T. Jarrett, E. L. Kopan, J. D. Kirkpatrick, R. M. Light, K. A. Marsh, H. McCallon, S. Schneider, R. Stiening, M. Sykes, M. Weinberg, W. A. Wheaton, S. Wheelock, and N. Zacarias. *2MASS All Sky Catalog of point sources.* 2003. 4.3

[91] John Bally, Adam Ginsburg, Jan Forbrich, and Jaime Vargas-González. The Orion Protostellar Explosion and Runaway Stars Revisited: Stellar Masses, Disk Retention, and an Outflow from the Becklin-Neugebauer Object. ApJ, 889(2):178, February 2020. 4.4

[92] Lynne A. Hillenbrand. On the Stellar Population and Star-Forming History of the Orion Nebula Cluster. AJ, 113:1733–1768, May 1997. 4.4

[93] E. E. Becklin and G. Neugebauer. Observations of an Infrared Star in the Orion Nebula. ApJ, 147:799, February 1967. 4.4

[94] V. Straižys, K. Milašius, R. P. Boyle, F. J. Vrba, U. Munari, N. R. Walborn, K. Černis, A. Kazlauskas, K. Zdanavičius, R. Janusz, J. Zdanavičius, and V. Laugalys. The Enigma of the Open Cluster M29 (NGC 6913) Solved. AJ, 148(5):89, November 2014. 4.5

[95] V. Straižys, F. J. Vrba, R. P. Boyle, K. Milašius, K. Černis, K. Zdanavičius, J. Zdanavičius, A. Kazlauskas, M. Macijauskas, and R. Janusz. Interstellar Extinction in the Direction of the Open Cluster M29. AJ, 149(5):161, May 2015. 4.5

[96] P. Boieriu, C. Buurma, R. Bommena, C. Blissett, C. Grein, and S. Sivananthan. Effects of inductively coupled plasma hydrogen on long-wavelength infrared hgcdte photodiodes. *Journal of Electronic Materials*, 42(12):3379–3384, 2013. 5